ABSTRACT

Title of Dissertation: SYNTHESIS AND DESIGN OF MICROWAVE WIDEBAND FILTERS AND COMPONENTS

Wei Meng, Doctor of Philosophy, 2014

Directed By: Professor Kawthar A. Zaki, Department of Electrical and Computer Engineering

In the development of modern communication systems, various stringent requirements are imposed on the hardware components to support emerging applications. There is broad interest in developing wideband microwave passive components that enable the successful building and integration of wideband communication systems.

The main objective of this dissertation is the development of exact synthesis techniques for wideband microwave filters, based on proposed equivalent circuit models. In the conventional narrowband approach, the multiple resonators are arbitrarily coupled by frequency independent couplings, which do not accurately represent very wideband frequency responses. By replacing the frequency independent couplings by the frequency dependent coupling model in the equivalent circuit, the synthesis techniques are re-developed by: (i) coupling matrix approach and (ii) cascade synthesis approach.

Coupling structures in LTCC (Low Temperature Co-fired Ceramic) technology that can provide very wide coupling bandwidth and are suitable for the developed synthesis technique are analyzed. Various wideband microwave filters realized in LTCC technology which utilize the proposed synthesis approaches are demonstrated by design examples. High performance microwave transitions that can be used for integration of the LTCC broadband filters in wideband communication systems are also investigated.

SYNTHESIS AND DESIGN OF MICROWAVE WIDEBAND FILTERS AND COMPONENTS

By

Wei Meng

Dissertation submitted to the Faculty of the Graduate School of the
University of Maryland, College Park, in partial fulfillment
of the requirements for the degree of
Doctor of Philosophy
2014

Advisory Committee:
Professor Kawthar A. Zaki, Chair/Advisor
Professor Julius Goldhar
Professor Neil Goldsman
Professor Christopher Davis
Professor Amr Baz

DEDICATION

To my parents.

ACKNOWLEDGEMENTS

I would like to express my sincere gratitude to my advisor Prof. Kawthar A. Zaki for her vital guidance and tremendous support during the course of this work. Her exceptional knowledge and enthusiastic energy have been of great benefit to me. This dissertation could not have been accomplished without her patience, encouragement and trust. I am deeply indebted to Dr. Ali E. Atia for his unprecedented ideas and critical suggestions, which have inspired a lot of original work in this dissertation. I am very grateful to four other faculty members of University of Maryland at College Park, Dr. Julius Goldhar, Dr. Neil Goldsman, Dr. Christopher Davis, and Dr. Amr Baz for serving in my Advisory Committee. I would also like to thank Andrew Piloto, Kyocera American Inc., for providing the opportunities and support in his projects. Last but not least, I have to acknowledge the love, understanding, and support of my wife, Chao Liu.

Table of Contents

DEDICATION II

ACKNOWLEDGEMENTS III

TABLE OF CONTENTS IV

LIST OF TABLES IX

LIST OF FIGURES X

CHAPTER 1 INTRODUCTION 1

1.1 Microwave Wideband System 1

1.2 LTCC Technology 3

1.3 Dissertation Objectives 7

1.4 Dissertation Organization 8

1.5 Dissertation Contributions 11

CHAPTER 2 SYNTHESIS OF WIDEBAND MULTICOUPLED RESONATORS FILTERS USING COUPLING MATRIX 13

2.1 Introduction 13

2.2 The Approximation Problem 16

2.2.1 Problem Statement 16

2.2.2 Solving the Approximation Problem in the Lowpass Domain 18

2.2.3 Solving the Approximation Problem in the Bandpass Domain 21

2.3 Coupling Matrix Synthesis for Narrow-Band Filters 34

2.3.1 Overview 34
2.3.2 Circuit Analysis and Coupling Matrix Synthesis 35
2.3.3 Coupling Matrix Reconfiguration 37
2.4 Multi-Coupled Series Resonators Filter Network with Frequency Dependent Couplings 40
2.4.1 Overview 40
2.4.2 Circuit Analysis and Coupling Matrix Synthesis for Inductive Coupling 41
2.4.3 Circuit Analysis and Coupling Matrix Synthesis for Capacitive Coupling 48
2.4.4 Limitation 54
2.5 Multi-Coupled Parallel Resonators Filter Network with Frequency Dependent Couplings 55
2.5.1 Overview 55
2.5.2 Circuit Analysis 56
2.6 Synthesis for All Inductive or All Capacitive Couplings 61
2.6.1 Only Inductive Coupling Elements 61
2.6.2 Only Capacitive Coupling Elements 63
2.6.3 Example 66
2.7 Synthesis of General Case for Composite Couplings 71
2.7.1 Numerical Technique Using Optimization 71
2.7.2 Filter Synthesis Examples 73
2.7.3 Example with Non-Adjacent Couplings 78

CHAPTER 3 CASCADE SYNTHESIS OF WIDEBAND MICROWAVE FILTERS 81

3.1 Introduction 81

3.2 The [*ABCD*] Polynomial Matrix 84

3.2.1 Overview and Circuit Model 84

3.2.2 The Derivation of the [*ABCD*] Polynomial Matrix 86

3.2.3 The Cascade Synthesis and the Extraction Procedure 93

3.3 The Cascade Synthesis 97

3.3.1 Overview 97

3.3.2 The Cascade Synthesis: Step by Step 98

3.4 Composite Type Coupling Inverter 111

3.4.1 Frequency Dependent Coupling Inverter 111

3.4.2 Analysis of Composite Type Frequency Dependent Coupling Inverter 114

3.4.3 Proof of the Equations Used to Extract Composite Coupling Inverter. 118

3.4.4 Examples 124

3.5 Inductive and Capacitive Coupling Inverter 129

3.5.1 Overview 129

3.5.2 Extraction Equations 130

3.5.3 Examples 134

CHAPTER 4 WIDEBAND MICROWAVE FILTERS DESIGNS 140

4.1 Design Methodology 140

4.1.1 Overview 140

4.1.2 Coupling Structures 140

4.1.3 Resonant Frequency and Coupling Coefficient 148
4.2 All Inductive-Coupled and All Capacitive-Coupled LTCC Filters 153
4.2.1 All Inductive Coupled LTCC Filter 153
4.2.2 All Capacitive Coupled LTCC Filter 158
4.3 Wideband Ridge waveguide and Combline-Like Filters 162
4.3.1 Wideband Ridge Waveguide Filter 162
4.3.2 Wideband Combline-Like LTCC Filter with Alternative Capacitive and Inductive Couplings 166
4.4 Bandwidth Enhancement by Negative Inductive Coupling 170
4.4.1 Negative Inductive Coupling 170
4.4.2 Bandwidth Enhancement 175
4.5 Inline Quasi-Elliptic Filter with Composite Type Couplings 179
4.5.1 Composite Type Coupling 179
4.5.2 Inline Quasi-Elliptic Filter 183
CHAPTER 5 MICROWAVE WIDEBAND TRANSITION DESIGNS 190
5.1 Introduction 190
5.2 Coaxial to Stripline Transition Integrated with Lowpass Filter 192
5.3 Wideband Coaxial to Stripline Transition Covering 14-50 GHz 204
5.4 LTCC Substrate to Air-Filled Waveguide Transition 208
CHAPTER 6 CONCLUSIONS AND FUTURE RESEARCH 212
6.1 Conclusions 212
6.2 Future Research 214
APPENDICES 216

Appendix A 216

Appendix B 218

BIBLIOGRAPHY 221

List of Tables

Table 2.1. Roots of Polynomials (in GHz) 31

Table 2.2. Matrix *D* Before Reduction (1e-3*)..... 67

Table 2.3. Matrix *D* After Reduction (1e-3*) 67

Table 2.4. Values of Circuit Elements from Analytical Synthesis and Numerical Optimization for the First Example in Section 2.7.2 (*L* in nH, *C* in nF, *f* in GHz)..... 74

Table 2.5. Normalized Values of Circuit Elements for the Set of Illustrative Examples in Section 2.7.2 (*f* in GHz) 74

Table 5.1. Design Table for Lowpass Filter 198

List of Figures

Figure 1.1. LTCC implementation of ridge waveguide, (a) ridge wave guide with solid metallic wall and housing and (b) LTCC implementation with metallization patches and rows of vertical via. 4

Figure 1.2. The realization of a combline-like resonator, (a) side view and (b) top view; the equivalent circuit model of a combline-like resonator. 5

Figure 1.3. Fields pattern of a combline-like resonator, (a) electric field (side view) and (b) magnetic field (bottom view). 5

Figure 1.4. The realization of a combline-like resonator with an input coupling stripline, (a) side view and (b) top view. 6

Figure 2.1. A general two-port network with (a) voltage source and (b) current source. 16

Figure 2.2. (a) Typical responses of a bandpass filter network. (b) Typical responses of a characteristic function including all critical frequency points in bandpass domain. 26

Figure 2.3. General two-port circuit model of multi-coupled resonators filter network with frequency independent couplings. 35

Figure 2.4. General two-port circuit model of multi-coupled series resonators filter network with frequency dependent couplings. 41

Figure 2.5. Coupling inverter elements: (a) purely capacitive, (b) purely inductive, and (c) a composite of both. 55

Figure 2.6. Circuit model of multicoupled resonators filter. 57

Figure 2.7. Responses of the seventh-degree all-pole filter example. 70

Figure 2.8. Topologies and coupling schemes of the filter synthesis examples in Section 2.7.2. The solid cycles are the source/load nodes. The empty cycles are the resonators. The solid lines are the couplings, which are denoted by the types of the coupling elements above them. 73

Figure 2.9. Responses of the sixth-degree filters. 78

Figure 2.10. Topology and coupling scheme of the six-pole filter in Section 2.7.3. 79

Figure 2.11. Responses of the six-pole filter in Section 2.7.3. 79

Figure 3.1. Circuit model of multicoupled resonators filter in folded form. 84

Figure 3.2. Extraction procedures for a circuit element from the [*ABCD*] polynomial matrix. 94

Figure 3.3. Circuit model for a third-order inline filter with two composite type coupling inverters 97

Figure 3.4. The extraction steps on the first *LC* resonator and the first composite type coupling inverter. 106

Figure 3.5. The equivalent transform of the first *LC* resonator. 107

Figure 3.6. Filter responses evaluated from the extracted results and from the characteristic polynomials. 110

Figure 3.7. Lumped element impedance and admittance inverter. 112

Figure 3.8. Equivalent circuit model of a second-order filter with a composite type coupling inverter. 115

Figure 3.9. Equivalent circuit model with a composite type coupling inverter with a symmetric plane. 115

Figure 3.10. The overall [*ABCD*] and the remainder [*ABCD*] after extracting a *LC* resonator and a composite coupling. 118

Figure 3.11. Another expression for the circuit model in Fig. 3.10. 123

Figure 3.12. Second-order filter with one transmission zero (a) below filter passband; (b) above filter passband. 125

Figure 3.13. Extraction of cross coupling inverter: (a) the overall [*ABCD*]; (b) an inverter represented by $[ABCD]_{inv}$ in parallel with the remainder $[ABCD]_{rem}$..... 133

Figure 3.14. (a) Topology and coupling diagram and (b) frequency responses of the first six-degree filter example. The solid circles are the source/load nodes. The empty circles are the *LC* resonators. The solid lines are the coupling inverters: *L* denotes the inductive type, *C* denotes the capacitive type, and *L/C* denotes the composite type.137

Figure 3.15. (a) Topology and coupling diagram and (b) frequency responses of the second six-degree filter example. 138

Figure 4.1. Magnetic coupling structure I, (a) resonators are in the same direction; (b) and (c) dimensions; (d) the surrounding magnetic field (bottom view). Dimensions in mil: $W = 300$, $L = 400$, $pa = 70$, $pb = 70$, $ra = 50$, $rb = 50$, $H = 118.2$, $D = 70$, $l1 = 110.32$, and $l2 = 7.88$. (Dielectric constant = 7.7)..... 144

Figure 4.2. Magnetic coupling structure II, (a) resonators are in the opposite direction; (b) and (c) dimensions; (d) the surrounding magnetic field (bottom view). Dimensions

in mil: W = 300, L = 400, pa = 70, pb = 70, ra = 50, rb = 50, H = 118.2, D = 70, $l1$ = 110.32, and $l2$ = 7.88. (Dielectric constant = 7.7)..... 145

Figure 4.3. Electric coupling structure I, (a) coupled by an additional floating conductor patch; (b) and (c) dimensions; (d) the electric field in patches area (side view). Dimensions in mil: W = 300, L = 400, pa = 70, pb = 70, ra = 50, rb = 50, H = 118.2, D = 100, $l1$ = 110.32, $l2$ = 7.88, $l3$ = 3.94, and Dr = 60. (Dielectric constant = 7.7). 146

Figure 4.4. Electric coupling structure II, (a) directly coupled by the overlapping of two conductor patches; (b) and (c) dimensions; (d) the electric field in patches area (side view). Dimensions in mil: W = 300, L = 400, pa = 70, pb = 70, ra = 50, rb = 50, H = 224.58, D = 20, $l1$ = 110.32, $l2$ = 19.7, $l3$ = 7.88, and $l4$ = 102.44. (Dielectric constant = 7.7)..... 147

Figure 4.5. Magnetic and electric coupling coefficient k and resonant frequency f_0 curves of the four coupling structures versus the distance D: (a) for the structure in Fig. 4.1 (a); (b) for the structure in Fig. 4.2 (a); (c) for the structure in Fig. 4.3 (a); (d) for the structure in Fig. 4.4 (a). 152

Figure 4.6. (a) Topology and coupling diagram and (b) the responses of the fourth-degree filter example. The solid circles are the source/load nodes. The empty circles are the LC resonator. The solid lines are the coupling inverters, L denotes the inductive type. 155

Figure 4.7. (a) Physical structure and (b) dimensions of the fourth-degree filter example in HFSS. (unit: mil, dielectric constant = 7.6)..... 156

Figure 4.8. (a) Final realization of the fourth-degree filter example in via model with stripline transitions and launches in HFSS simulator. (b) Fabricated filter example in measurement. 157

Figure 4.9. Measurement results of the fourth-degree filter example: the dashed lines are from HFSS simulation of final realization model; all other solid lines are from measurements of different fabricated filters. 158

Figure 4.10. (a) Topology and coupling diagram and (b) the responses of the third-degree filter example. *C* denotes the capacitive coupling..... 160

Figure 4.11. (a) Physical structure and (b)-(c) dimensions of the third-degree filter example in HFSS. (unit: mil, dielectric constant = 7.7)..... 161

Figure 4.12. (a) Topology and coupling diagram and (b) the responses of the seventh-degree ridge waveguide filter..... 164

Figure 4.13. (a) Physical structure and (b)-(c) dimensions of the seventh-degree LTCC ridge waveguide filter in HFSS. (unit: mil, dielectric constant = 7.6): a = 180, b = 78.8, h = 7.88, $w1$ = 81, $w2$ = 27, $r1$ = 59.23, $r2$ = 35.19, $r3$ = 22.80, $r4$ = 20.46, $i1$ = 82.61, $i2$ = 30.66, $i3$ = 55.58, and $i4$ = 66.53. 165

Figure 4.14. (a) Topology and coupling diagram and (b) the responses of the seventh-degree combline-like LTCC filter. 168

Figure 4.15. (a) Physical structure and (b) dimensions of the seventh-degree combline-like LTCC filter in HFSS. (unit: mil, dielectric constant = 7.7) 169

Figure 4.16. 2-pole filter in LTCC: (a) two posts are both shorted at bottom ground plane. (b) The second post is flipped and shorted at the top ground plane. (c) Two patches are shifted. Dimensions in mil: W = 100, L = 300, pa = 70, pb = 40, ra = 40,

rb = 40, *H* = 39.4, *l1* = 31.52, *l2* = 27.58, *l3* = 31.52, *f1* = 16, *f2* = 18, *f3* = 13.5, *D* = 30, *Dp* = 10. Dielectric constant = 7.8. 173

Figure 4.17. The phase of S21 for the filter structures in Fig. 4.16 (a) and (b). 174

Figure 4.18. The frequency responses of the three filter structures in Fig. 4.16: solid lines for (a), dot-dashed lines for (b), and dashed lines for (c). 174

Figure 4.19. 3-pole filter in LTCC: (a) no overlapping between the conductor patches. (b) The conductor patches are shifted by *Dp1* = 20 mil. (c) The conductor patches are shifted by *Dp2* = 30 mil. Dimensions in mil: *W* = 140, *L* = 400, *ra* = 20, *rb* = 20, *H* = 55.16, *pa1* = 102.7, *pb1* = 100, *pa2* = 120.2, *pb2* = 100, *pa3* = 115.2, *pb3* = 115, *pa4* = 106, *pb4* = 100, *D* = 50, *l1* = 35.46, *s1* = 4.5, *s2* = 21, and *s3* = 28. Dielectric constant = 7.8. 177

Figure 4.20. The frequency responses of three filter structures in Fig. 4.19: solid lines for (a), dot-dashed lines for (b), and dashed lines for (c). 178

Figure 4.21. Realization of composite type coupling, with strong capacitive coupling and weak inductive coupling. Dimensions in mil: *W* = 140, *L* = 300, *ra* = 40, *rb* = 40, *H* = 52.2, *H1* = 30.6, *pa1* = 102, *pb1* = 40, *pa2* = 80, *pb2* = 118, *D* = 60, *s1* = 50, *w1* = 90, and *w2* = 13.5. Dielectric constant = 7.8. 181

Figure 4.22. Frequency responses of the filter structure in Fig. 4.21. 182

Figure 4.23. Realization of composite type coupling, with strong inductive coupling and weak capacitive coupling. Dimensions in mil: *W* = 140, *L* = 300, *ra* = 60, *rb* = 35, *H* = 44.1, *H1* = 30.6, *pa1* = 110, *pb1* = 56, *pa2* = 80, *pb2* = 60, *D* = 19, *s1* = 35. Dielectric constant = 7.8. 182

Figure 4.24. Frequency responses of the filter structure in Fig. 4.23. 183

Figure 4.25. Circuit model of fourth-degree inline quasi-elliptic filter with composite type couplings. 184

Figure 4.26. Realization of fourth-degree inline filter in HFSS with via model. Dimensions in mil: W = 140, L = 520, H = 52.2, $H1$ = 30.6, $H2$ = 30.6, $H3$= 44.1, $H4$ = 21.6, $D2$ = 40.06. Dielectric constant = 7.8. 185

Figure 4.27. Realization of the first and second resonators in Fig. 4.26. Dimensions in mil: ra = 40, rb = 40, $pa1$ = 119.35, $pb1$ = 40, $pa2$ = 100.78, $pb2$ = 40, $pa3$ = 80, $pb3$ = 120.11, $D1$ = 60, $D4$ = 18, $s1$ = 65.36, $w1$ = 90, $w2$ = 13.5. Dielectric constant = 7.8. 185

Figure 4.28. Realization of the third and fourth resonators in Fig. 4.26. Dimensions in mil: ra = 60, rb = 35, $pa1$ = 109.01, $pb1$ = 50, $pa2$ = 113.34, $pb2$ = 50, $pa3$ = 80, $pb3$ = 60, $D3$ = 13.47, $s2$ = 51.63, $s3$ = 10. Dielectric constant = 7.8. 186

Figure 4.29. Frequency responses of fourth-degree inline filter from the HFSS model and from the circuit model. 186

Figure 4.30. (a) Frequency responses of fourth-degree inline filter: the dashed lines are from HFSS simulation of the entire filter model with stripline transitions and launches; all other solid lines are from measurements of different fabricated filters. (b) Fabricated filter example in measurement. 187

Figure 5.1. (a) Original design, there are two components: a coaxial to stripline transition and a bandpass filter. (b) New design with only one component: a coaxial to stripline transition integrated with a lowpass filter. 193

Figure 5.2. Lowpass filter prototype. (n is odd) 195

Figure 5.3. Realization of stripline in LTCC. (Dimension in mil): a = 55, b = 36, h = 14.4, *w1* = 3. (Dielectric constant = 7.8)..... 196

Figure 5.4. Realization of lowpass filter in LTCC, (a) frequency responses from initial design parameters (calculated from formulas) and optimized parameters, (b) physical model in HFSS. (Dimension in mil), *sl1-sl6* refers to Table 5.1, a = 55, b = 36, *wi* = 9, *wh* = 3, *wl* = 35. (Dielectric constant = 7.8)..... 201

Figure 5.5. Realization of coaxial to stripline transition integrated with lowpass filter in LTCC, (a) frequency responses from coaxial connector and final optimized design parameters, (b) physical model of coaxial connector to one stripline section, and (c) physical model of entire transition design in HFSS. (Dimension in mil), *sl1-sl11* refers to Table 5.1, the width of lines is the same as that in Fig. 5.4, a = 55, b = 36, *sl0* = 40, l = 454. (Dielectric constant = 7.8). 203

Figure 5.6. Physical structure of coaxial connector with one stripline section..... 206

Figure 5.7. Realization of coaxial to stripline transition. (Dimensions in mil): *a1* = 54.2, *b1* = 60, *a2* = 45, *b2* = 30, *w8* = 6.5, and other dimensions are given in (5.4). (Dielectric constant = 8.8)..... 206

Figure 5.8. Frequency responses of coaxial to stripline transition. 207

Figure 5.9. Realization of LTCC substrate to air-filled waveguide transition in LTCC. (Dielectric constant = 8.8)..... 210

Figure 5.10. Frequency responses of LTCC substrate to air-filled waveguide transition. 211

Chapter 1 Introduction

1.1 MICROWAVE WIDEBAND SYSTEM

In the development of modern communication systems, various stringent requirements are imposed on the hardware components to support emerging applications. Microwave communication systems have been widely deployed in cellular communication networks, broadcast satellites for TV and broadband internet services, radar and sensing systems for both civilian and defense applications.

In [1], a wideband communication satellite payload architecture is proposed. Conventionally, communication satellite transponders use channelized filter banks to allocate the frequency bands into narrowband channels. Technology advancement has achieved revolutionary results for satellite communication, such as digital signal processing techniques (DVB-S2 [2]), mobile Very Small Aperture Terminal (VSAT) on ground, and so on. However, the basic configuration of a communication satellite payload has remained on a channelized approach [3]. By adopting wideband architecture, the system complexity and the payload mass are significantly reduced. For a typical Ku-Band transponder with 12 channels of 36 MHz bandwidth each, a combined single 500 MHz channel can achieve high frequency spectrum utilization with more usable bandwidth, and possibly improve the overall power efficiency, as analyzed in [1].

Emerging Active Electronically Scanned Array (AESA) applications require a Monolithic Microwave Integrated Circuit (MMIC) Transmitter/Receiver (T/R) frontend module to operate over very wide frequency bandwidth, and support multi-band / multi-function applications. Therefore, considerable efforts have been made in this area [4] [5]. High performance components of ultra wideband antennas, broadband high-power monolithic amplifiers, and novelty in array architecture have been successfully developed and tested. Moreover, such frontend modules require highly system level integration and great miniaturization through advanced packaging technology. In [6], a high-power, wide bandwidth, and compact size frontend module using multilayer ceramic technology has been introduced, which can operate up to Ku-Band.

Therefore, there is broad interest in developing wideband microwave passive components that enable the successful building and integration of wideband communication systems.

1.2 LTCC TECHNOLOGY

LTCC (Low Temperature Co-fired Ceramic) technology has found increasingly promising potential especially for RF and microwave applications. LTCC technology features the capability of embedding passive elements, such as resistors, capacitors, and inductors into a ceramic-based substrate, providing multichip and multi-substrate packaging. The technology also includes the surface mounted active components, thus enabling the solutions of System-in-Packaging integration and miniaturization [43].

The realizations of microwave filters in LTCC technology have already had significant attention in industry and academia [44]-[51]. In early work, LTCC has been typically used in planar multilayer structures, which suffer from higher loss [52]. In [44], the LTCC waveguide filter was first introduced using a similar structure to conventional inductive windows. In [53]-[54], the conventional ridge waveguide was also applied to LTCC technology to realize wideband filters. In both cases, the use of metallization patches and rows of vertical vias as fences to approximate the conductors and metallic housing takes full advantage of a 3-dimensional structure in LTCC. This consequently achieves low volume and small size, high packaging density, and relatively high Q value. In Fig. 1.1, a typical LTCC implementation of a ridge waveguide is shown as a conceptual illustration.

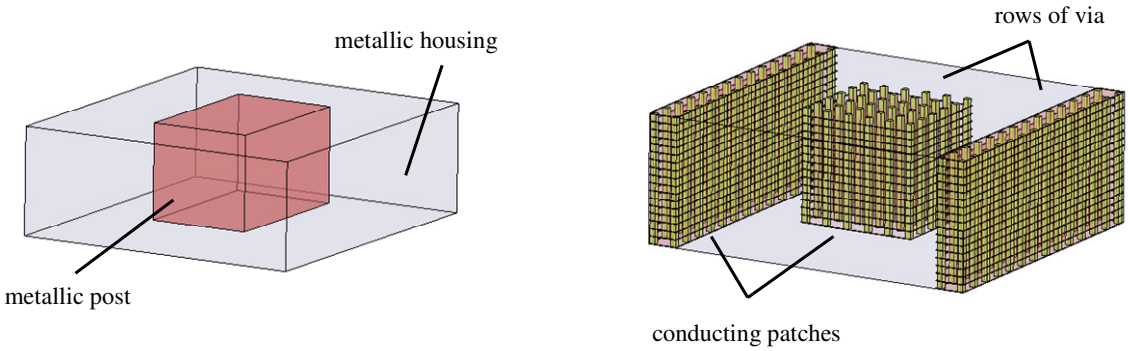

Figure 1.1. LTCC implementation of ridge waveguide, (a) ridge wave guide with solid metallic wall and housing and (b) LTCC implementation with metallization patches and rows of vertical via.

In this dissertation, a combline-like resonator structure in LTCC is introduced to design a broad range of wideband microwave filters. The typical realization of the proposed combline-like resonator for LTCC technology is shown in Fig. 1.2. The resonator consists of a vertical square or rectangular metallic post shorted at the bottom (bottom ground plane) and a conducting patch at the other open end. The resonant mode of a conventional combline structure is a TEM mode [55]-[56]. The electric field and magnetic field patterns of the fundamental resonant mode of this combline-like structure are shown in Fig. 1.3. As expected, the electric field is mainly concentrated between the conducting patch and the top ground plane and the magnetic field is circulating around the metallic post.

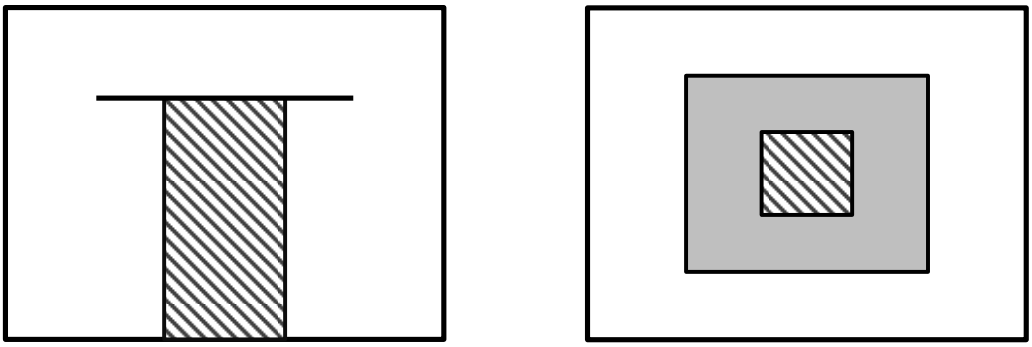

(a) (b)

Figure 1.2. The realization of a combline-like resonator, (a) side view and (b) top view; the equivalent circuit model of a combline-like resonator.

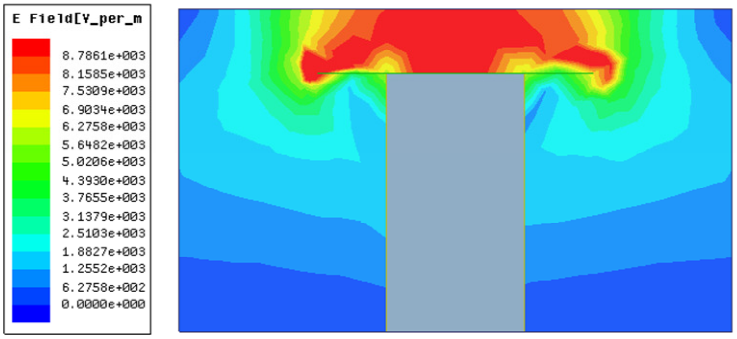

(a)

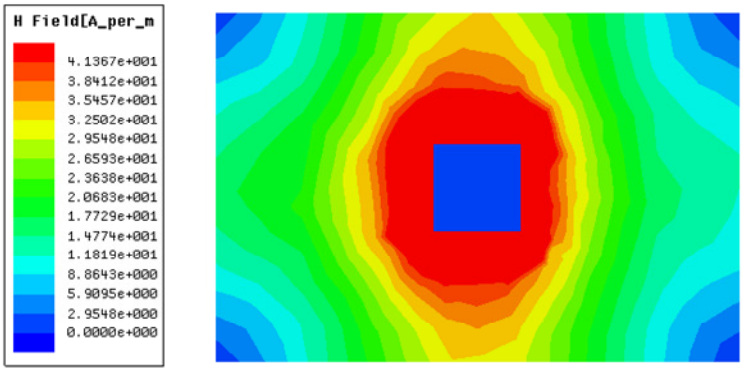

(b)

Figure 1.3. Fields pattern of a combline-like resonator, (a) electric field (side view) and (b) magnetic field (bottom view).

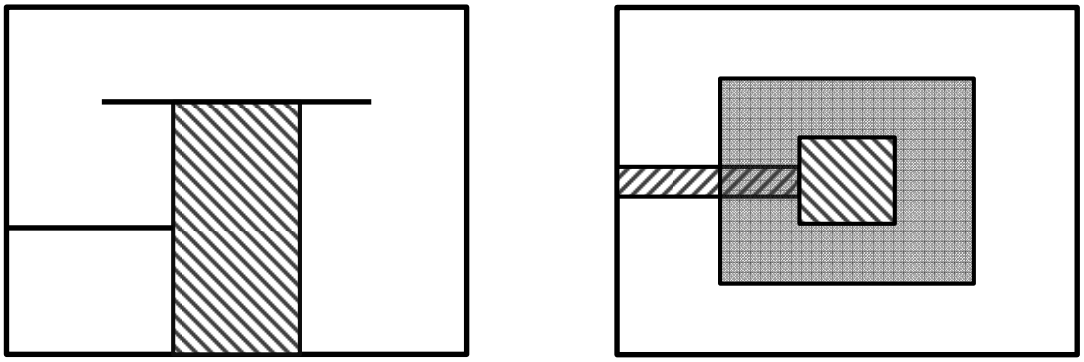

(a) (b)

Figure 1.4. The realization of a combline-like resonator with an input coupling stripline, (a) side view and (b) top view.

Therefore, the equivalent circuit model of such a combline-like resonator structure can be simply modeled an *LC* resonator. The resonant frequency is controlled by the length of the metallic post, the area of the conducting patch and the gap distance between the patch and the ground plane.

Due to the nature of a layered stack structure in LTCC technology, it is most convenient to utilize a tapped-in stripline as an input / output coupling realization as shown in Fig. 4.4. The amount of input coupling or the input impedance is controlled by the tapped-in position and the width of the stripline. Another important factor is that the 50 Ohm characteristic impedance line can be easily achieved by a simple stripline transition [57].

1.3 DISSERTATION OBJECTIVES

The increased demand for high performance wideband microwave components inspired the research and development work presented in this dissertation.

The main objective of this dissertation is the development of exact synthesis techniques for wideband microwave filters, based on proposed equivalent circuit models. The filters' frequency responses can cover a very wide frequency range, and at the same time, maintain very high performance to satisfy stringent specifications.

This dissertation is devoted to developing novel synthesis techniques of wideband microwave filters by: (i) coupling matrix approach and (ii) cascade synthesis approach. Coupling structures in LTCC technology that can provide very wide coupling bandwidth and are suitable for the developed synthesis technique are analyzed. Various wideband microwave filters which utilize the proposed synthesis approaches are demonstrated by design examples. High performance microwave transitions that can be used for integration of the LTCC broadband filters in communication systems are also investigated.

1.4 DISSERTATION ORGANIZATION

The dissertation is composed of six chapters. Chapter One is this introduction.

Chapter Two is devoted to the coupling matrix approach for the synthesis of wideband multi-coupled resonators filters with frequency dependent couplings. In a conventional narrowband approach, the multiple resonators are arbitrarily coupled by frequency independent couplings, which do not accurately represent very wideband frequency responses. By replacing the frequency independent couplings by the frequency dependent coupling model in the equivalent circuit, the synthesis technique by coupling matrix approach is re-developed. The approximation problem is directly solved in the bandpass domain instead of in the lowpass domain, to derive the filtering characteristic function, from which the [*Z*]-parameters are derived. The equivalent circuit model consisting of *LC* resonators and frequency dependent couplings in a filter network is analyzed, also to derive its [*Z*]-parameters. By equating the two sets of derived [*Z*]-parameters, the values of circuit elements are synthesized according to the prescribed specifications.

Chapter Three is focused on another approach, cascaded network synthesis of wideband microwave filters with frequency dependent couplings. The conventional synthesis of a ladder network consisting of lumped circuit elements cannot provide an analytical solution for the folded circuit network topology. The conventional network synthesis approach is also incapable of incorporating frequency dependent couplings.

Therefore, the network synthesis approach is further developed to enable frequency dependent couplings, suitable for representing the filter frequency responses over a wide frequency range. This approach is primarily based on the [*ABCD*] matrix. The overall [*ABCD*] matrix of a circuit network can be built up by cascading the [*ABCD*] matrix of each individual circuit element. The synthesis can be regarded as an inverse process, which will extract the values of all circuit elements from the overall [*ABCD*] matrix following a pre-defined sequence.

Chapter Four presents several physical designs of wideband microwave filters. A combline-like resonator structure suitable for LTCC realization is introduced, which can also be easily modeled by *LC* resonators as an equivalent circuit. Four coupling structures constructed by the combline-like resonators are investigated in detail. These structures provide frequency dependent coupling inverters in the equivalent circuit model. For each filter design example its equivalent circuit is first synthesized by using one of the synthesis techniques introduced in Chapter Two or Chapter Three. Next, the physical realizations of the filters based on the combline-like resonator structures, and one or multiple coupling realizations in LTCC technology are presented. The filters are then implemented and optimized in electromagnetic (EM) simulating software, HFSS, to obtain the optimum dimensions satisfying the prescribed specifications. Some measurement results are also included to demonstrate the successfulness of the synthesis techniques and design procedures.

Chapter Five deals with another important microwave component, the transition in wideband communication systems. In LTCC technology, passive components are usually buried into a multi-layer ceramic structure for the benefit of 3D integration and the application of system-on-chip packaging. Therefore, a transition acting as an interface between the buried passive components and the external conventional connectors is needed. These external connectors can be coaxial to connect to coaxial signal cable or a co-planar waveguide launcher for measurements by probe station. The transition is a critical element in the development of LTCC module. In addition, a novel transition design capable of integrating other functionality, such as embedded filtering function is also presented. Finally a transition with very wide operating frequency range implemented in LTCC is presented in this Chapter.

In Chapter Six, the conclusions of this dissertation are summarized, and further research work is discussed.

1.5 DISSERTATION CONTRIBUTIONS

The main contributions of this dissertation are summarized as the follows.

1. The approximation problem determining the filtering characteristic function is directly derived and solved in the filter bandpass domain, so that it is suitable for the equivalent circuit model of a filter network with frequency dependent couplings.

2. The multi-coupled resonators filter network with frequency dependent coupling is directly solved and synthesized in the bandpass domain, instead of transforming and solving it in a lowpass prototype.

3. The cascade synthesis approach for a filter network in the bandpass domain is also re-developed to enable the inclusion of frequency dependent coupling and folded coupling structure.

4. Three types of frequency dependent coupling inverters have been identified, and have been applied into the developed novel synthesis techniques.

5. The microwave filter realizations in LTCC technology are intensively investigated for very wide frequency band applications.

6. Four types of coupling structures for combline-like resonators in LTCC realization are investigated in details. These are the basic structures for the wideband filter realization in LTCC.

7. A novel quasi-elliptic inline filter is synthesized by the developed techniques, designed in an electromagnetic simulator and successfully built and tested. This filter

has simple topology, small physical layout, and two transmission zeros realized at finite frequencies.

8. Several transitions in LTCC have also been designed, which feature very wide bandwidth, or embedded filtering function.

The publications from this dissertation are given in [13] [41] [72] and [73].

Chapter 2 Synthesis of Wideband Multicoupled Resonators Filters Using Coupling Matrix

2.1 INTRODUCTION

The synthesis techniques of narrowband multicoupled resonators filters have been well documented [7]-[9]. In those studies, the two-port lossless filter network is modeled by lumped *LC* resonators with multiple frequency independent couplings. Given a filtering function with prescribed order, passband return-loss level, and transmission zeros, a coupling matrix can be analytically synthesized. This approach proved to be sufficiently accurate for narrowband filters, but is not adequate as the filter bandwidth is increased. For wideband filters, the circuit model with frequency independent coupling elements does not accurately reproduce the responses of a physical electromagnetic structure.

A coupling element in microwave structures behaves as a capacitance (electric field coupling), an inductance (magnetic field coupling) or a combination of both. Early work on wideband filters by Wenzel [10], [11] discussed the qualitative behavior of the responses of multicoupled resonators filters with simple coupling elements (single inductive or capacitive elements). The discussions in [10] focused only on canonical cross coupled structures, and did not present a systematic synthesis procedure. It has

also been shown in [12] that a multicoupled resonators filter whose coupling coefficients are linear functions of frequency can be transformed to a filter network with constant coupling coefficients. Recently, several attempts have been made on the exact synthesis of wideband microwave filters [13], [14]. The couplings in waveguide technology can be approximated as a linear function of the guided wavelength, not with the frequency as in TEM cases. However if the filter bandwidth is moderate, such linear frequency dependence could be applied as a good approximation.

In this Chapter, a synthesis technique is presented that accounts for the frequency variation of microwave coupling structures. The circuit model of a two-port lossless filter network consists of a number of *LC* resonators arbitrarily coupled by frequency dependent coupling elements. The type of coupling elements can be capacitive, inductive or a composite of both. The two-port impedance parameters of the filter are obtained in the form of partial fraction expansion from the nodal analysis of the circuit. The corresponding impedance parameters can also be evaluated from the desired transfer and reflection functions of the filter. By identifying the impedance parameters obtained from the circuit analysis and those from the desired transfer and reflection functions, it is possible to determine the values of the circuit elements.

The recent work [14] addresses the same problem of wideband filter synthesis by a different approach. It utilizes the so-called “transversal circuit” and manipulates it to achieve different equivalent circuit that may be realizable in a physical structure. In this Chapter, a totally different and systematic approach for exact synthesis of

wideband microwave filters with frequency dependent couplings is presented. The circuit model has direct correspondence to physical realization. The physical representation is clear and straightforward. The filtering characteristic function is directly obtained in the bandpass domain, avoiding any low-pass to bandpass, or variable transformations.

2.2 THE APPROXIMATION PROBLEM

2.2.1 Problem Statement

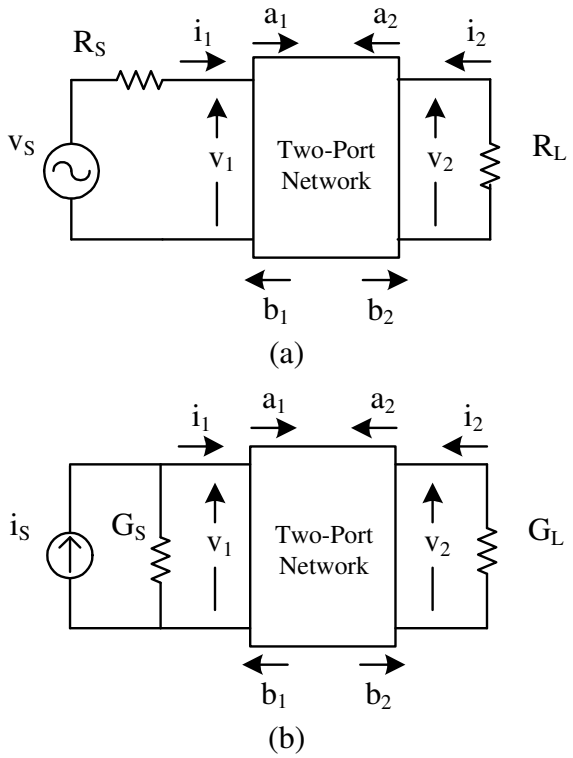

Figure 2.1. A general two-port network with (a) voltage source and (b) current source.

For a general two-port lossless, lumped element, reciprocal network as shown in Fig. 2.1, the transfer and reflection functions (known as Scattering or *S*-parameters) are expressed as rational functions of the complex frequency variable *s*:

$$S_{11}(s) = \frac{F(s)}{E(s)} \text{ and } S_{21}(s) = \frac{P(s)}{\varepsilon E(s)} \tag{2.1}$$

From (2.1), each of the transfer and reflection functions can be expressed as a ratio of two polynomial functions in *s*. The properties of the polynomials *E(s)*, *F(s)* and *P(s)* and the definition of the constant ε will be introduced in the following sections that consider two cases: one for a lowpass prototype network and the other for a bandpass filter network.

The approximation problem in filter theory determines realizable rational transfer and reflection functions of minimum degree satisfying the desired specifications, such as insertion loss (IL), return loss (RL), and group delay (GD). The produced transfer and reflection functions can meet the given requirements on the amplitude responses in all passbands and stopbands, and the phase responses in the passbands. Proceeding to the next step, the transfer and reflection functions will then be synthesized and realized by a filter prototype network with specific topologies and coupling structures.

For a lossless network, the conservation of energy formula should also apply

$$\left|S_{11}(s)\right|^2 + \left|S_{21}(s)\right|^2 = 1 \tag{2.2}$$

for real frequency $s = j\omega$.

Therefore, the following equation must hold

$$E(s)E\ (-s) = F(s)F\ (-s) + \frac{1}{\varepsilon^2} P(s)P\ (-s) \tag{2.3}$$

where the polynomial *E(s)*, *F(s)* and *P(s)* have real coefficients.

Using (2.3), the transfer and reflection functions in (2.1) can be further expressed as

$$\begin{aligned} \left|S_{11}(j\omega)\right|^2 &= \frac{\varepsilon^2 C^2(j\omega)}{1+\varepsilon^2 C^2(j\omega)} \\ \left|S_{21}(j\omega)\right|^2 &= \frac{1}{1+\varepsilon^2 C^2(j\omega)} \end{aligned} \tag{2.4}$$

where $C(j\omega)$ is known as the characteristic function:

$$C(j\omega) = \frac{F(j\omega)}{P(j\omega)} \tag{2.5}$$

and $s = j\omega$. The properties of the characteristic function $C(j\omega)$ will also be introduced in the following sub-sections that consider lowpass and bandpass domains, respectively.

The approximation problem is herein re-defined as to finding the characteristic function $C(j\omega)$, i.e., to finding the values of zeros and poles of the characteristic function $C(j\omega)$ for an optimum filtering function with equiripple levels in all passbands and stopbands of minimum degrees.

2.2.2 Solving the Approximation Problem in the Lowpass Domain

The two-port lossless lowpass prototype filter is normalized to a cutoff frequency of 1 radian per second and has impedance level of 1 Ω at each port. The traditional synthesis of the lowpass prototype filter network is carried out that are normalized in frequency and impedance level. Using the frequency variable transformation and the

scaling in frequency and impedance level, it is possible to realize bandpass filter networks with any desirable frequency bandwidth and impedance levels.

For any two-port lossless filter prototype network in the lowpass domain composed of N multi-coupled resonators, the transfer and reflection functions can be expressed as a ratio of two Nth degree *complex* polynomials as in (2.1), where s is the complex frequency variable $s = \alpha + j\omega$, and ε is a real constant normalizing the transfer function S_{21} to the equiripple level at $\omega = \pm 1$ as follows:

$$\varepsilon = \frac{1}{\sqrt{10^{RL/10} - 1}} \cdot \left| \frac{P(\omega)}{F(\omega)} \right|_{\omega=\pm 1} \tag{2.6}$$

where RL is the prescribed return loss level in decibels.

The polynomials $E(s)$, $F(s)$ and $P(s)$ are all monic polynomials, i.e.,the coefficients of their highest degrees are unity. Moreover, they must assure the following requirements to satisfy the conditions of a realizable two-port lossless prototype network:

1. The polynomial $P(s)$ containing the prescribed transmission zeros of the transfer function is of degree $M \leq N - 1$. Prescribing the positions of the transmission zeros follows the rule that symmetry must be preserved about the imaginary ($j\omega$) axis of the complex s-plane.
2. The polynomial $F(s)$ is of degree N, where N is the degree of the filtering function.
3. The polynomial $E(s)$ is a strict Hurwitz polynomial of degree N, whose zeros must lie in the left half of the complex s-plane.

The aim now is to find the zeros and poles of the characteristic function $C(j\omega)$ in (2.5) of an optimum solution. The analytic determination, as the most desirable approach, of the characteristic function in the lowpass domain is known for several classes of generic mathematical functions:

1. All-pole functions employing some well-known functions, i.e., Butterworth, Chebyshev, and Bessel types.
2. Transfer functions having the maximum number of real frequency transmission zeros, i.e., the Elliptic function type.
3. Generalized Chebyshev filtering functions solved by recursion techniques with symmetrically or asymmetrically prescribed transmission zeros and/or group delay equalization zero pairs.

On the other hand, some numerical techniques, still a favorable approach, have also been implemented to solving the approximation problem by which the optimum filtering function can be obtained to satisfy any specific requirements. One of the widely used techniques is the transformed variables to synthesize lowpass prototype network for narrow bandpass filters. The strong usefulness of these transformed variable techniques has already been demonstrated in numerous publications. Also, such a technique can be applied to increase the computation accuracy for the filtering functions of very high degrees, namely for the filter network with high order.

Solving the approximation problem in the lowpass domain has also been extended to the design of multi-band filters, namely, multiple passbands filters. The characteristic filtering function can be numerically obtained by placing the transmission zeros within the original passband to generate a large amount of reflection and herein create multiple passbands. Once the characteristic function exhibiting multiple passbands is generated, the same synthesis and design technique can be applied to realize multi-band filters.

For the application of bandstop filters, a bandpass-like filter configuration with bandstop filtering characteristic can be easily created by simply exchanging the transfer function $S_{21}(s)$ and the reflection function $S_{11}(s)$, so that what used to be return loss characteristic now becomes the transfer characteristic, and vice versa. If the filtering characteristic is a Chebyshev function for instance, the original prescribed equiripple return loss level becomes the equiripple stopband attuenation, whereas the former rejection levels out of passband become the return loss performance out of stopband. Therefore, the approximation problem can be solved in the same manner to obtain the filtering characteristic for bandstop filter applications.

2.2.3 Solving the Approximation Problem in the Bandpass Domain

The two-port lossless bandpass filter is directly defined on the frequency passband. Therefore, the frequency variable transformation is not necessarily involved. The impedance level could be set to 1 Ω for simplicity or scaled to any practical values.

For any two-port lossless filter network in the bandpass domain composed of *N* multi-coupled resonators, the transfer and reflection functions can also be expressed in the form as shown in (2.1). Nevertheless, they, in this case, are of a ratio between two *2N*th degree *real* polynomials in the complex frequency variable $s = \alpha + j\omega$. Similarly, ε is a real constant normalizing the transfer function S_{21} to the equiripple level

$$\varepsilon = \frac{1}{\sqrt{10^{RL/10} - 1}} \cdot \left| \frac{P(\omega)}{F(\omega)} \right|_{\omega=\omega 1 \text{ or } \omega 2} \tag{2.7}$$

where ω_1 and ω_2 are the real frequency points at low and high side of the equiripple level of the filter passband, respectively, and *RL* is the prescribed return loss level in decibels.

The following properties of polynomials *E(s)*, *F(s)*, and *P(s)* should be satisfied, in order to be realizable in a two-port lossless network in the bandpass domain:

1) The polynomials *E(s)*, *F(s)* and *P(s)* are all monic polynomials, i.e., the coefficients of their highest degrees are unity.
2) The polynomial *P(s)* containing the prescribed transmission zeros of the transfer function is of degree less than *2N*. Prescribing the positions of the transmission zeros follows the rule that symmetry must be preserved about the imaginary

($j\omega$) axis of the complex *s*-plane, or the transmission zeros are directly located on the imaginary ($j\omega$) axis.

3) The polynomial *F(s)* is of degree *2N*, where 2*N* is the degree of the filtering function.
4) The polynomial *E(s)* is a strict Hurwitz polynomial of degree 2*N*, whose zeros must lie in the left half of the complex *s*-plane.
5) The formula for the conservation of energy (2.2) also holds.

Therefore, the characteristic function defined in (2.5) can now be expressed as

$$C(j\omega) = \frac{F(j\omega)}{P(j\omega)} = \frac{\prod_{i=1}^{N}(\omega^2 - p_i^2)}{\omega^p \prod_{j=1}^{M}(\omega^2 - z_j^2)\prod_{i=1}^{L}(\omega^2 + c_i^2)\prod_{i=1}^{K}(\omega^4 + d_i\,\omega^2 + e_i)} \quad (2.8)$$

where p_i, $i = 1, 2, \ldots, N$, are the reflection poles, z_j, $j = 1, 2, \ldots, M$, are the transmission zeros (corresponding to real frequencies). Other coefficients, c_i, d_i, and e_i are derived from real or complex transmission zeros, which is usually prescribed and may be utilized for group delay equalization. It is obviously to see the following equation must be true

$$p + 2M + 2L + 4K < 2N$$

$$d_i^2 - 4e_i < 0, \quad i = 1, \ldots, K \quad (2.9)$$

Comparing the characteristic function and the transfer and reflection functions defined in the bandpass domain to those in the lowpass domain, a primary, but critical difference is the orders of the polynomials for the filter networks with the same

number of N resonators. Precisely, the orders of the polynomials $E(s)$ and $F(s)$ are $2N$ instead of N. Doubling the order of polynomial to $2N$ makes it possible to directly represent the characteristic function $C(j\omega)$ in the bandpass domain. Also, the zeros and poles of the characteristic function are directly defined in the bandpass domain (real frequency points) without using any frequency transformation between the bandpass and lowpass domains. Therefore, any amount of filter bandwidth in filter design requirement can be theoretically accomplished. The order p of the frequency variable ω in (2.8) is arbitrary as long as the characteristic function $C(j\omega)$ is an odd function and the inequality in (2.9) is satisfied. The order p actually represents the number of transmission zeros at zero frequency. Also, it should be chosen carefully according to realizable filter physical structures.

In order to find the zeros and poles of the characteristic function $C(j\omega)$ in (2.8) for an optimum filtering function, some numerical techniques are typically required. There is no general analytic solution to this problem. One possible solution of the approximation problem has been given in [17] using transformed variable for different classes of wideband filters, in which the approximation problem is solved in the lowpass domain. An obvious motivation using transformed variable is that, when such a problem was initially postulated in filter theory, the computing power in that era was severely restricted and the design automation of filter synthesis is extremely limited. Nevertheless, the characteristic function in (2.8) can still be directly solved in bandpass domain. In [18], another possible numerical technique is introduced with detail equations to realize an optimum filtering function in the lowpass domain for

multiband filter synthesis. The same concept and technique has been applied to solving the approximation problem in the bandpass domain. The detailed derivations, equations and algorithms are given below.

As shown in Fig. 2.2 (a), the determination of the characteristic function is based on the bandpass filter network, obtaining an equiripple performance in each passband and stopband, which will mathematically depict an optimum filtering function. The passband is defined by two frequency points, ω_2 and ω_3. The return loss between these two points is equiripple, and its level is usually prescribed according to the specification. The frequency point ω_1 is the band edge equiripple point of the lower stopband. Similarly, ω_4 is the band edge equiripple point of the upper stopband. The attenuation levels of the stopbands are usually controlled by the number of transmission zeros in respective stopbands. Other requirements, like phase and group delay, can also be accomplished by prescribing real and/or complex transmission zeros in (2.8). It is worth mentioning again that ω_1, ω_2, ω_3 and ω_4 in Fig. 2.2 (a) are directly defined as real frequency points.

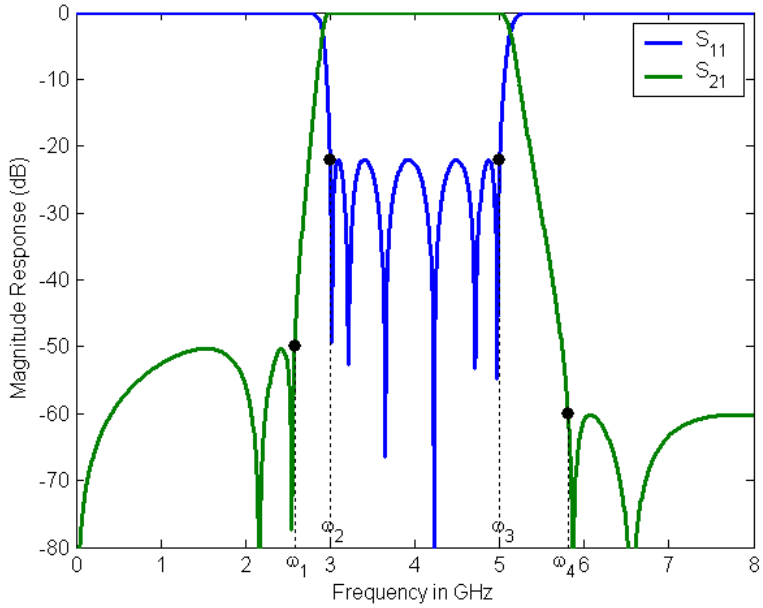

(a)

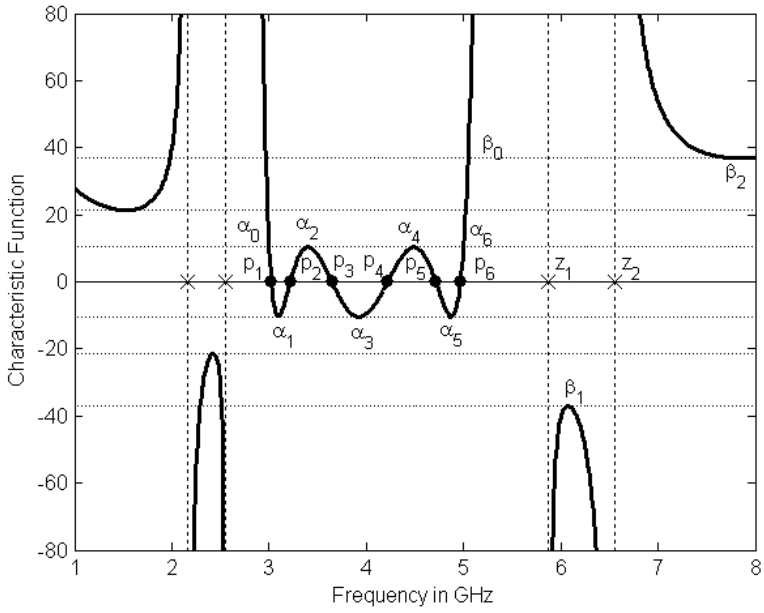

(b)

Figure 2.2. (a) Typical responses of a bandpass filter network. (b) Typical responses of a characteristic function including all critical frequency points in bandpass domain.

Because the real and/or complex transmission zeros, (if any are present), and the order p of the frequency variable ω in (2.8) are prescribed, using

$$D(\omega) = \omega^p \prod_{i=1}^{L} (\omega^2 - c_i^2) \prod_{i=1}^{K} (\omega^4 + d_i\, \omega^2 + e_i\,) \tag{2.10}$$

the characteristic function $C(j\omega)$ in (2.8) can be re-defined as

$$C(\,j\omega) = \frac{F(\,j\omega)}{P(\,j\omega)} = \frac{\prod_{i=1}^{N} (\omega^2 - p_i^2)}{\prod_{j=1}^{M} (\omega^2 - z_j^2) D(\omega)} \tag{2.11}$$

The algorithm to solve the characteristic function in (2.11) employs an iteration process to recursively find the locations of the zeros and poles. Hence, the iteration process for obtaining the optimum filtering function starts with the initial guess of a set of zeros $\{z_j\}$ and poles $\{p_i\}$. The critical frequencies, at which $C(\omega)$ has its extrema, are determined by solving the roots of the derivative of $C(\omega)$

$$\frac{dC(\omega)}{d\omega} = \frac{d}{d\omega}\frac{F(\omega)}{P(\omega)} = \frac{F'(\omega)P(\omega) - F(\omega)P'(\omega)}{P^2(\omega)} \tag{2.12}$$

namely, solving

$$F'(\omega)P(\omega) - F(\omega)P'(\omega) = 0 \tag{2.13}$$

A typical response curve of the characteristic function $C(\omega)$ is shown in Fig. 2.2 (b), which exactly corresponds to the responses of the bandpass filter network shown in Fig. 2.2 (a). Let the roots of equation (2.13), which should be located within filter passband be α_1, α_2, …, α_{N-1}. Also, let α_0 and α_N represent two passband edge equiripple points that are pre-defined, namely, ω_2 and ω_3 respectively. Each pole of

p's should lie between two successive α's as shown in Fig. 2.2 (b), i.e., $\alpha_{l-1} < p_l < \alpha_l, \quad l = 1,2,\ldots,N-1$, or

$$\alpha_0 < p_1 < \alpha_1 < p_2 < \alpha_2 < \cdots < \alpha_{N-1} < p_N < \alpha_N \tag{2.14}$$

With the initial guess of poles p's, the absolute values of $C(\omega)$ at α's are usually not equal. Therefore, the updated values of p's are required to find for an updated $C(\omega)$, which will approach closer to an equiripple performance, according to the solved values of $C(\omega)$ at α's. Now, let $C_0(\omega)$ be the initial characteristic function and $C_1(\omega)$ be updated one with a new value p'_l replacing the old p_l

$$C_0(\omega) = (\omega^2 - p_l^2)\frac{\prod_{i=1, i\neq l}^{N}(\omega^2 - p_i^2)}{\prod_{j=1}^{M}(\omega^2 - z_j^2)D(\omega)} \tag{2.15}$$

$$C_1(\omega) = (\omega^2 - p_l'^2)\frac{\prod_{i=1, i\neq l}^{N}(\omega^2 - p_i^2)}{\prod_{j=1}^{M}(\omega^2 - z_j^2)D(\omega)} \tag{2.16}$$

In (2.16), p'_l will be used to force $C_1(\omega)$ to have equal absolute values at α_{l-1} and α_l, namely,

$$C_1(\alpha_{l-1}) = -C_1(\alpha_l) \tag{2.17}$$

Substituting (2.16) into (2.17) yields

$$(\alpha_{l-1}{}^2 - p_l'^2)\frac{\prod_{i=1, i\neq l}^{N}(\alpha_{l-1}{}^2 - p_i^2)}{\prod_{j=1}^{M}(\alpha_{l-1}{}^2 - z_j^2)D(\alpha_{l-1})} = -(\alpha_l{}^2 - p_l'^2)\frac{\prod_{i=1, i\neq l}^{N}(\alpha_l{}^2 - p_i^2)}{\prod_{j=1}^{M}(\alpha_l{}^2 - z_j^2)D(\alpha_l)} \tag{2.18}$$

From (2.15)

$$\frac{\prod_{i=1,\, i\neq l}^{N}(\alpha_{l-1}{}^2 - p_i^2)}{\prod_{j=1}^{M}(\alpha_{l-1}{}^2 - z_j^2)D(\alpha_{l-1})} = \frac{C_0(\alpha_{l-1})}{(\alpha_{l-1}{}^2 - p_l^2)} \tag{2.19}$$

$$\frac{\prod_{i=1,\, i\neq l}^{N}(\alpha_l{}^2 - p_i^2)}{\prod_{j=1}^{M}(\alpha_l{}^2 - z_j^2)D(\alpha_l)} = \frac{C_0(\alpha_l)}{(\alpha_l{}^2 - p_l^2)} \tag{2.20}$$

then substituting (2.19) and (2.20) into (2.18) yields

$$\frac{(\alpha_{l-1}{}^2 - p_l'^2)}{(\alpha_{l-1}{}^2 - p_l^2)} C_0(\alpha_{l-1}) = -\frac{(\alpha_l{}^2 - p_l'^2)}{(\alpha_l{}^2 - p_l^2)} C_0(\alpha_l) \tag{2.21}$$

Therefore, p'_l can be solved as

$$p_i'^2 = \frac{\alpha_{l-1}{}^2(\alpha_l{}^2 - p_l^2)C_0(\alpha_{l-1}) + \alpha_l{}^2(\alpha_{l-1}{}^2 - p_l^2)C_0(\alpha_l)}{(\alpha_l{}^2 - p_l^2)C_0(\alpha_{l-1}) + (\alpha_{l-1}{}^2 - p_l^2)C_0(\alpha_l)} \tag{2.22}$$

Now, $C_l(\omega)$ has equal absolute values at α_{l-1} and α_l.

For one stopband, for example, the upper stopband in Fig. 2.2 (b), let the roots of (2.13) which should be located within corresponding stopband be β_1, β_2, …, β_U, where U is the number of zeros in this stopband. Also, let β_0 represents pre-defined band edge equiripple point, namely, ω_4 at the beginning. Each zero of z's should lie between two successive β's as shown in Fig. 2.2 (b), i.e., $\beta_{l-1} < z_l < \beta_l, \quad l = 1, 2, \ldots, U$

or

$$\beta_0 < z_1 < \beta_1 < z_2 < \beta_2 < \cdots < \beta_{U-1} < z_U < \beta_U \tag{2.23}$$

Similarly to the case in the passband, the objective here is to find an updated value of z's for an updated $C(\omega)$, which will approach closer to an equiripple performance, according to the solved values of $C(\omega)$ at β's. The updated characteristic function can be expressed as

$$C_1(\omega) = \frac{1}{\omega^2 - z_l'^2} \frac{\prod_{i=1}^{N}(\omega^2 - p_i^2)}{\prod_{j=1,\, j\neq l}^{M}(\omega^2 - z_j^2)D(\omega)} \tag{2.24}$$

where z'_l is a new zero replacing the old z_l in $C_0(\omega)$, and will be used to force $C_1(\omega)$ to have equal absolute values at β_{l-1} and β_l, namely,

$$C_1(\beta_{l-1}) = -C_1(\beta_l) \tag{2.25}$$

Substituting (2.24) into (2.25) yields

$$\frac{1}{\beta_{l-1}^2 - z_l'^2} \frac{\prod_{i=1}^{N}(\beta_{l-1}^2 - p_i^2)}{\prod_{j=1,\, j\neq l}^{M}(\beta_{l-1}^2 - z_j^2)D(\beta_{l-1})} = -\frac{1}{\beta_l^2 - z_l'^2} \frac{\prod_{i=1}^{N}(\beta_l^2 - p_i^2)}{\prod_{j=1,\, j\neq l}^{M}(\beta_l^2 - z_j^2)D(\beta_l)} \tag{2.26}$$

Thus, following some mathematical derivation,

$$\frac{\beta_{l-1}^2 - z_l^2}{\beta_{l-1}^2 - z_l'^2} C_0(\beta_{l-1}) = -\frac{\beta_l^2 - z_l^2}{\beta_l^2 - z_l'^2} C_0(\beta_l) \tag{2.27}$$

which solves

$$z_l'^2 = \frac{\beta_l^2(\beta_{l-1}^2 - z_l^2)C_0(\beta_{l-1}) + \beta_{l-1}^2(\beta_l^2 - z_l^2)C_0(\beta_l)}{(\beta_{l-1}^2 - z_l^2)C_0(\beta_{l-1}) + (\beta_l^2 - z_l^2)C_0(\beta_l)} \tag{2.28}$$

Table 2.1. Roots of Polynomials (in GHz)

	Roots of *P(s)*	Roots of *F(s)*	Roots of *E(s)*
1	±j2.1620	±j3.0227	-0.0859±j2.9257
2	±j2.5460	±j3.2189	-0.3099±j3.0849
3	±j5.8692	±j3.6470	-0.5866±j3.5468
4	±j6.5586	±j4.2238	-0.6390±j4.2822
5		±j4.7154	-0.4002±j4.8562
6		±j4.9689	-0.1237±j5.1009

One count of iteration to obtain an updated characteristic function is completed once all of the updated zeros $\{z_j\}$ and poles $\{p_i\}$ are found for all passbands and stopbands. The process will go back to (2.13) to find new critical frequency points by using the updated characteristic function. The iteration will be terminated if an equiripple performance according to acceptable tolerance is simultaneously achieved at all critical frequency points. Otherwise, the iteration process will continue to find the next characteristic function. The convergence of this iteration process is guaranteed using above technique, and usually less than 30 iterations are required depending on the established tolerance.

Once the characteristic function is obtained, it is straightforward to find filter transfer and reflection functions in (2.1) through the relationship in (2.3), subjecting to the realizable conditions. Thereafter, knowing the scattering parameters [*S*], the impedance matrix [*Z*] of the bandpass filter network may be obtained using

$$\begin{bmatrix} z_{11} & z_{12} \\ z_{21} & z_{22} \end{bmatrix} = Z_0 \begin{bmatrix} \dfrac{(1+S_{11})(1-S_{22})+S_{12}S_{21}}{(1-S_{11})(1-S_{22})-S_{12}S_{21}} & \dfrac{2S_{12}}{(1-S_{11})(1-S_{22})-S_{12}S_{21}} \\ \dfrac{2S_{21}}{(1-S_{11})(1-S_{22})-S_{12}S_{21}} & \dfrac{(1-S_{11})(1+S_{22})+S_{12}S_{21}}{(1-S_{11})(1-S_{22})-S_{12}S_{21}} \end{bmatrix} \quad (2.29)$$

If the polynomial *E(s)* can be expressed as

$$E(s) = E_e(s) + E_o(s) \tag{2.30}$$

where $E_e(s)$ is even polynomial, and $E_o(s)$ is odd polynomial, the impedance matrix [Z] can be derived after some mathematical manipulation as:

$$\begin{bmatrix} z_{11} & z_{12} \\ z_{21} & z_{22} \end{bmatrix} = Z_0 \begin{bmatrix} \dfrac{E_o(s)}{E_e(s)-F(s)} & \dfrac{P(s)/\varepsilon}{E_e(s)-F(s)} \\ \dfrac{P(s)/\varepsilon}{E_e(s)-F(s)} & \dfrac{E_o(s)}{E_e(s)-F(s)} \end{bmatrix} \tag{2.31}$$

If the characteristic impedance Z_0 at ports is assumed to be 1 Ω, the impedance matrix [Z] can be expressed in a form of partial fraction expansion:

$$\begin{bmatrix} z_{11} & z_{12} \\ z_{21} & z_{22} \end{bmatrix} = \sum_{k=1}^{n} \frac{2s}{s^2 \pm \Omega_k'^2} \begin{bmatrix} r_{11,k} & r_{12,k} \\ r_{21,k} & r_{22,k} \end{bmatrix} \tag{2.32}$$

To illustrate the procedure, the numerical technique will be applied to a sixth degree filter with an equiripple return loss level of 22 dB and four transmission zeros at lower and upper stopbands (two at each stopband). The transmission zeros are chosen to give equiripple attenuation lobe levels about 50 dB and 60 dB at lower and upper stopbands, respectively. The center frequency f_0 is 4 GHz, and the bandwidth is 2 GHz, which corresponds to a 50% relative bandwidth. Thus, the prescribed equiripple frequency points ω_1-ω_4 are 2.58 GHz, 3 GHz, 5 GHz, and 5.81 GHz, respectively.

The procedure starts with an initial guess of a set of zeros $\{z_j\}$ and poles $\{p_i\}$, the roots of polynomials $P(s)$ and $F(s)$, respectively. The location of initial values of $\{z_j\}$ and $\{p_i\}$ can be evenly distributed at the filter stopband and passband, respectively.

The convergence condition of the iteration process is set as a test function of the difference of ripple levels at critical frequency points (the goal is to have equal-ripple level in the filter passband and stopband). Within few iteration counts, the process is dramatically converged. When the value of the test function is smaller than a pre-set value, the iteration process will stop. The roots of all polynomials are given in Table 2.1. Moreover, the value of constant ε in (2.1) is 1.5316, and the order p in (2.8) is one in this example. The transfer and reflection functions of this example have been plotted in Fig. 2.2 (a). Note that the approximation problem is directly solved in the bandpass domain, thus the imaginary values of the roots of the polynomials *F(s)* and *P(s)* are exactly located at the reflection zeros and transmission zeros, respectively on the responses in Fig. 2.2 (a).

2.3 COUPLING MATRIX SYNTHESIS FOR NARROW-BAND FILTERS

2.3.1 Overview

In this section, we examine the existing coupling matrix representation of multi-coupled resonators filter circuit model with frequency independent couplings for narrow-band microwave filter applications.

In the early 1970s, Atia *et al.* [7] introduced the concept of the coupling matrix as applied to the synthesis and design of multiple coupled cavity microwave filters. The circuit model is comprised of N inter-coupled lumped-element series resonators as shown in Fig. 2.3. The couplings among these resonators exist in an arbitrary way, and are represented by the frequency independent coupling impedance matrix jM. The assumption of frequency independent couplings is only valid over a narrow frequency band. Therefore, the filter bandwidth realized by this circuit model is limited to narrow bandpass filter with typical relative bandwidth (bandwidth / center frequency) less than five percent.

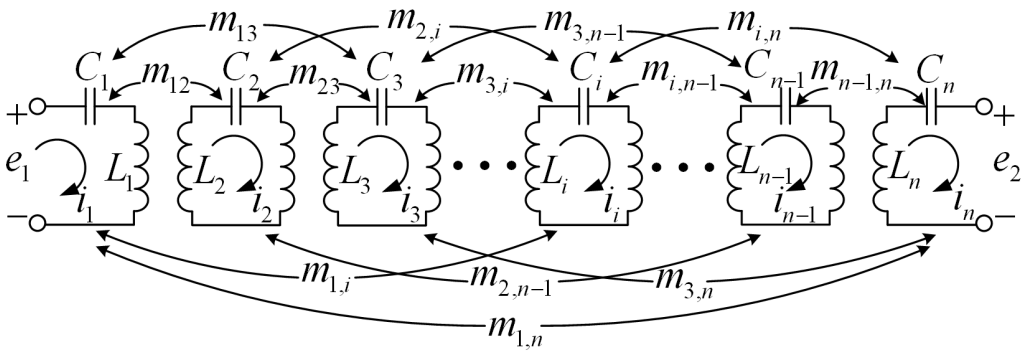

Figure 2.3. General two-port circuit model of multi-coupled resonators filter network with frequency independent couplings.

2.3.2 Circuit Analysis and Coupling Matrix Synthesis

Kirchhoff's law is applied to the loop currents in the series resonators of the circuit shown in Fig. 2.3, leading to a set of equations which may be represented in a matrix form:

$$[e] = [Z] \cdot [J] \tag{2.33}$$

where [*Z*] is the impedance matrix of the *N*-loop filter circuit network plus its terminations, and

$$[e] = e_s[1, 0, 0, \ldots, 0]^t$$

$$[Z] = [\, jM + sI + R]$$

$$[J] = [i_1, i_2, i_3, \ldots, i_N]^t \tag{2.34}$$

where $[.]^t$ denotes matrix transpose and I is the identity matrix, e_s is the source voltage, and i_1, i_2, … , i_N are the currents in each of the N loops. The impedance matrix $[Z]$ itself is the sum of three $N \times N$ matrices.

The matrix R is the $N \times N$ matrix with all entries zero, except the first element is equal to the source impedance R_s and the last element is equal to the load impedance R_L. And the coupling matrix M is the $N \times N$ reciprocal matrix containing the values of mutual couplings between resonators and having the form:

$$M = \begin{bmatrix} M_{1,1} & M_{1,2} & M_{1,3} & \cdots & M_{1,N} \\ M_{1,2} & M_{2,2} & M_{2,3} & & \\ M_{1,3} & & \ddots & & \\ \vdots & & & \ddots & M_{N-1,N} \\ M_{1,N} & & & M_{N-1,N} & M_{NN} \end{bmatrix} \tag{2.35}$$

The synthesis procedures for obtaining the values of coupling matrix have been clearly presented in [8] in detail. In brief, the key steps in solving the current synthesis problem include: solving the inverse problem of the impedance matrix to obtain the admittance matrix $[Y]$ of the multiple coupled resonators filter network, generating another admittance matrix $[Y]$ in a partial fraction expansion form from the filtering characteristic polynomials $E(s)$, $F(s)$ and $P(s)/\varepsilon$, and finally relating these two admittance matrices by identifying the corresponding elements in order to solve the coupling matrix in an analytical manner.

In general, all the entries in the coupling matrix M are nonzero. If the coupling is between the resonators in sequence, $M_{i,i+1}$, it is known as a mainline coupling. For the

entries on the main diagonal, $M_{i,i}$, they are named as self-couplings. Whereas, all the other couplings between non-sequentially numbered resonators are referred to as cross couplings.

2.3.3 Coupling Matrix Reconfiguration

It is clear that there is no practical way to realize and implement a coupling matrix with all nonzero entries into a physical structure with realizable dimensions. Therefore, a common practice is to eliminate the unwanted couplings with a sequence of similarity transformations (also known as rotations) in order to obtain a coupling matrix with a minimal number of couplings in a more convenient form.

A similarity transformation on an $N \times N$ coupling matrix is given as follows:

$$M_1 = H \cdot M_0 \cdot H^t \tag{2.36}$$

where M_0 is the original matrix, M_1 is the transformed matrix, and the rotation matrix H has the same dimensions $N \times N$ and is defined as an identity matrix with a pivot [i, j] ($i \neq j$), except of the following elements having special values:

$$H_{i,i} = H_{j,j} = \cos\theta \tag{2.37a}$$

$$H_{i,j} = -H_{j,i} = -\sin\theta \tag{2.37b}$$

where the angle θ is defined as the rotation angle. All other entries apart from the principal diagonal in the rotation matrix H are zero.

In using the similarity transformation, the eigenvalues and eigenvectors of the transformed matrix M are preserved, so that the transformed matrix has exactly the same transfer and reflection characteristics as the original matrix. Moreover, given the pivot $[i, j]$ $(i \neq j)$ for the similarity transformation, only those elements in the rows and columns i and j may possibly be affected by the transformation. All other elements retain their previous values. And if two elements facing each other across the rows or columns of the pivot are both zero before the transformation, they will still be zero thereafter.

In order to annihilate a specific element in the coupling matrix, the rotation angle must be properly chosen for a similarity transformation at pivot $[i, j]$ $(i \neq j)$ as follows:

$$\theta = \tan^{-1}(M_{ik} / M_{jk}), \qquad \text{for the } k\text{th element in row } i \qquad (2.38a)$$

$$\theta = -\tan^{-1}(M_{jk} / M_{ik}), \qquad \text{for the } k\text{th element in row } j \qquad (2.38b)$$

$$\theta = \tan^{-1}(M_{ki} / M_{kj}), \qquad \text{for the } k\text{th element in column } i \qquad (2.38c)$$

$$\theta = -\tan^{-1}(M_{kj} / M_{ki}), \qquad \text{for the } k\text{th element in column } j \qquad (2.38d)$$

Usually, a sequence of rotations is required to apply on the full coupling matrix M resulting from the synthesis procedures previously described, and progressively to annihilate the unrealizable elements to reach a convenient matrix topology.

Many filter network topologies have been extensively studied and well published in the literature based on analytical or numerical procedures [24]. Some filter topologies

have found numerous applications throughout industry, and certain advanced topologies can even provide desirable filter performance.

2.4 MULTI-COUPLED SERIES RESONATORS FILTER NETWORK WITH FREQUENCY DEPENDENT COUPLINGS

2.4.1 Overview

Rigorous synthesis methods of narrow-band multi-coupled resonator filters with frequency independent couplings have been discussed in previous section. As the filter relative bandwidth becomes wider, the circuit model of frequency independent coupling matrix will no longer accurately reproduce the electromagnetic responses of a physical filter structure obtained by electromagnetic simulation. It is known that the coupling elements in microwave structures behave as either capacitances (electric field coupling) or inductances (magnetic field coupling) or a combination of both. It also has been shown in [12] that a multiple coupled-resonator filter whose couplings are linear functions of frequency can be transformed to a filter network with constant coupling coefficients.

In this section, a coupling matrix synthesis technique is presented to account for the frequency variation of the microwave coupling structures. The wideband circuit model of filter network consists of *N* series resonators arbitrarily coupled by inductors or capacitors (frequency dependent elements). The circuit analysis leads to the two-port admittance parameters of the filter in partial fraction expansion form. As discussed in Section 2.2, given filter specifications, the approximation problem can be solved by numerical techniques to determine the rational transfer and reflection

functions of the filter in the bandpass domain. The corresponding admittance parameters can be therefore extracted from the transfer and reflection functions. The synthesis of the coupling matrix representing the filter network is completed by identifying the corresponding elements in admittance parameters obtained from the circuit analysis and those from the transfer and reflection functions.

2.4.2 Circuit Analysis and Coupling Matrix Synthesis for Inductive Coupling

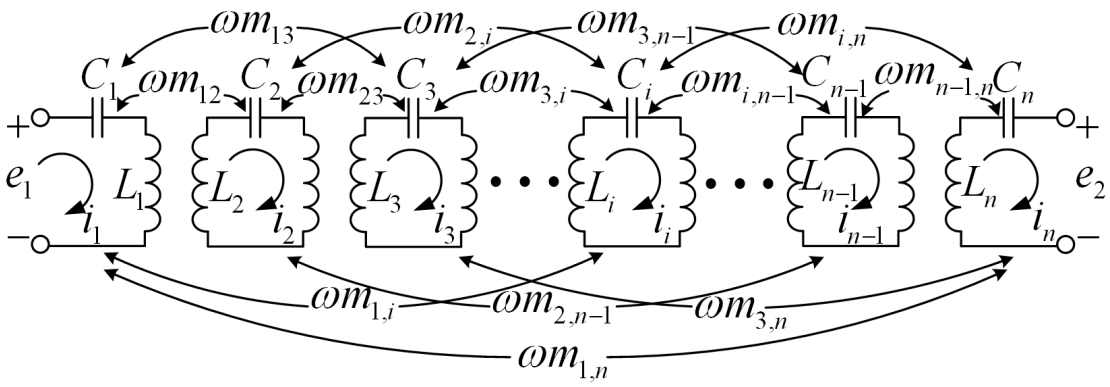

Figure 2.4. General two-port circuit model of multi-coupled series resonators filter network with frequency dependent couplings.

An equivalent circuit of a multi-coupled series resonators filter network is comprised of *N* series *LC* resonators, where couplings among these resonators exist in an arbitrary way. The coupling element between any two resonators can be purely a capacitance (electric field coupling), purely an inductance (magnetic field coupling) or a composite of both (mixed electric and magnetic field coupling). The coupling

element between resonators i and j is given by a general form ωm_{ij}-$1/\omega C_{ij}$, which obviously has dependence on the frequency variable ω.

In this section, we will consider only the cases where all the coupling elements are of one kind, i.e. either inductive or capacitive. Fig. 2.4 shows the wideband circuit model for the case with only inductive coupling elements, which are proportional to the frequency variable ω.

Kirchhoff's law is applied to the circuit model in Fig. 2.4, from which a set of loop equations can be derived and further simplified to a matrix form:

$$j\begin{bmatrix} \omega L_1 - \frac{1}{\omega C_1} & \omega m_{1,2} & \omega m_{1,3} & \cdots & \cdots & \omega m_{1,n} \\ \omega m_{2,1} & \omega L_2 - \frac{1}{\omega C_2} & \omega m_{2,3} & \cdots & \cdots & \omega m_{2,n} \\ \vdots & \vdots & \ddots & \vdots & \vdots & \vdots \\ \omega m_{l,1} & \omega m_{l,2} & \cdots & \omega L_l - \frac{1}{\omega C_l} & \cdots & \omega m_{l,n} \\ \vdots & \vdots & \vdots & \vdots & \ddots & \vdots \\ \omega m_{n,1} & \omega m_{n,2} & \cdots & \cdots & \omega m_{n,n-1} & \omega L_n - \frac{1}{\omega C_n} \end{bmatrix} \begin{bmatrix} i_1 \\ i_2 \\ \vdots \\ i_l \\ \vdots \\ i_n \end{bmatrix} = \begin{bmatrix} e_1 \\ 0 \\ \vdots \\ 0 \\ \vdots \\ -e_2 \end{bmatrix} \tag{2.39}$$

This equation can be immediately re-written in the following form:

$$j[\omega(L+M) - \frac{1}{\omega}S][i_1, i_2, \cdots, i_n]^t = [e_1, 0, \cdots, -e_2]^t \tag{2.40}$$

where

$$L = diag(L_1, L_2, \cdots, L_n)$$

$$S = diag(\frac{1}{C_1}, \frac{1}{C_2}, \cdots, \frac{1}{C_n}) = \sqrt{S} \cdot \sqrt{S}$$

$$C = diag(C_1, C_2, \cdots, C_n) = \sqrt{C} \cdot \sqrt{C} = S^{-1}$$

$$M = [m_{i,j}]_{i,j=1,2,\cdots,n \text{ and } i \neq j} \text{ where } M_{i,i} = 0 \tag{2.41}$$

Following some manipulations, equation (2.40) can be re-arranged as:

$$-j\omega\sqrt{S}[\frac{1}{\omega^2} I - \sqrt{C}(L+M)\sqrt{C}]\sqrt{S}[i_1, i_2, \cdots, i_n]^t = [e_1, 0, \cdots, -e_2]^t \tag{2.42}$$

Then keep only current vector to the left of the equal sign

$$[i_1, i_2, \cdots, i_n]^t = \frac{j}{\omega}\sqrt{C}[\frac{1}{\omega^2} I - \sqrt{C}(L+M)\sqrt{C}]^{-1}\sqrt{C}[e_1, 0, \cdots, -e_2]^t \tag{2.43}$$

Since $\sqrt{C}(L+M)\sqrt{C}$ is a real and symmetric matrix, it can be decomposed as:

$$\sqrt{C}(L+M)\sqrt{C} = T\Omega T^t = Q \tag{2.44}$$

where $\Omega = diag(\Omega_1, \Omega_2, \cdots, \Omega_n)$, Ω_i are the eigenvalues of $\sqrt{C}(L+M)\sqrt{C}$, and T is an $N \times N$ matrix with rows of orthogonal unit vectors, satisfying $T \cdot T^t = T^t \cdot T = I$. The inverse matrix in the right-hand-side of equation (2.43) can be solved as:

$$\begin{aligned}
&[\frac{1}{\omega^2} I - \sqrt{C}(L+M)\sqrt{C}]^{-1} = [\frac{1}{\omega^2} I - T\Omega T^t]^{-1} \\
&= [Tdiag(\frac{1}{\omega^2} - \Omega_1, \frac{1}{\omega^2} - \Omega_2, \cdots, \frac{1}{\omega^2} - \Omega_n)T^t]^{-1} \\
&= Tdiag(\frac{1}{\frac{1}{\omega^2} - \Omega_1}, \frac{1}{\frac{1}{\omega^2} - \Omega_1}, \cdots, \frac{1}{\frac{1}{\omega^2} - \Omega_n})T^t
\end{aligned} \tag{2.45}$$

Substituting equation (2.45) into (2.43) yields

$$[i_1, i_2, \cdots, i_n]^t$$
$$= \frac{j}{\omega}\sqrt{C}Tdiag\left(\frac{1}{\frac{1}{\omega^2}-\Omega_1}, \frac{1}{\frac{1}{\omega^2}-\Omega_1}, \cdots, \frac{1}{\frac{1}{\omega^2}-\Omega_n}\right)T^t\sqrt{C}[e_1, 0, \cdots, -e_2]^t \quad (2.46)$$

It can be shown that the matrix Q is positive definite, i.e., all of its eigenvalues are positive real numbers. Letting $\Omega_k = 1/\omega_k^2$, the two-port admittance matrix [Y] can be derived as:

$$y_{11} = \left.\frac{i_1}{e_1}\right|_{e_2=0} = \frac{j}{\omega}C_1\sum_{k=1}^{n}\frac{T_{1,k}^2}{\frac{1}{\omega^2}-\Omega_k} = -j\sum_{k=1}^{n}\frac{\omega_k C_1 T_{1,k}^2}{\frac{\omega}{\omega_k}-\frac{\omega_k}{\omega}} \quad (2.47)$$

and similarly,

$$\begin{aligned} y_{21} &= \left.\frac{i_1}{e_2}\right|_{e_1=0} = -\frac{j}{\omega}\sqrt{C_1 C_n}\sum_{k=1}^{n}\frac{T_{1,k}T_{n,k}}{\frac{1}{\omega^2}-\Omega_k} \\ &= j\sum_{k=1}^{n}\frac{\omega_k\sqrt{C_1 C_n}T_{1,k}T_{n,k}}{\frac{\omega}{\omega_k}-\frac{\omega_k}{\omega}} = y_{12} \end{aligned} \quad (2.48)$$

$$y_{22} = \left.\frac{-i_n}{e_2}\right|_{e_1=0} = \frac{j}{\omega}C_n\sum_{k=1}^{n}\frac{T_{n,k}^2}{\frac{1}{\omega^2}-\Omega_k} = -j\sum_{k=1}^{n}\frac{\omega_k C_n T_{n,k}^2}{\frac{\omega}{\omega_k}-\frac{\omega_k}{\omega}} \quad (2.49)$$

Knowing the transfer and reflection functions by solving the approximation problem in bandpass domain, the admittance parameters [Y] of the wideband filter circuit model may be obtained using

$$\begin{bmatrix} y_{11} & y_{12} \\ y_{21} & y_{22} \end{bmatrix} = Y_0 \begin{bmatrix} \dfrac{(1-S_{11})(1+S_{22})+S_{12}S_{21}}{(1+S_{11})(1+S_{22})-S_{12}S_{21}} & \dfrac{-2S_{12}}{(1+S_{11})(1+S_{22})-S_{12}S_{21}} \\ \dfrac{-2S_{21}}{(1+S_{11})(1+S_{22})-S_{12}S_{21}} & \dfrac{(1+S_{11})(1-S_{22})+S_{12}S_{21}}{(1+S_{11})(1+S_{22})-S_{12}S_{21}} \end{bmatrix} \tag{2.50}$$

If the polynomial *E(s)* can be expressed as

$$E(s) = E_e(s) + E_o(s) \tag{2.51}$$

where $E_e(s)$ is even polynomial, and $E_o(s)$ is odd polynomial, the admittance matrix [*Y*] can be derived after some mathematical manipulation as:

$$\begin{bmatrix} y_{11} & y_{12} \\ y_{21} & y_{22} \end{bmatrix} = Y_0 \begin{bmatrix} \dfrac{E_o(s)}{E_e(s)+F(s)} & \dfrac{-P(s)/\varepsilon}{E_e(s)+F(s)} \\ \dfrac{-P(s)/\varepsilon}{E_e(s)+F(s)} & \dfrac{E_o(s)}{E_e(s)+F(s)} \end{bmatrix} \tag{2.52}$$

If the characteristic admittance Y_0 at ports is assumed to be 1 (S), the admittance matrix [*Y*] can be expressed in a form of partial fraction expansion:

$$\begin{bmatrix} y_{11} & y_{12} \\ y_{21} & y_{22} \end{bmatrix} = -j\sum_{k=1}^{n} \frac{1}{\dfrac{\omega}{\omega_k'} - \dfrac{\omega_k'}{\omega}} \begin{bmatrix} r_{k11} & r_{k12} \\ r_{k21} & r_{k22} \end{bmatrix} \tag{2.53}$$

Note that it is necessary to solve again the approximation problem in the bandpass domain to accommodate the introduction of frequency dependent couplings on the wideband filter circuit model.

The two expressions for the admittance matrix [*Y*], in terms of the circuit elements of the multi-coupled series resonators filter network in equations (2.47)-(2.49), and in terms of the eigenvalues and residues from the transfer and reflection functions in

equation (2.53), may be related to identify the corresponding elements. It is seen immediately that

$$\omega_k = \omega_k' \tag{2.54a}$$

$$\omega_k C_1 T_{1,k}^2 = r_{k11} \tag{2.54b}$$

$$\omega_k \sqrt{C_1 C_n} T_{1,k} T_{n,k} = -r_{k21} \tag{2.54c}$$

$$\omega_k C_n T_{n,k}^2 = r_{k22} \tag{2.54d}$$

Since the matrix [*T*] is an orthogonal matrix as defined in (2.44), the row vectors T_{1k} and T_{nk} have the following properties:

$$\sum_{k=1}^{n} T_{1,k}^2 = 1 \text{ and } \sum_{k=1}^{n} T_{1,k} T_{n,k} = 0 \tag{2.55}$$

Substituting equation (2.55) to (2.54) yields

$$\sum_{k=1}^{n} T_{1,k}^2 = 1 = \sum_{k=1}^{n} \frac{r_{k11}}{\omega_k C_1}$$

$$\Rightarrow C_1 = \sum_{k=1}^{n} \frac{r_{k11}}{\omega_k} \tag{2.56}$$

From (2.54b),

$$T_{1,k} = \sqrt{\frac{r_{k11}}{\omega_k C_1}} \tag{2.57}$$

Following similar derivation for C_1, C_n can be found as

$$C_n = \sum_{k=1}^{n} \frac{r_{k22}}{\omega_k} \tag{2.58}$$

Knowing equations (2.56)-(2.58), $T_{n,k}$ can be solved from (2.54c) as

$$T_{n,k} = \frac{-r_{k21}}{\omega_k \sqrt{C_1 C_n} T_{1,k}} \tag{2.59}$$

With the first and last rows of the matrix [T] now determined, the remaining orthogonal rows in [T] may be constructed by a Gram-Schmidt process to fill in. As defined in (2.44), $Q = T\Omega T^t$ is now known, and from

$$T\Omega T^t = \begin{bmatrix} L_1 C_1 & m_{1,2}\sqrt{C_1 C_2} & \cdots & m_{1,n}\sqrt{C_1 C_n} \\ m_{2,1}\sqrt{C_2 C_1} & L_2 C_2 & \cdots & m_{2,n}\sqrt{C_2 C_n} \\ \vdots & \vdots & \ddots & \vdots \\ m_{n,1}\sqrt{C_n C_1} & \cdots & \cdots & L_n C_n \end{bmatrix} \tag{2.60}$$

all remaining circuit elements L_i, C_i, and m_{ij} in the multi-coupled series resonators filter network can be found. Firstly, since C_1 and C_n are already known,

$$L_1 = \frac{Q_{11}}{C_1} \text{ and } L_n = \frac{Q_{nn}}{C_n} \tag{2.61}$$

The two-port parameters determine uniquely L_1, C_1, L_n, and C_n, but others, C_2, …, C_{n-1} are arbitrary to choose. If the loop characteristic impedances

$$Z_{ok} = \sqrt{L_k / C_k} \tag{2.62}$$

where $k = 2, \ldots, n-1$, are chosen as design parameters, then

$$L_k = Z_{ok}\sqrt{Q_{kk}} \text{ and } C_k = \frac{\sqrt{Q_{kk}}}{Z_{ok}} \tag{2.63}$$

Moreover, from (2.44) and (2.60),

$$m_{i,j} = \frac{Q_{ij}}{\sqrt{C_i C_j}} \tag{2.64}$$

Thus, all of the circuit elements are synthesized.

The synthesized coupling matrix may contain all the elements. To realize a certain topology some of the matrix elements must be reduced to zero. This can be readily done using matrix rotations as in the narrow band case.

Circuit analysis and coupling matrix synthesis for the case with only capacitive coupling elements are very similar, and can be solved in a similar way.

2.4.3 Circuit Analysis and Coupling Matrix Synthesis for Capacitive Coupling

Now consider the case that the coupling element between any two resonators in Fig. 2.4 is purely a capacitance instead of a inductance as has been shown in previous sub-sections, namely, it will be *inversely* proportional to the frequency variable ω. Apply Kirchhoff's Law to the circuit mode, the following equation in matrix form can be derived similarly to (2.39):

$$
j\begin{bmatrix}
\omega L_1-\frac{1}{\omega C_1} & -\frac{1}{\omega m_{1,2}} & -\frac{1}{\omega m_{1,3}} & \cdots & \cdots & -\frac{1}{\omega m_{1,n}} \\
-\frac{1}{\omega m_{2,1}} & \omega L_2-\frac{1}{\omega C_2} & -\frac{1}{\omega m_{2,3}} & \cdots & \cdots & -\frac{1}{\omega m_{2,n}} \\
\vdots & \vdots & \ddots & \vdots & \vdots & \vdots \\
-\frac{1}{\omega m_{l,1}} & -\frac{1}{\omega m_{l,2}} & \cdots & \omega L_l-\frac{1}{\omega C_l} & \cdots & -\frac{1}{\omega m_{l,n}} \\
\vdots & \vdots & \vdots & \vdots & \ddots & \vdots \\
-\frac{1}{\omega m_{n,1}} & -\frac{1}{\omega m_{n,2}} & \cdots & \cdots & -\frac{1}{\omega m_{n,n-1}} & \omega L_n-\frac{1}{\omega C_n}
\end{bmatrix}
\begin{bmatrix} i_1 \\ i_2 \\ \vdots \\ i_l \\ \vdots \\ i_n \end{bmatrix}
=
\begin{bmatrix} e_1 \\ 0 \\ \vdots \\ 0 \\ \vdots \\ -e_2 \end{bmatrix}
\tag{2.65}
$$

This equation can be immediately re-written as:

$$
j[\omega L-\frac{1}{\omega}(S+M^C)][i_1,i_2,\cdots,i_n]^t=[e_1,0,\cdots,-e_2]^t \tag{2.66}
$$

where

$$
L=diag(L_1,L_2,\cdots,L_n)
$$

$$
S=diag(\frac{1}{C_1},\frac{1}{C_2},\cdots,\frac{1}{C_n})
$$

$$
C=diag(C_1,C_2,\cdots,C_n)=S^{-1}
$$

$$
M^C=[\frac{1}{m_{i,j}}]_{i,j=1,2,\cdots,n\ and\ i\neq j}\ where\ M^C_{i,i}=0 \tag{2.67}
$$

After some manipulation, equation (2.66) can be re-arranged as:

$$
[i_1,i_2,\cdots,i_n]^t=-j\omega\sqrt{P}[\omega^2 I-\sqrt{P}(S+M^C)\sqrt{P}]^{-1}\sqrt{P}[e_1,0,\cdots,-e_2]^t \tag{2.68}
$$

where

$$P = diag(\frac{1}{L_1}, \frac{1}{L_2}, \cdots, \frac{1}{L_n}) = L^{-1} \tag{2.69}$$

Since $\sqrt{P}(S + M^C)\sqrt{P}$ is a real and symmetric matrix, it also can be decomposed as:

$$\sqrt{P}(S + M^C)\sqrt{P} = T\Omega^C T^t = Q^C \tag{2.70}$$

where $\Omega^C = diag(\Omega_1^C, \Omega_2^C, \cdots, \Omega_n^C)$, Ω_1^C are the eigenvalues of $\sqrt{P}(S + M^C)\sqrt{P}$, and again, T is an $N \times N$ matrix with rows of orthogonal unit vectors, satisfying $T \cdot T^t = T^t \cdot T = I$. The inverse matrix in the right-hand-side of (2.68) can be solved as:

$$\begin{aligned} &[\omega^2 I - \sqrt{P}(S + M^C)\sqrt{P}]^{-1} = [\omega^2 I - T\Omega^C T^t]^{-1} \\ &= [Tdiag(\omega^2 - \Omega_1^C, \omega^2 - \Omega_2^C, \cdots, \omega^2 - \Omega_n^C)T^t]^{-1} \\ &= Tdiag(\frac{1}{\omega^2 - \Omega_1^C}, \frac{1}{\omega^2 - \Omega_2^C}, \cdots, \frac{1}{\omega^2 - \Omega_n^C})T^t \end{aligned} \tag{2.71}$$

Substituting (2.71) into (2.68) yields:

$$\begin{aligned} &[i_1, i_2, \cdots, i_n]^t \\ &= -j\omega\sqrt{P}Tdiag(\frac{1}{\omega^2 - \Omega_1^C}, \frac{1}{\omega^2 - \Omega_2^C}, \cdots, \frac{1}{\omega^2 - \Omega_n^C})T^t\sqrt{P}[e_1, 0, \cdots, -e_2]^t \end{aligned} \tag{2.72}$$

It can be shown that the matrix Q^C is positive definite, i.e., all of its eigenvalues are positive real numbers. Letting $\Omega_k^C = \omega_k^2$, the two-port admittance matrix [Y] can be derived as:

$$y_{11} = \left.\frac{i_1}{e_1}\right|_{e_2=0} = -j\omega\frac{1}{L_1}\sum_{k=1}^{n}\frac{T_{1,k}^2}{\omega^2-\Omega_k^C} = -j\sum_{k=1}^{n}\frac{\frac{1}{\omega_k}\frac{1}{L_1}T_{1,k}^2}{\frac{\omega}{\omega_k}-\frac{\omega_k}{\omega}} \tag{2.73}$$

$$\begin{aligned} y_{21} &= \left.\frac{i_1}{e_2}\right|_{e_1=0} = j\omega\frac{1}{\sqrt{L_1L_n}}\sum_{k=1}^{n}\frac{T_{1,k}T_{n,k}}{\omega^2-\Omega_k^C} \\ &= j\sum_{k=1}^{n}\frac{\frac{1}{\omega_k}\frac{1}{\sqrt{L_1L_n}}T_{1,k}T_{n,k}}{\frac{\omega}{\omega_k}-\frac{\omega_k}{\omega}} = y_{12} \end{aligned} \tag{2.74}$$

$$y_{22} = \left.\frac{-i_n}{e_2}\right|_{e_1=0} = -j\omega\frac{1}{L_n}\sum_{k=1}^{n}\frac{T_{n,k}^2}{\omega^2-\Omega_k^C} = -j\sum_{k=1}^{n}\frac{\frac{1}{\omega_k}\frac{1}{L_n}T_{n,k}^2}{\frac{\omega}{\omega_k}-\frac{\omega_k}{\omega}} \tag{2.75}$$

The coupling matrix synthesis is carried out in a similar manner as shown in previous sub-section. Identifying the corresponding elements in equation (2.53) and equations (2.73)-(2.75), it is seen immediately that

$$\begin{aligned} &\omega_k = \omega_k' \\ &\frac{1}{\omega_k}\frac{1}{L_1}T_{1,k}^2 = r_{k11} \\ &\frac{1}{\omega_k}\frac{1}{\sqrt{L_1L_n}}T_{1,k}T_{n,k} = -r_{k21} \\ &\frac{1}{\omega_k}\frac{1}{L_n}T_{n,k}^2 = r_{k22} \end{aligned} \tag{2.76}$$

Since the matrix [*T*] is an orthogonal matrix as defined in (2.70), the row vectors $T_{1,k}$ and $T_{n,k}$ have the following properties:

$$\sum_{k=1}^{n} T_{1,k}^2 = 1 \text{ and } \sum_{k=1}^{n} T_{1,k} T_{n,k} = 0 \tag{2.77}$$

Substituting equation (2.77) into (2.76) yields:

$$\sum_{k=1}^{n} T_{1,k}^2 = 1 = \sum_{k=1}^{n} r_{k11} \omega_k L_1$$

$$\Rightarrow L_1 = \frac{1}{\sum_{k=1}^{n} r_{k11} \omega_k} \tag{2.78}$$

Also,

$$T_{1,k} = \sqrt{r_{k11} \omega_k L_1} \tag{2.79}$$

Following similar derivation for L_1, L_n can be found as

$$L_n = \frac{1}{\sum_{k=1}^{n} r_{k22} \omega_k} \tag{2.80}$$

Knowing equations (2.78)-(2.80), $T_{n,k}$ can be solved as

$$T_{n,k} = \frac{-r_{k21} \omega_k \sqrt{L_1 L_n}}{T_{1,k}} \tag{2.81}$$

With the first and last rows of the matrix [T] now determined, the remaining orthogonal rows in [T] may be constructed by a Gram-Schmidt process to fill in. As defined in (2.70), $Q^C = T \Omega^C T^t$ is now known, and from

$$T\Omega^{C}T^{t}=\begin{bmatrix} \frac{1}{L_1C_1} & \frac{1}{M^{C}_{1,2}\sqrt{L_1L_2}} & \cdots & \frac{1}{M^{C}_{1,n}\sqrt{L_1L_n}} \\ \frac{1}{M^{C}_{2,1}\sqrt{L_2L_1}} & \frac{1}{L_2C_2} & \cdots & \frac{1}{M^{C}_{2,n}\sqrt{L_2L_n}} \\ \vdots & \vdots & \ddots & \vdots \\ \frac{1}{M^{C}_{n,1}\sqrt{L_nL_1}} & \cdots & \cdots & \frac{1}{L_nC_n} \end{bmatrix} \tag{2.82}$$

all remaining circuit elements L_i, C_i, and M^c_{ij} in the multi-coupled series resonators filter network can be found. Firstly, since L_1 and L_n are already known

$$C_1=\frac{1}{L_1Q^{C}_{11}} \text{ and } C_n=\frac{1}{L_nQ^{C}_{nn}} \tag{2.83}$$

The two-port parameters determine uniquely L_1, C_1, L_n, and C_n, but others, L_2, …, L_{n-1} are arbitrary to choose. If the loop characteristic impedances

$$Z_{ok}=\sqrt{L_k/C_k} \tag{2.84}$$

where $k = 2, \ldots, n-1$, are chosen as design parameters, then

$$L_k=\frac{Z_{ok}}{\sqrt{Q^{C}_{kk}}} \text{ and } C_k=\frac{1}{Z_{ok}\sqrt{Q^{C}_{kk}}} \tag{2.85}$$

Moreover,

$$M^{C}_{i,j}=\frac{1}{Q^{C}_{ij}\sqrt{L_iL_j}} \tag{2.86}$$

Thus, all of the circuit elements for the case that the coupling element between any two resonators in Fig. 2.4 is purely a capacitance are synthesized in this sub-section. Again, the synthesized coupling matrix may contain all the elements. To realize a

certain topology some of the matrix elements must be reduced to zero. This can be readily done using matrix rotations as in the narrow band case.

2.4.4 Limitation

The wide band circuit model in Fig. 2.4 has series *LC* resonators coupled by frequency dependent couplings. The limitation is on the physical definition of the capacitive coupling element between any two resonators. Although the mathematic derivation can be carried on for the case of purely capacitive coupling elements or for the case of the composite elements of inductive and capacitive couplings, it is then very hard to relate the synthesized coupling matrix to the physical structure when designing a filter.

Therefore, in the following sections, the circuit model with series *LC* resonators will be replaced by the circuit model with shunt *LC* resonators.

2.5 MULTI-COUPLED PARALLEL RESONATORS FILTER NETWORK WITH FREQUENCY DEPENDENT COUPLINGS

2.5.1 Overview

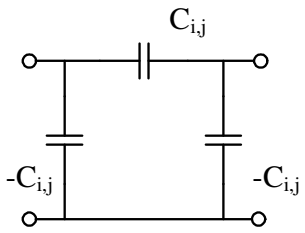

(a)

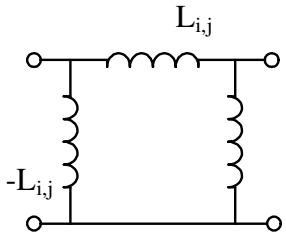

(b)

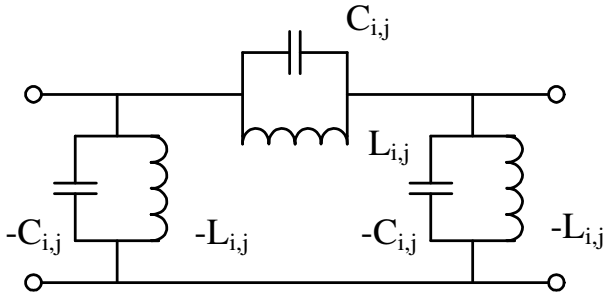

(c)

Figure 2.5. Coupling inverter elements: (a) purely capacitive, (b) purely inductive, and (c) a composite of both.

The wideband circuit model discussed in previous section is modified from series coupled resonators to parallel arrangement. This change of the circuit model makes the physical representation more suitable to model three types of coupling inverter elements, which are shown in Fig. 2.5. It is evident that these types of coupling elements are all frequency dependent.

2.5.2 Circuit Analysis

An equivalent circuit model of a multi-coupled parallel resonators filter is composed of N shunt LC resonators. Coupling elements among these resonators may exist in an arbitrary way, as shown in Fig. 2.6. For $i = 1, \ldots, N$, the resonator i consists of an inductor L_i and a capacitor C_i connected in parallel. The coupling between any two resonators is an inverter realized by a *pi* network, which can be capacitor (electric coupling), inductor (magnetic coupling), or both for composite coupling, as shown in Fig. 2.5. This model can accurately reproduce the responses of an electromagnetic structure over a very wide frequency band, provided that the number of resonators and the values of the circuit elements are properly constructed.

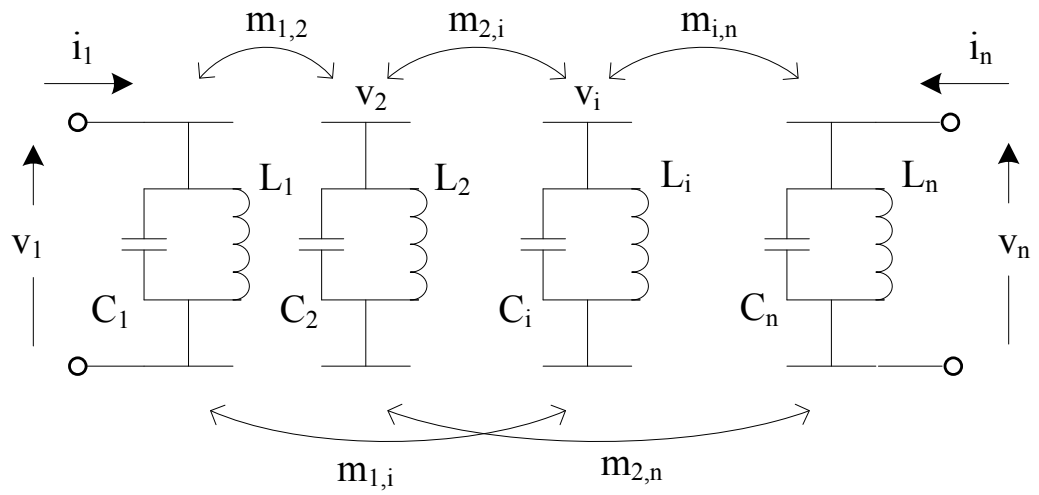

Figure 2.6. Circuit model of multicoupled resonators filter.

The node equations of this circuit model can be written as

$$\begin{bmatrix} sC_1+\dfrac{1}{sL_1} & -m_{1,2} & \cdots & -m_{1,n} \\ -m_{2,1} & sC_2+\dfrac{1}{sL_2} & \cdots & -m_{2,n} \\ \vdots & \vdots & \ddots & \vdots \\ -m_{n,1} & \cdots & -m_{n,n-1} & sC_n+\dfrac{1}{sL_n} \end{bmatrix} \begin{bmatrix} v_1 \\ v_2 \\ \vdots \\ v_n \end{bmatrix} = \begin{bmatrix} i_1 \\ 0 \\ \vdots \\ i_n \end{bmatrix} \tag{2.87}$$

where

$$m_{i,j} = sC_{i,j} + \frac{1}{sL_{i,j}}, \quad i, j = 1, 2, \ldots, n; i \neq j. \tag{2.88}$$

The node equations can also be written in the following form:

$$[s(C - M^C) + \frac{1}{s}(P - M^L)][v] = [i] \tag{2.89}$$

where

$$C = diag(C_1, C_2, \ldots, C_n)$$

$$P = diag(\frac{1}{L_1}, \frac{1}{L_2}, \ldots, \frac{1}{L_n}) = L^{-1}$$

$$M^L = [\frac{1}{L_{i,j}}], \quad i, j = 1, 2, \ldots, n; \quad i \neq j, \quad M^L_{i,i} = 0$$

$$M^C = [C_{i,j}], \quad i, j = 1, 2, \ldots, n; \quad i \neq j, \quad M^C_{i,i} = 0$$

$$[v] = [v_1, v_2, \ldots, v_n]^t$$

$$[i] = [i_1, 0, \ldots, 0, i_n]^t \tag{2.90}$$

Then, equation (2.89) can be rearranged as

$$[v] = [s(C - M^C) + \frac{1}{s}(P - M^L)]^{-1}[i] \tag{2.91}$$

The matrices $(C - M^C)$ and $(P - M^L)$ are both real symmetrical and positive definite (see [16] and Appendix A). Therefore, $(C - M^C)$ can be decomposed as

$$(C - M^C) = Q\Lambda_C Q^t \tag{2.92}$$

where $\Lambda_C = diag(\lambda_{C1}, \lambda_{C2}, \ldots, \lambda_{Cn})$, λ_{Ci} are the eigenvalues of $(C - M^C)$ (all real positive numbers) and Q is an orthogonal matrix, satisfying $Q \cdot Q^t = Q^t \cdot Q = I$. The inverse matrix in the right-hand side of (2.91) can be solved as

$$[s(C - M^C) + \frac{1}{s}(P - M^L)]^{-1} = [sQ\Lambda_C Q^t + \frac{1}{s}(P - M^L)]^{-1}$$

$$= Q\sqrt{\Lambda_C^{-1}}[sI + \frac{1}{s}\sqrt{\Lambda_C^{-1}}Q^t(P - M^L)Q\sqrt{\Lambda_C^{-1}}]^{-1}\sqrt{\Lambda_C^{-1}}Q^t \tag{2.93}$$

Let

$$A = Q\sqrt{\Lambda_C^{-1}} \text{ and } A^t = \sqrt{\Lambda_C^{-1}}Q^t \tag{2.94}$$

Substituting (2.94) into (2.93) yields

$$[s(C-M^C)+\frac{1}{s}(P-M^L)]^{-1} = A[sI+\frac{1}{s}A^t(P-M^L)A]^{-1}A^t \tag{2.95}$$

Again, it can be shown that (see [16] and the Appendix A) $A^t(P-M^L)A$ is a real symmetric and positive definite matrix, so it is possible to be decomposed as

$$A^t(P-M^L)A = T\Lambda_L T^t \tag{2.96}$$

where $\Lambda_L = diag(\Omega_1^2, \Omega_2^2, \ldots, \Omega_n^2)$, Ω_i^2 are the eigenvalues of $A^t(P-M^L)A$ (all real positive numbers) and T is an orthogonal matrix, satisfying $T \cdot T^t = T^t \cdot T = I$. Equation (2.95) now becomes

$$[s(C-M^C)+\frac{1}{s}(P-M^L)]^{-1} = A[sI+\frac{1}{s}T\Lambda_L T^t]^{-1}A^t = Bdiag(\frac{1}{s+\frac{1}{s}\Omega_i^2})B^t \tag{2.97}$$

where

$$B = AT \tag{2.98}$$

The node equation (2.91) can now be expressed as

$$[v] = Bdiag(\frac{s}{s^2+\Omega_i^2})B^t[i] \tag{2.99}$$

Thus, the two-port impedance parameters [*Z*] of the multi-coupled parallel resonators filter can be derived as

$$z_{11} = \sum_{i=1}^{n}\frac{sB_{1i}^2}{s^2+\Omega_i^2}$$

$$z_{22} = \sum_{i=1}^{n} \frac{sB_{ni}^2}{s^2 + \Omega_i^2} \tag{2.100}$$

$$z_{12} = \sum_{i=1}^{n} \frac{sB_{1i}B_{ni}}{s^2 + \Omega_i^2} = z_{21}$$

Comparing equations (2.32) and (2.100), the following parameters can easily be identified:

$$\begin{aligned} B_{1i}^2 &= 2r_{11,i} \\ B_{ni}^2 &= 2r_{22,i} \\ B_{1i}B_{ni} &= 2r_{21,i} \\ \Omega_i^2 &= \Omega_i'^2, \quad i = 1, 2, \ldots, n. \end{aligned} \tag{2.101}$$

Thus, the first and the last row of the matrix [B] are known as well as the eigenvalues Ω_i^2. The issue now is how to reconstruct the matrices [B], $(C - M^C)$, and $(P - M^L)$ from these known values in (2.101) subject to a given topology. Analytical solutions for the synthesis have been obtained for the cases where all the couplings are either inductive or capacitive. These solutions are presented in Section 2.6. For the general case where all three types of couplings exist, a numerical optimization approach is adopted and is presented in Section 2.7.

2.6 SYNTHESIS FOR ALL INDUCTIVE OR ALL CAPACITIVE COUPLINGS

2.6.1 Only Inductive Coupling Elements

For all inductive couplings, the matrix $M^C = 0$, and $Q = I$, the identity matrix. Therefore, the node equation (2.89) becomes

$$[sC + \frac{1}{s}(P - M^L)][v] = [i] \tag{2.102}$$

and the matrix B defined in (2.98) becomes

$$B = \sqrt{C^{-1}}T \tag{2.103}$$

By identifying the residues in (2.101), the following results are obtained:

$$\begin{aligned} &\frac{1}{C_1}T_{1,k}^2 = 2r_{11,k} \\ &\frac{1}{C_n}T_{n,k}^2 = 2r_{22,k} \\ &\frac{T_{1,k}T_{n,k}}{\sqrt{C_1 C_n}} = 2r_{21,k} \end{aligned} \tag{2.104}$$

The circuit elements can now be solved as follows:

$$\sum_{k=1}^{n} T_{1,k}^2 = 1 = C_1 \sum_{k=1}^{n} 2r_{11,k} \quad C_1 = \frac{1}{2\sum_{k=1}^{n} r_{11,k}} \tag{2.105}$$

$$\sum_{k=1}^{n} T_{n,k}^2 = 1 = C_n \sum_{k=1}^{n} 2r_{22,k} \quad C_n = \frac{1}{2\sum_{k=1}^{n} r_{22,k}} \tag{2.106}$$

$$\mathrm{T}_{n,k} = \sqrt{2r_{22,k}C_n} \quad \mathrm{T}_{1,k} = \frac{2r_{21,k}\sqrt{C_1 C_n}}{T_{n,k}} \tag{2.107}$$

With the first and last rows of the matrix [*T*] determined, the remaining orthogonal rows of [*T*] may be constructed by the Gram-Schmidt process or equivalent. Thus, the matrix Λ_L and the matrix [*T*] are known, as well as parameters C_1 and C_n. As defined in (2.96),

$$\sqrt{C^{-1}}(P - M^L)\sqrt{C^{-1}} = \begin{bmatrix} \frac{1}{L_1 C_1} & \frac{-1}{L_{1,2}\sqrt{C_1 C_2}} & \cdots & \frac{-1}{L_{1,n}\sqrt{C_1 C_n}} \\ \frac{-1}{L_{2,1}\sqrt{C_2 C_1}} & \frac{1}{L_2 C_2} & \cdots & \frac{-1}{L_{2,n}\sqrt{C_2 C_n}} \\ \vdots & \vdots & \ddots & \vdots \\ \frac{-1}{L_{n,1}\sqrt{C_n C_1}} & \cdots & \cdots & \frac{1}{L_n C_n} \end{bmatrix} = T\Lambda_L T^t = D \tag{2.108}$$

all remaining circuit elements in the multicoupled resonators filter can be identified. Firstly, since C_1 and C_n are already known,

$$L_1 = \frac{1}{D_{11}C_1} \text{ and } L_n = \frac{1}{D_{nn}C_n} \tag{2.109}$$

The two-port parameters determine uniquely C_1, C_n, L_1, and L_n, but others, C_2, …, C_{n-1}, are arbitrary. If the node characteristic impedances

$$Z_{ok} = \sqrt{L_k / C_k} \tag{2.110}$$

where $k = 2, \ldots, n-1$ are chosen as design parameters, then

$$L_k = \frac{Z_{ok}}{\sqrt{D_{kk}}} \text{ and } C_k = \frac{1}{Z_{ok}\sqrt{D_{kk}}} \tag{2.111}$$

Moreover,

$$L_{i,j} = \frac{-1}{D_{ij}\sqrt{C_i C_j}}, \quad i, j = 1, 2, \ldots, n; \quad i \neq j \tag{2.112}$$

Thus, all of the circuit elements and coupling elements consisting of only inductive couplings are synthesized.

The synthesized coupling matrix may contain all non-zero elements. To realize a certain topology, some of the matrix elements must be reduced to zero. This can be readily done using matrix rotations as in the narrowband case.

2.6.2 Only Capacitive Coupling Elements

For all capacitive couplings, the matrix $M^L = 0$. Following a similar process as that in all inductive couplings case, one can derive the values of all circuit elements. The node equation (2.89) now becomes

$$[s(C - M^C) + \frac{1}{s}P][v] = [i] \tag{2.113}$$

which can be re-arranged as

$$[v] = \sqrt{L}[\frac{1}{s}I + s\sqrt{L}(C - M^C)\sqrt{L}]^{-1}\sqrt{L}[i] \tag{2.114}$$

It can be shown (see [16] and Appendix A) that $\sqrt{L}(C-M^C)\sqrt{L}$ is a real symmetric and positive definite matrix. Therefore, this matrix can be decomposed as

$$\sqrt{L}(C-M^C)\sqrt{L} = T\Omega T^t \tag{2.115}$$

where $\Omega = diag(\Omega_1^2, \Omega_2^2, \ldots, \Omega_n^2)$, Ω_i^2 are the eigenvalues of $\sqrt{L}(C-M^C)\sqrt{L}$, and T is an orthogonal matrix, satisfying $TT^t = T^tT = I$. Now equation (2.114) now becomes

$$[v] = \sqrt{L}Tdiag\left(\frac{1}{\frac{1}{s}+s\Omega_1^2}, \frac{1}{\frac{1}{s}+s\Omega_2^2}, \ldots, \frac{1}{\frac{1}{s}+s\Omega_n^2}\right)T^t\sqrt{L}[i] \tag{2.116}$$

Thus, the two-port impedance parameters [*Z*] of the multi-coupled resonators filter can be derived as

$$\begin{aligned} z_{11} &= \sum_{k=1}^{n} \frac{sL_1T_{1,k}^2/\Omega_k^2}{s^2+1/\Omega_k^2} \\ z_{22} &= \sum_{k=1}^{n} \frac{sL_nT_{n,k}^2/\Omega_k^2}{s^2+1/\Omega_k^2} \\ z_{12} &= \sum_{k=1}^{n} \frac{s\sqrt{L_1L_n}T_{1,k}T_{n,k}/\Omega_k^2}{s^2+1/\Omega_k^2} = z_{21} \end{aligned} \tag{2.117}$$

The synthesis of the circuit elements for this case can be carried out in similar manner to the case in Section 2.6.1. By comparing the two-port impedance parameters [*Z*] in (2.32) and (2.117), the following parameters can be identified:

$$\frac{1}{\Omega_k^2} = \Omega_k'^2$$
$$L_1 \frac{T_{1,k}^2}{\Omega_k^2} = 2r_{11,k}$$
$$L_n \frac{T_{n,k}^2}{\Omega_k^2} = 2r_{22,k} \tag{2.118}$$
$$\sqrt{L_1 L_n} \frac{T_{1,k} T_{n,k}}{\Omega_k^2} = 2r_{21,k}$$

The circuit elements can be solved

$$L_1 = \sum_{k=1}^{n} 2r_{11,k}\Omega_k^2 \quad L_n = \sum_{k=1}^{n} 2r_{22,k}\Omega_k^2$$

$$T_{n,k} = \sqrt{\frac{2r_{22,k}\Omega_k^2}{L_n}} \quad T_{1,k} = \frac{2r_{21,k}\Omega_k^2}{\sqrt{L_1 L_n} T_{n,k}} \tag{2.119}$$

With the first and last rows of the matrix [T] determined, the remaining orthogonal rows of [T] may be constructed by the Gram-Schmidt process or equivalent. Thus, the matrix Ω and the matrix [T] are known, as well as parameters L_1 and L_n. As defined in (2.115)

$$\sqrt{L}(C - M^C)\sqrt{L} = \begin{bmatrix} L_1 C_1 & -\sqrt{L_1 L_2} C_{1,2} & \cdots & -\sqrt{L_1 L_n} C_{1,n} \\ -\sqrt{L_2 L_1} C_{2,1} & L_2 C_2 & \cdots & -\sqrt{L_2 L_n} C_{2,n} \\ \vdots & \vdots & \ddots & \vdots \\ -\sqrt{L_n L_1} C_{n,1} & \cdots & \cdots & L_n C_n \end{bmatrix} = T\Omega T^t = D \tag{2.120}$$

all remaining circuit elements in the multicoupled resonators filter can be identified.

Firstly, since L_1 and L_n are already known,

$$C_1 = \frac{D_{11}}{L_1} \text{ and } C_n = \frac{D_{nn}}{L_n} \tag{2.121}$$

The two-port parameters determine uniquely L_1, L_n, C_1 and C_n, but others, L_2, …, L_{n-1}, are arbitrary. If the node characteristic impedances

$$Z_{ok} = \sqrt{L_k / C_k} \tag{2.122}$$

where $k = 2, \ldots, n-1$ are chosen as design parameters, then

$$L_k = Z_{ok}\sqrt{D_{kk}} \text{ and } C_k = \frac{\sqrt{D_{kk}}}{Z_{ok}} \tag{2.123}$$

Moreover,

$$C_{i,j} = -\frac{D_{i,j}}{\sqrt{L_i L_j}}, \quad i, j = 1, 2, \ldots, n; \quad i \neq j \tag{2.124}$$

Thus, all of the circuit elements and coupling elements consisting of only capacitive couplings are synthesized.

Once again, the synthesized coupling matrix may contain all non-zero elements. To realize a certain topology, some of the matrix elements must be reduced to zero. This can be readily done using matrix rotations as in the narrowband case.

2.6.3 Example

To illustrate the synthesis procedure, a seventh-degree all-pole filter with 22-dB return loss is demonstrated as an example. The center frequency f_0 is 8 GHz, and the bandwidth BW is 4.8 GHz, which corresponds to a 60% relative bandwidth. The first step is to solve the approximation problem to obtain the transfer and reflection filtering functions.

Table 2.2. Matrix D Before Reduction (1e-3*)

	1	*2*	*3*	*4*	*5*	*6*	*7*
1	0.5568	-0.1504	0.1097	-0.1256	-0.0047	-0.1148	0.0000
2	-0.1504	0.3761	-0.0189	0.0600	-0.0143	-0.0645	0.1312
3	0.1097	-0.0189	0.4239	-0.0684	-0.0302	-0.1473	0.0319
4	-0.1256	0.0600	-0.0684	0.6514	-0.0654	-0.0871	0.0408
5	-0.0047	-0.0143	-0.0302	-0.0654	0.6415	-0.1818	-0.1030
6	-0.1148	-0.0645	-0.1473	-0.0871	-0.1818	0.5958	-0.1820
7	0.0000	0.1312	0.0319	0.0408	-0.1030	-0.1820	0.5568

Table 2.3. Matrix D After Reduction (1e-3*)

	1	*2*	*3*	*4*	*5*	*6*	*7*
1	0.5568	-0.2522	0	0	0	0	0
2	-0.2522	0.5538	-0.1731	0	0	0	0
3	0	-0.1731	0.5280	-0.1632	0	0	0
4	0	0	-0.1632	0.5252	-0.1632	0	0
5	0	0	0	-0.1632	0.5280	-0.1731	0
6	0	0	0	0	-0.1731	0.5538	-0.2522
7	0	0	0	0	0	-0.2522	0.5568

The roots of numerator polynomial of S_{11} or reflection zeros are (all values are in GHz) ±j5.6268, ±j5.8461, ±j6.3087, ±j7.0552, ±j8.1048, ±j9.3304, ±j10.2607. The roots of denominator polynomial of S_{11} are -0.6703±j10.8272, -1.3543±j9.4518, -1.2547±j 7.9771, -0.9239±j6.8848, -0.6044±j6.1585, -0.3374±j5.7198, -

0.1082±j5.5136. Note that this approximation problem is solved directly on the bandpass domain, therefore the imaginary values of roots of numerator polynomial of S_{11} are exactly located at the reflection zeros on the S_{11} response. The value of constant ε is 3.6243. Also, considering an inline coupling realization for this filter, the number of transmission zeros at dc, i.e., the order p in (2.8), is chosen as thirteen and the synthesis procedure for all capacitive coupling elements is applied. The conductance at the source and load port is assumed to be the matched load, for instance, 1 Ω.

Then, the values of circuit elements are identified one by one as previously explained. L_1 and L_n are equal to 0.0141 nH. After solving the matrix Ω and the matrix [T], the matrix [D] in (2.120) is listed in Table 2.2.

Since this matrix [D] is real symmetric, a reduction process by a sequence of similarity transformations can be applied to annihilate non-zero couplings to reach a practical coupling matrix. This reduction process is the same as those published in [8]. As defined in (2.95), the matrix [D] itself is independent of the frequency variable ω. By preserving the eigenvalues and first and last eigenvectors of the matrix [D] during similarity transformations, the transformed matrix will yield exactly the same characteristic function as the original matrix. Also, similarity transformations would not apply on the first and last rows and columns of the matrix [D] so that the two-port impedance parameters would not change. The matrix [D] after reduction is listed in Table 2.3. It is observed that only inline coupling elements exist, and all

coupling elements between non-adjacent resonators are annihilated by the sequence of similarity transformations determined analytically.

Using the equations (2.121)-(2.124), the L (in nH) = $diag$(0.0141, 0.0235, 0.0230, 0.0229, 0.0230, 0.0235, 0.0141). The C (in nF) = $diag$(0.0395, 0.0235, 0.0230, 0.0229, 0.0230, 0.0235, 0.0395). Note that L_i and C_i, $i = 2, ..., n-1$ are equal to each other. This is because the node characteristic impedances chosen as design parameters in (2.122) are assumed to be 1 Ohm for convenience. And the coupling values (in nF) are: C_{12} = 0.0139, C_{23} = 0.0074, C_{34} = 0.0071, C_{45} = 0.0071, C_{56} = 0.0074, and C_{67} = 0.0139. Note that all coupling elements are capacitive couplings. The filter responses obtained from polynomials and those obtained from the circuit elements are shown in Fig. 2.7. The exact match between these responses validates the synthesis process. Note that there is slight difference between this example and the first example presented in [13], since the circuit models proposed here and that in [13] are essentially dual-networks.

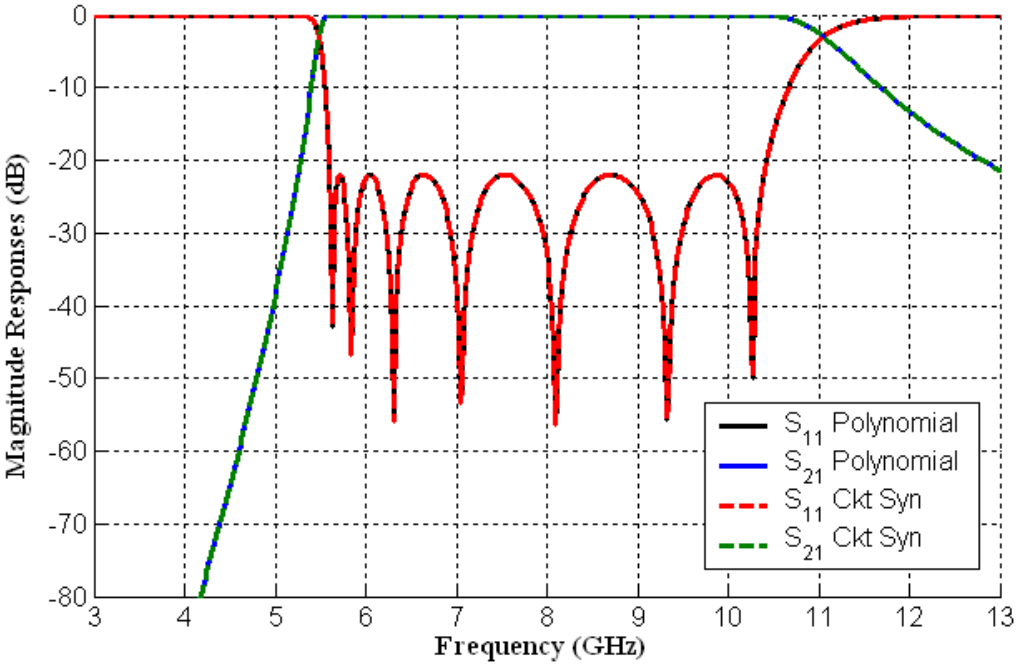

Figure 2.7. Responses of the seventh-degree all-pole filter example.

2.7 SYNTHESIS OF GENERAL CASE FOR COMPOSITE COUPLINGS

2.7.1 Numerical Technique Using Optimization

For the general case with all three types of coupling elements, a numerical optimization approach is applied to solve the synthesis problem. The algorithm is easy to implement and is described as the following procedures.

1) Start by initial matrices $(\hat{C} - \hat{M}^C)$ and $(\hat{P} - \hat{M}^L)$ that conform to the desired topology, *i.e.*, having certain zeros in their off-diagonal positions subject to the consideration in physical realization. Note that all symbols with ^ are designated as estimated values and all symbols without ^ are as the values obtained from previous synthesis techniques.

   To improve the efficiency of convergence, the initial starting matrices could be chosen from the case of synthesis with frequency independent couplings and the values of elements are evaluated at the filter center frequency.

2) Following equations (2.92), (2.94), (2.96), and (2.98), the initial calculations are expressed as

$$(\hat{C} - \hat{M}^C) = \hat{Q}\hat{\Lambda}_C\hat{Q}^t$$

$$\hat{A} = \hat{Q}\sqrt{\hat{\Lambda}_C^{-1}}$$

$$\hat{A}^t(\hat{P} - \hat{M}^L)\hat{A} = \hat{T}\hat{\Lambda}_L\hat{T}^t = \hat{T}diag(\hat{\Omega}_i^2)\hat{T}^t$$

$$\hat{B} = \hat{A}\hat{T} \qquad (2.125)$$

respectively. Thus, $\hat{\Omega}_i^2$, $\hat{B}_{1i}$ and $\hat{B}_{ni}$, $i = 1, 2, \ldots, n$, are known.

3) Form the error function defined as

$$er = \sum_{i=1}^{n}[(\hat{B}_{1i}^2 - 2r_{11,i})^2 + (\hat{B}_{1i}\hat{B}_{ni} - 2r_{12,i})^2 + (\hat{B}_{ni}^2 - 2r_{22,i})^2 + (\hat{\Omega}_i^2 - \Omega_i'^2)^2] \quad (2.126)$$

Here, $r_{11,i}$, $r_{12,i}$, $r_{22,i}$, and $\Omega_i'^2$, $i = 1, 2, \ldots, n$, are known from solving the approximation problem.

4) Use constrained optimization to minimize the error function *er* by defining the non-zero elements in $(\hat{C} - \hat{M}^C)$ and $(\hat{P} - \hat{M}^L)$ as variables. The constraint may include

$$\hat{C}_i > 0, \hat{L}_i > 0, i = 1, 2, \ldots, n$$

$$\hat{C}_{i,j} > 0, i, j = 1, 2, \ldots, n \;\&\; i \neq j \qquad (2.127)$$

5) If the value of the error function *er* is reduced to zero or becomes less than a threshold value, then the coupling matrices $(\hat{C} - \hat{M}^C)$ and $(\hat{P} - \hat{M}^L)$ are the desired ones.

The whole algorithm can be readily implemented using the programming environment of MATLAB [19]. The built-in optimization function gives fairly accurate results and fast convergence.

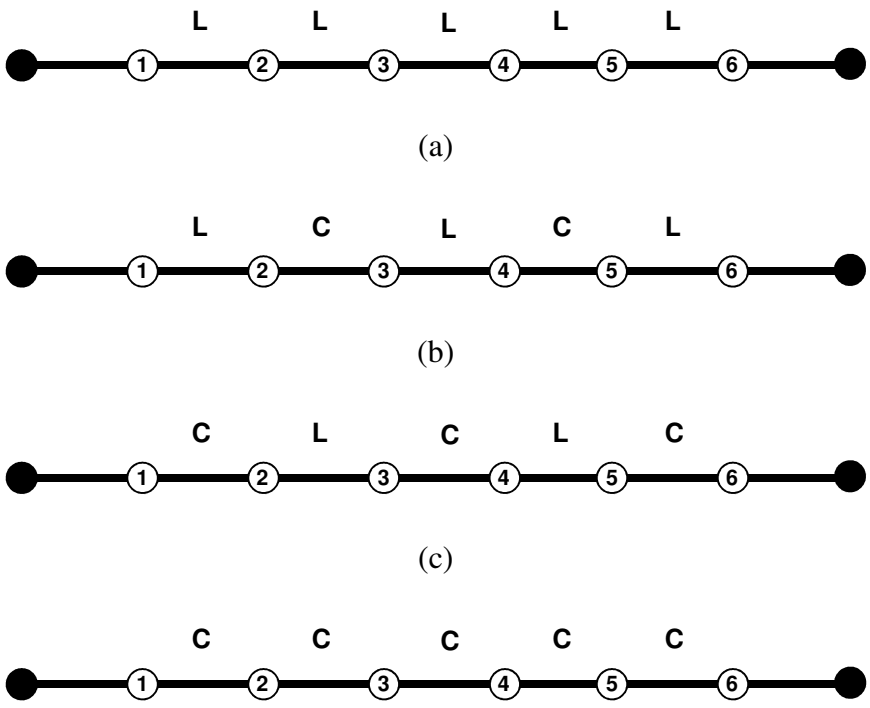

Figure 2.8. Topologies and coupling schemes of the filter synthesis examples in Section 2.7.2. The solid cycles are the source/load nodes. The empty cycles are the resonators. The solid lines are the couplings, which are denoted by the types of the coupling elements above them.

2.7.2 Filter Synthesis Examples

Table 2.4. Values of Circuit Elements from Analytical Synthesis and Numerical Optimization for the First Example in Section 2.7.2 (L in nH, C in nF, f in GHz)

	L_1 (=L_6)	L_2 (=L_5)	L_3 (=L_4)	C_1 (=C_6)	C_2 (=C_5)	C_3 (=C_4)
Synthesized	0.0097	0.0189	0.0192	0.0365	0.0189	0.0192
Optimized	0.0097	0.0256	0.0229	0.0365	0.0139	0.0161
	L_{12} (=L_{56})	L_{23} (=L_{45})	L_{34}			
Synthesized	0.0339	0.0672	0.0697			
Optimized	0.0395	0.0856	0.0832			
	f_1 (=f_6)	f_2 (=f_5)	f_3 (=f_4)	k_{12} (=k_{56})	k_{23} (=k_{45})	k_{34}
Synthesized	8.4551	8.4411	8.2933	0.4216	0.2960	0.2852
Optimized	8.4551	8.4411	8.2933	0.4216	0.2960	0.2852

Table 2.5. Normalized Values of Circuit Elements for the Set of Illustrative Examples in Section 2.7.2 (f in GHz)

	f_1 (=f_6)	f_2 (=f_5)	f_3 (=f_4)	k_{12} (=k_{56})	k_{23} (=k_{45})	k_{34}	Q_{e1} (=Q_{en})
Fist				L	L	L	
	8.4551	8.4411	8.2933	0.4216	0.2960	0.2852	1.9376
Second				L	C	L	
	8.4973	7.7317	7.6869	0.4195	-0.3189	0.2819	1.9531
Third				C	L	C	
	7.0611	7.7602	7.8055	-0.4475	0.2989	-0.3007	1.9531
Forth				C	C	C	
	7.0963	7.1081	7.2347	-0.4497	-0.3157	-0.3043	1.9376

To illustrate the numerical technique, firstly, a set of examples is presented. The filter specifications for this set of examples are identical, namely, sixth-degree 22-db return loss filters with center frequency f_0 = 8 GHz, and bandwidth BW = 4 GHz. Also, all filters in this set are realized with inline structures. The fundamental

distinction among these filters is the types of couplings and the arrangement of different types of couplings.

As the first example, the filter structure with all inductive couplings, namely, L_{12}, L_{23}, L_{34}, L_{45}, and L_{56} is realized as shown in Fig. 2.8 (a). This example is trivial because the analytic solution exists for this case. But comparing the values of circuit elements in Table 2.4, where the results from both analytic synthesis and numerical technique are given, it is clear that some values of circuit elements are different. Recall that the node characteristic impedances chosen as design parameters in (2.110) are assumed to be 1 Ohm for convenience in the analytic synthesis. There is no such assumption in the numerical optimization routine. Therefore, the values of L_i and C_i, $i = 2, \ldots, n-1$ have some freedom subject to the initial values in optimization.

However, the values of circuit elements can be normalized according to the following equations [20]:

$$f_{0i} = \frac{1}{2\pi\sqrt{L_i C_i}}$$

$$k_{ij}^{L} = \frac{1/\left(f_0 L_{ij}\right)}{\sqrt{1/\left(f_{0i} L_i\right) \cdot 1/\left(f_{0j} L_j\right)}}$$

$$k_{ij}^{C} = \frac{-f_0 C_{ij}}{\sqrt{f_{0i} C_i f_{0j} C_j}}$$

$$Q_{e1} = 2\pi f_{01} C_1, \; Q_{en} = 2\pi f_{0n} C_n \qquad (2.128)$$

The normalized values of circuit elements are also given in Table 2.5. The results from both analytic synthesis and numerical optimization are identical after normalization, because a unique class of multicoupled resonators filter is realized according to the same specification. Note that the number of transmission zero at dc, i.e., the order p in (2.8) is chosen as one for this example, where an all inductive couplings inline structure is proposed.

The second example as shown in Fig. 2.8 (b) is adopted to realize an alternation of inductive and capacitive coupling elements, namely, L_{12}, C_{23}, L_{34}, C_{45}, and L_{56}. The types of two coupling elements are changed from inductive to capacitive. Therefore, the number of transmission zeros at dc becomes five.

The third example as shown in Fig. 2.8 (c) realizes three capacitive couplings in the sequence of coupling elements, C_{12}, L_{23}, C_{34}, L_{45}, and C_{56}. Therefore, two more transmission zeros will be relocated to dc resulting in seven.

In the fourth and last example, all capacitive coupling inline structure is realized as shown in Fig. 2.8 (d). The number of transmission zeros at dc becomes eleven for this case, which is the maximum possible number, because the order of denominator polynomials must be less than the order of numerator polynomials in (2.8), which is twelve for a sixth-degree filter. Therefore, it is easy to see that, starting from the case of all inductive inline couplings, where there is only one transmission zero at dc, once the type of an inline coupling is changed from inductive to capacitive, two

transmission zeros will be relocated to dc. Up to the case of all capacitive inline couplings, the maximum number of transmission zeros will be found at dc. The rest of transmission zeros are either prescribed at the finite positions or located at infinity.

The resonators here are arranged in parallel as shown in Fig. 2.6. For its dual network, where the resonators are in series Fig. 2.4, the rule on the number of transmission zeros at dc is simply reversed. For the cases where there are non-adjacent couplings, it will be even more complicated, which is left as a future research topic.

The numerical technique introduced in this section is applied to the second and the third examples. The convergence on the error function (2.126) for all cases in this example set is very fast, and optimized values can be obtained in seconds. The normalized values of circuit elements for all four examples are summarized in Table 2.5. Note that the resonant frequencies of some resonators can be dramatically off the center frequency at 8 GHz. This shows the need to utilize the synthesis technique with frequency dependent couplings in this work when designing wideband microwave filters.

Since the filter responses obtained from the polynomials and those obtained from the synthesized circuit elements are indistinguishable, the comparisons of these responses are omitted. In Fig. 2.9, the filter responses of all four examples obtained from the numerical approach are superimposed. Within the passband, the locations of

reflection zeros are different. The selectivity of both lower and upper stopbands is also different. Thus, the choice of the number of transmission zeros at dc is critical in realizing a specific filtering function with a particular physical structure.

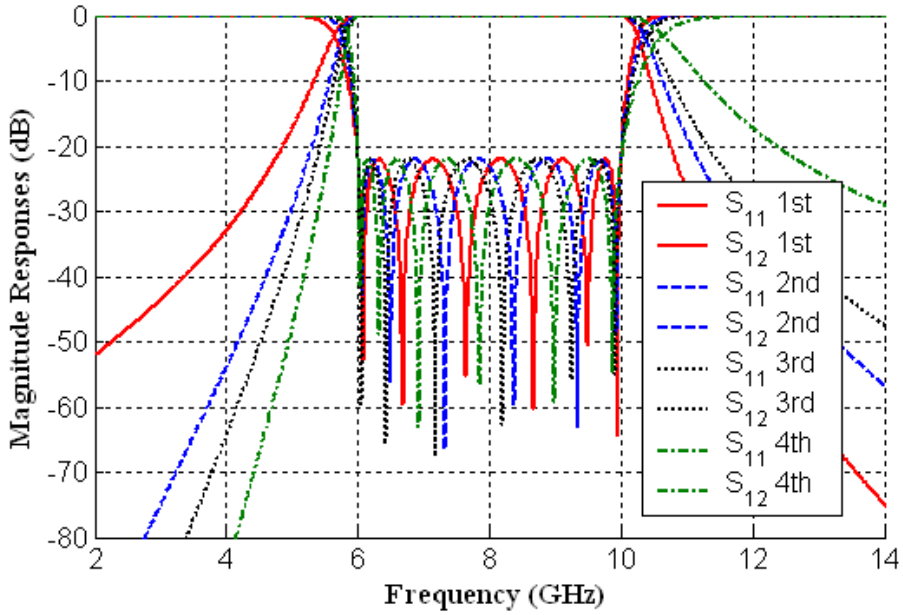

Figure 2.9. Responses of the sixth-degree filters.

2.7.3 Example with Non-Adjacent Couplings

The same filter specification in Section 2.7.2 is taken for this example with introducing two finite transmission zeros, one each at the lower and upper stop bands. Fig. 2.10 shows the topology and coupling scheme for this example. This topology is enforced during the optimization so that there is no asymmetric non-adjacent coupling, such as the couplings between the resonators 1 and 5, the resonator 2 and 4.

They could pose great challenge in filter physical design. Only one symmetric non-adjacent coupling between the resonator 2 and 5 is presented to realize two finite transmission zeros. The symmetric plane in the middle is also assumed to reduce the number of optimized variables ($f_1 = f_6, f_2 = f_5, f_3 = f_4$, $L_{12} = L_{56}$, and $L_{23} = L_{45}$).

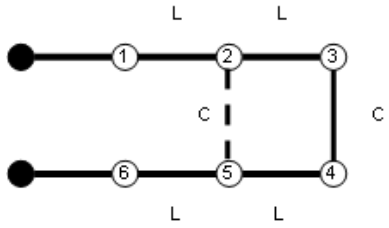

Figure 2.10. Topology and coupling scheme of the six-pole filter in Section 2.7.3.

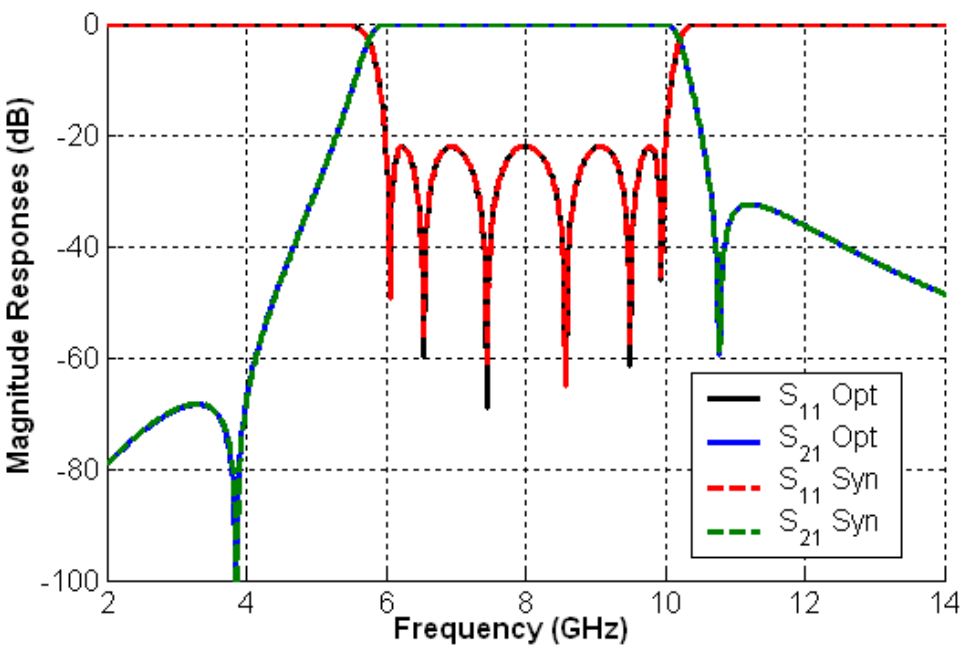

Figure 2.11. Responses of the six-pole filter in Section 2.7.3.

The number of transmission zeros at dc is chosen as three in this example. After solving the approximation problem, the optimization approach is applied. The algorithm converges in seconds in MATLAB. The synthesized values of circuit elements are: $f_1 = f_6$ = 8.4559 GHz, $f_2 = f_5$ = 8.4120 GHz, $f_3 = f_4$ = 7.6128 GHz, $k_{12} = k_{56}$ = 0.4153 (inductive), $k_{23} = k_{45}$ = 0.2828 (inductive), k_{25} = -0.0574 (capacitive), k_{34} = 0.3557 (capacitive) and $Q_{e1} = Q_{en}$ = 1.9669. One may quickly notice that the value of capacitive coupling k_{34} is positive, which is not physically feasible referring to the definition in (2.128). But this sign can be manipulated with adjacent couplings by applying matrix rotation, setting the rotation angle at 90 degree.

The filter responses calculated from the transfer and reflection functions and those from the optimized circuit elements are superimposed in Fig. 2.11. It is interesting to observe that the locations of two finite transmission zeros are not symmetric about the center frequency. On contrast in narrowband synthesis techniques, if the filter topology is symmetric and there is no non-adjacent asymmetric coupling, the finite transmission zeros must be in pairs and symmetric about the center frequency.

Chapter 3 Cascade Synthesis of Wideband Microwave Filters

3.1 INTRODUCTION

The design of microwave filters usually includes the following steps. The transfer and reflection polynomial functions representing frequency responses are first derived to satisfy design specifications. Then a filter circuit model has to been identified and synthesized according to the transfer and reflection functions. Next the actual realization and design of the physical filter layout is realized from the circuit model, aided by design software and tools. Two main categories for filter circuit model synthesis are available: one is based on the coupling matrix, which represents arbitrary electromagnetic couplings among the resonators in the circuit network. In Chapter Two, this direct coupling matrix approach has been successfully extended to wideband microwave filter synthesis. The other category is based on lumped element circuit network. In this circuit synthesis approach, the values of lumped circuit elements must be directly synthesized from the transfer and reflection functions, subject to specific topology of the circuit network.

The later approach has been covered in [26]-[30]. The synthesis of a ladder network consisting of *LC* circuit elements was introduced in [31]. However this approach

cannot cover folded circuit topologies with cross-couplings between non-adjacent resonators, which are of critical usefulness in realizing transmission zeros. A general approach presented in [32] is capable of achieving generalized Chebyshev filtering function in a lowpass prototype. But it cannot incorporate frequency dependent coupling inverters, suitable for microwave filters over a wide frequency range. Therefore, in this Chapter, this approach is further developed to enable the inclusion of frequency dependent coupling inverters in the filter circuit model, as mainline couplings or as cross-couplings.

There are three types of frequency dependent coupling inverters: purely inductive, purely capacitive, and composite of both. An important functionality of the composite type coupling is the capability of realizing a transmission zero due to the interaction of electric and magnetic fields. The synthesis technique introduced in this Chapter utilizes this feature, combined with close examination between circuit model and physical implementation.

The cascade synthesis of wideband microwave filters is a general filter synthesis approach based on the [*ABCD*] polynomial matrix, also called the cascaded / chain matrix. The overall [*ABCD*] matrix of a circuit network can be built up by cascading the [*ABCD*] matrix of each individual circuit element. The cascade synthesis can be regarded as the inverse of this procedure. Namely, the value of each individual circuit element, represented by its [*ABCD*] matrix is extracted from the overall [*ABCD*] matrix. The remainder [*ABCD*] matrix will serve as the starting point for next step.

Therefore, this synthesis technique is essentially a series of circuit element extraction in a pre-defined sequence [32]. One of the advantages over the coupling matrix approach is to provide additional freedom to manipulate individual circuit elements.

3.2 THE [*ABCD*] POLYNOMIAL MATRIX

3.2.1 Overview and Circuit Model

The wideband circuit model of a two-port lossless filter network shown in Fig. 3.1 consists of a number of *LC* resonators coupled by frequency dependent inverters in a general folded cross-coupled form.

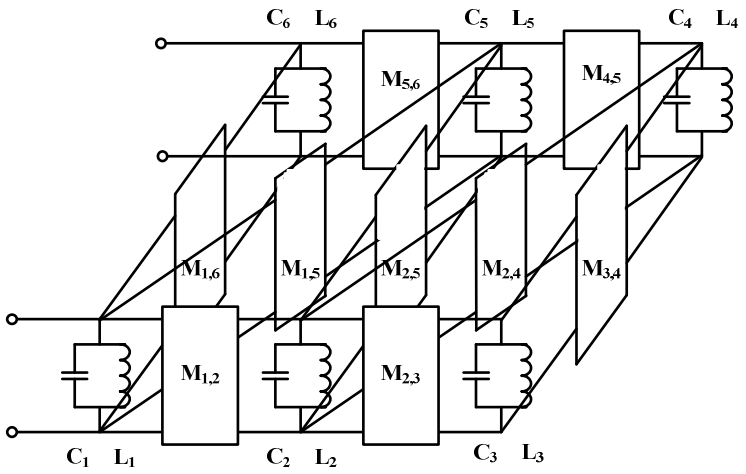

Figure 3.1. Circuit model of multicoupled resonators filter in folded form.

An early work on wideband filters in [10] discussed the qualitative behavior of the frequency responses of cross-coupled resonators filters, but the work considered only simple coupling elements without a detailed synthesis procedure. In [22]-[23], by putting a frequency invariant reactance in shunt with a capacitor, canonical asymmetric lowpass prototype filter having complex coefficients in the transfer and reflection polynomials may be synthesized. Meanwhile, the coupling elements are

still frequency independent inverters. Therefore, a comprehensive study on wideband filter synthesis by the circuit synthesis approach with frequency dependent inverters in bandpass domain is indeed desired.

In Fig. 3.1, the circuit elements include *LC* resonators and frequency dependent coupling inverters:

-- The *LC* resonator consists of a capacitor and an inductor in parallel. The number of the resonators in the filter circuit model determines the degree of the filter. The *LC* resonator, instead of a frequency invariant reactance in shunt with a capacitor enables the filtering characteristic function to be solved directly in bandpass domain. During the extraction process, there are several cases to be handled:

- *LC* resonator in front of a composite type coupling inverter
- *LC* resonator in front of an inductive coupling inverter
- *LC* resonator in front of a capacitive coupling inverter

-- Frequency dependent coupling inverters, acting as coupling elements among the resonators. The couplings between two resonators in sequence are named mainline couplings. Those between non-sequential resonators are cross-couplings. And the frequency dependent coupling inverter can represent the filter response over a wide frequency range. Once again, the coupling inverters can be inductive, capacitive or a composite of both. During the extraction process, there

are several cases to be handled as well:

- Composite coupling inverter as a mainline coupling
- Inductive coupling inverter as a mainline coupling
- Capacitive coupling inverter as a mainline coupling
- Inductive coupling inverter as a cross-coupling
- Capacitive coupling inverter as a cross-coupling

The circuit model in Fig. 3.1 is a 6th-degree filter network and will serve as a prototype model. Other degree filter networks with or without cross-couplings will be scaled from this prototype model in a similar fashion. As summarized in [24], there are many excellent contributions to the circuit synthesis approach in the literature. In this Chapter, it is not the intention to repeat, but rather to utilize and expand the established theories to develop a new synthesis technique for wideband microwave filters.

3.2.2 The Derivation of the [*ABCD*] Polynomial Matrix

Although each of the elements of the [*ABCD*] matrix is a rational polynomial, we will call the [*ABCD*] polynomial matrix for short.

In this Section, the [*ABCD*] polynomial matrix will be derived from the [*S*]-parameters in terms of the polynomials *E(s)*, *F(s)* and *P(s)*. To recap several equations

from Chapter Two, consider the transfer and reflection polynomial functions (*S*-parameters) of a two-port lossless, passive and reciprocal *N*-degree filter network:

$$\left|S_{21}(j\omega)\right|^2 = \frac{1}{1+\varepsilon^2\Phi^2(j\omega)} \text{ and } \left|S_{11}(j\omega)\right|^2 = \frac{\varepsilon^2\Phi^2(j\omega)}{1+\varepsilon^2\Phi^2(j\omega)} \quad (3.1)$$

where $\Phi(j\omega)$ is the characteristic filtering function defined by:

$$\Phi(j\omega) = \frac{F(j\omega)}{P(j\omega)} = \frac{\prod_{i=1}^{N}(\omega^2 - p_i^2)}{\omega^p \prod_{j=1}^{M}(\omega^2 - z_j^2)\prod_{i=1}^{L}(\omega^2 + c_i^2)\prod_{i=1}^{K}(\omega^4 + d_i\,\omega^2 + e_i)} \quad (3.2)$$

where p_i, $i = 1, 2, \ldots, N$ are the reflection zeros; z_j, $j = 1, 2, \ldots, M$ are the real frequency transmission zeros; c_i, $i = 1, 2, \ldots, L$ are the imaginary frequency transmission zeros; and $d^2_i - 4e_i < 0$, $i = 1, 2, \ldots, K$ define the complex frequency transmission zeros.

Eq. (3.1) and Eq. (3.2) are the same as Eq. (2.4) and Eq. (2.8), except a new notation $\Phi(j\omega)$ for the characteristic filtering function is used instead of $C(j\omega)$, avoiding the confusion with the *C* element in the [*ABCD*]. In Chapter Two, the solution of the approximation problem in bandpass domain, i.e., the determination of the filtering characteristic function (3.2) has been presented. Note that Eq. (3.2) is directly evaluated in bandpass domain for wideband filter applications.

In order to derive the [*ABCD*] polynomial matrix, the complex frequency variable *s* rather than $j\omega$ will be used, so Eq. (3.1) can now be written as:

$$S_{21}(s)\cdot S_{21}(-s) = \frac{P(s)\cdot P(-s)}{P(s)\cdot P(-s) + \varepsilon^2 F(s)\cdot F(-s)} \quad (3.3a)$$

$$S_{11}(s)\cdot S_{11}(-s)=\frac{\varepsilon^2 F(s)\cdot F(-s)}{P(s)\cdot P(-s)+\varepsilon^2 F(s)\cdot F(-s)} \tag{3.3b}$$

Note that in Eq. (3.3), the polynomial *P(s)* and *F(s)* are monic polynomials with real coefficients. Namely, the leading coefficient of the highest degree of *s* is one for both polynomials.

To analytically determine $S_{11}(s)$ and $S_{21}(s)$ in the polynomial form, the complex zeros of the denominator polynomial in Eq. (3.3), $P(s)\cdot P(-s)+\varepsilon^2 F(s)\cdot F(-s)$ must firstly be obtained. These complex zeros must occur in complex conjugate pairs: $\pm s_i$, $\pm s_i^*$, *i = 1, 2, …, N*. Select the complex zeros with negative real parts, and let these be s_1, s_1^*, s_2, s_2^*, …, s_N, s_N^*. These selected complex zeros will form the real monic Hurwitz polynomial *E(s)*:

$$E(s)=\prod_{i=1}^{N}\left(s-s_i\right)\left(s-s_i^*\right)=\prod_{i=1}^{N}\left(s^2-2\,\mathrm{Re}\left(s_i\right)s+\left|s_i\right|^2\right) \tag{3.4}$$

Then $S_{11}(s)$ and $S_{21}(s)$ can be expressed as:

$$S_{11}(s)=\frac{F(s)}{E(s)} \text{ and } S_{21}(s)=\frac{P(s)/\varepsilon}{E(s)} \tag{3.5}$$

and

$$E(s)=E_e(s)+E_o(s) \tag{3.6}$$

where $E_e(s)$ is the even part and $E_o(s)$ is the odd part of *E(s)*.

The [*ABCD*] polynomial matrix of the lossless two-port network terminated by the source and load impedances R_{01} and R_{02}, respectively can be derived from the *S*-

parameters in terms of the polynomials *E(s)*, *F(s)* and *P(s)* using the following equation [33]-[34]:

$$\begin{bmatrix} A & B \\ C & D \end{bmatrix} = \begin{bmatrix} \sqrt{\frac{R_{01}}{R_{02}}}\frac{(1+S_{11})(1-S_{22})+S_{12}S_{21}}{2S_{21}} & \sqrt{R_{01}R_{02}}\frac{(1+S_{11})(1+S_{22})-S_{12}S_{21}}{2S_{21}} \\ \frac{1}{\sqrt{R_{01}R_{02}}}\frac{(1-S_{11})(1-S_{22})-S_{12}S_{21}}{2S_{21}} & \sqrt{\frac{R_{02}}{R_{01}}}\frac{(1-S_{11})(1+S_{22})+S_{12}S_{21}}{2S_{21}} \end{bmatrix} \tag{3.7}$$

The impedances R_{01} and R_{02} terminating the two ports can be regarded as normalizing impedances for the impedance level of the network. Therefore, both of the impedances can be assumed as 1 (one) Ohm, $R_{01} = R_{02} = 1$. These impedances can later be de-normalized to any impedance value for practical consideration.

For a passive, lossless, reciprocal ($S_{21} = S_{12}$) two-port network, the condition of conservation of energy implies the following as necessary conditions [34]:

$$S_{11}(s)S_{11}(-s) + S_{21}(s)S_{21}(-s) = 1 \tag{3.8a}$$

$$S_{22}(s)S_{22}(-s) + S_{12}(s)S_{12}(-s) = 1 \tag{3.8b}$$

$$S_{11}(s)S_{12}(-s) + S_{21}(s)S_{22}(-s) = 0 \tag{3.8c}$$

This set of equations is also called unitary condition. From Eq. (3.5) and Eq. (3.8), it is easy to have:

$$F(s)\cdot F(-s) + P(s)/\varepsilon \cdot P(-s)/\varepsilon = E(s)\cdot E(-s) \tag{3.9}$$

For $S_{22}(s)$, the fourth and last element in the *S*-parameters of the two-port network, there are two possible solutions:

$$S_{22}(s) = \pm S_{11}(s) \tag{3.10}$$

For the first case, if $S_{11} = S_{22}$, then $F(s)$ is an even polynomial, and $P(s)$ is an odd polynomial, so that

$$F(s) = F(-s)$$

$$P(s)/\varepsilon = -P(-s)/\varepsilon$$

$$E(-s) = E_e(s) - E_o(s) \tag{3.11}$$

Then Eq. (3.9) becomes

$$F^2 - \left(P/\varepsilon\right)^2 = E(s)E(-s) = E_e^2 - E_o^2 \tag{3.12}$$

Now, using (3.5), (3.8) and (3.12), every element of the [*ABCD*] polynomial matrix in (3.7) can be further derived as:

$$A = \sqrt{\frac{R_{01}}{R_{02}}}\frac{\left(1+S_{11}\right)\left(1-S_{22}\right)+S_{12}S_{21}}{2S_{21}}$$

$$= \frac{\left(1+F/E\right)\left(1-F/E\right)+\left(P/\varepsilon/E\right)^2}{2P/\varepsilon/E} = \frac{\left(E+F\right)\left(E-F\right)+\left(P/\varepsilon\right)^2}{2EP/\varepsilon}$$

$$= \frac{E^2 - F^2 + \left(P/\varepsilon\right)^2}{2EP/\varepsilon} = \frac{E^2 - E(s)E(-s)}{2EP/\varepsilon}$$

$$= \frac{E(s)-E(-s)}{2P/\varepsilon} = \frac{E_o}{P/\varepsilon} \tag{3.13}$$

Similarly,

$$B = \sqrt{R_{01}R_{02}}\frac{\left(1+S_{11}\right)\left(1+S_{22}\right)-S_{12}S_{21}}{2S_{21}} = \frac{E_e+F}{P/\varepsilon} \tag{3.14}$$

$$C = \frac{1}{\sqrt{R_{01}R_{02}}} \frac{(1-S_{11})(1-S_{22}) - S_{12}S_{21}}{2S_{21}} = \frac{E_e - F}{P/\varepsilon} \tag{3.15}$$

$$D = \sqrt{\frac{R_{02}}{R_{01}}} \frac{(1-S_{11})(1+S_{22}) + S_{12}S_{21}}{2S_{21}} = \frac{E_o}{P/\varepsilon} \tag{3.16}$$

Overall, the derived [*ABCD*] polynomial matrix in terms of the polynomials *E(s)*, *F(s)* and *P(s)* is

$$\begin{bmatrix} A & B \\ C & D \end{bmatrix} = \frac{1}{P(s)/\varepsilon} \begin{bmatrix} E_o(s) & E_e(s)+F(s) \\ E_e(s)-F(s) & E_o(s) \end{bmatrix} \tag{3.17}$$

As for the second case, if $S_{11} = -S_{22}$, then *P(s)* must be an even polynomial, and Eq. (3.9) now becomes:

$$F^2 + (P/\varepsilon)^2 = E(s)E(-s) \tag{3.18}$$

Following similar derivations, the [*ABCD*] polynomial matrix in (3.7) can now be derived as:

$$\begin{bmatrix} A & B \\ C & D \end{bmatrix} = \frac{1}{P(s)/\varepsilon} \begin{bmatrix} E_e(s)+F(s) & E_o(s) \\ E_o(s) & E_e(s)-F(s) \end{bmatrix} \tag{3.19}$$

Here, the reflection coefficient $S_{11}(s) = F(s)/E(s)$ is re-examined. In the filter's circuit model, the first element looking into the circuit from a terminal port is a parallel *LC* resonator in shunt. As $s \to j\infty$, the parallel *LC* resonator in shunt will short the terminal port, which implies the reflection coefficient at this port is equal to

-1 at $s \to j\infty$.

$$S_{11}(s = j\infty) = -1 \tag{3.20}$$

Therefore,

$$S_{11}(s)\Big|_{s\to j\infty} = \frac{F(s)}{E(s)}\Big|_{s\to j\infty} = \frac{f_{2N}}{e_{2N}} = -1 \tag{3.21}$$

where f_{2N} and e_{2N} are the leading coefficients of the highest order s^{2N} in the polynomial *F(s)* and *E(s)*, respectively. Because *F(s)* and *E(s)* are derived from the multiplication of their singularities, their leading coefficients of s^{2N} will be 1 (recall *F(s)* and *E(s)* are both monic). According to (3.21), it is necessary to manually multiply *F(s)* by -1 so that the derived polynomials can properly represent the proposed structure of the filter circuit model. The polynomial *F(s)* is selected for convenience, instead of selecting *E(s)*. Note that by multiplying *F(s)* by -1, the necessary condition in (3.8) is still preserved.

For convenience, the polynomials *E(s)*, *F(s)* and *P(s)* are still chosen as monic polynomials. Then, it will be necessary to modify Eq. (3.17) as

$$[ABCD] = \frac{1}{P(s)/\varepsilon}\begin{bmatrix} A(s) & B(s) \\ C(s) & D(s) \end{bmatrix} = \frac{1}{P(s)/\varepsilon}\begin{bmatrix} E_o(s) & E_e(s) - F(s) \\ E_e(s) + F(s) & E_o(s) \end{bmatrix} \tag{3.22a}$$

The highest orders of each polynomial are

$$\frac{1}{p+2L}\begin{bmatrix} 2N-1 & 2N-2 \\ 2N & 2N-1 \end{bmatrix} \tag{3.22b}$$

where *N* is the order of filter circuit network, *p* is the coefficient in (3.2) (the order of transmission zeros at dc) and *L* is the number of real frequency transmission zeros

(assumed no other type of transmission zeros, although that is possible).

As seen from the above equation, for a specific element I in the [$ABCD$] matrix (I = A, B, C, or D), the actual element is a rational polynomial of the form $I(s)/P(s)/\varepsilon$. Since all four elements share the same denominator polynomial, sometimes the element I may be simply referred as $I(s)$, or just I.

In the following sections, only filter networks having the property of $S_{11} = S_{22}$ are considered. So the rational polynomials $A(s)$, $B(s)$, $C(s)$ and $D(s)$ will be evaluated from Eq. (3.22). For other cases which are not treated here, Eq. (3.17) and (3.19) may still be considered.

3.2.3 The Cascade Synthesis and the Extraction Procedure

Having formed the overall [$ABCD$] polynomial matrix in the bandpass domain, the next step is to carry out the extraction of every individual circuit element from the overall [$ABCD$] matrix in a pre-defined sequence.

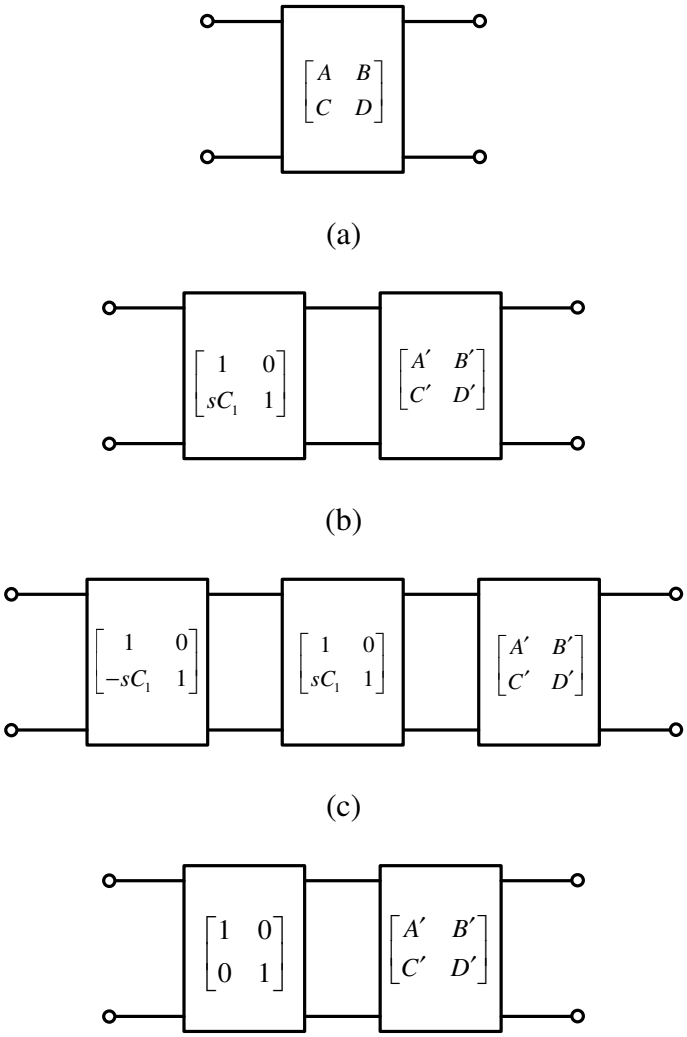

Figure 3.2. Extraction procedures for a circuit element from the [*ABCD*] polynomial matrix.

If it is required to extract a certain element, it is hypothesized that the overall [*ABCD*] polynomial matrix contains such an element. Fig. 3.2 (a) shows the overall [*ABCD*] polynomial matrix as a single two-port network. In Fig. 3.2 (b), a capacitor element is assumed to be the first element in the overall matrix and to be extracted in the first step. The primed [*ABCD*] matrix represents the remaining [*ABCD*]

polynomial matrix after element extraction. Then, this element is extracted by pre-multiplying the overall [*ABCD*] polynomial matrix with the inverse [*ABCD*] matrix of the extracted element as shown in Fig. 3.2 (c), leaving a remainder [*ABCD*] polynomial matrix in cascade with a unit matrix as shown in Fig. 3.2 (d). This unit matrix can be ignored. The whole extraction procedure is the reverse of building up the overall [*ABCD*] polynomial matrix from the individual elements in the entire circuit network. A sequence of successful extractions will result in a remainder [*ABCD*] matrix, all of which elements are either zero or constant at the final step [24].

Knowledge of the type of circuit element and the order in which it appears in the circuit network is required beforehand. For the proposed two-port filter circuit model shown in Fig. 3.1, the extraction procedure will commence with an *LC* resonator from one port, followed by coupling inverters. Next, the extraction procedure will work from the two ports alternatively till a coupling inverter as a cross-coupling is reached and the *LC* resonators at both ends of this cross-coupling inverter have been extracted. After extracting the cross-coupling inverter, the extraction procedure will continue working from the two ports in an iterative manner. The last remainder [*ABCD*] matrix will be a single element, the value of which can be solved directly from the [*ABCD*] matrix.

For an inline topology of a circuit network, it is not necessary to alternate the ports, from which the extraction procedure is performed. The sequence of extraction can start from one port, work through the entire circuit network, and reach the last

element at the other port. Nevertheless, it is still possible to alternate the ports during the extraction procedure for different considerations, such as for the arrangement about the locations of composite type coupling inverters among other coupling inverters. Regardless of the sequence, the extracted circuit network will produce the same frequency responses. The details about these aspects will be covered in the following sections.

3.3 THE CASCADE SYNTHESIS

3.3.1 Overview

A third-order filter is used in this Section as an example to demonstrate the extraction procedure of the cascade synthesis. The circuit model of this filter is shown in Fig. 3.3 with three *LC* resonators and two composite type coupling inverters arranged in an inline topology. The composite type coupling inverter shown in Fig. 2.5 (c) not only provides the direct coupling between two *LC* resonators, but also is responsible to realize a transmission zero. Therefore, the third-order filter with angular center frequency = 8 GHz, bandwidth = 3 GHz and return-loss level -22 dB has two transmission zeros, one located below passband at 4.1364 GHz giving a 30-dB side lobe, and the other located above passband at 13.0881 GHz showing a 25-dB side lobe.

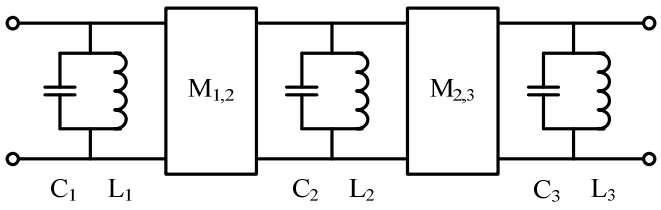

Figure 3.3. Circuit model for a third-order inline filter with two composite type coupling inverters.

The choice of how the transmission zeros are assigned to composite type couplings is arbitrary, and can be regarded as a design factor. This assignment of transmission

zeros to composite type couplings will be of great importance in the physical implementation of *LC* resonators and coupling elements and other practical considerations of the filter design.

As introduced in Sec. 3.2, the extraction of the values of circuit elements commences with the synthesis of the transfer and reflection polynomial functions. Then the transfer and reflection functions are used to obtain the [*ABCD*] polynomial. Every circuit element shown in Fig. 3.3 will be extracted from the [*ABCD*] polynomial matrix in a cascaded sequence. After the extraction of a circuit element, the remaining [*ABCD*] matrix will be used for the extraction of next element. The extraction sequence will be carried out until the last element is left over, which could be an *LC* resonator or a coupling element. The value of the last element can be directly evaluated from the final remainder [*ABCD*] matrix. The successful extraction till the last element also possibly indicates the successfulness of the whole extraction sequence.

3.3.2 The Cascade Synthesis: Step by Step

First, the polynomials *E(s)*, *F(s)* and *P(s)* in (3.5) are evaluated after solving the approximation problem introduced in Section 2.2:

	s^6	*s^5*	*s^4*	*s^3*	*s^2*	*s^1*	*s^0*
E(s)	1	7.5328	220.74	1029.3	13752	29302	2.388e5
F(s)	1	0	193.02	0	11978	0	2.388e5
P(s)	0	1	0	188.41	0	2930.9	0

$$p = 1 \text{ and } \varepsilon = 0.87974 \tag{3.23}$$

Note that the highest degree of s in *E(s)* and *F(s)* is $2N$ (N = 3), since the approximation problem is solved in bandpass domain for wideband filter applications. The coefficient p in the denominator of (3.2) has to be one, since *P(s)* is an odd polynomial constructed by the multiplication of singularities (transmission zeros conjugated pairs), and the order of *P(s)* is less than the order of *F(s)*. Also, the coefficient ε in (3.5) is evaluated to be 0.87974.

An important issue here is that all of the polynomials are numerically evaluated, and the software package MATLAB is used as programming environment. In MATLAB [19], by default, double-precision floating-point format is used, which gives 16 significant decimal digits. This imposes the limitation on handling the high order polynomials, since the rounded numerical error can accumulate very quickly. Filters up to 7th-dgree have been tested and will be demonstrated in the next Chapter. For high order filter, mathematical treatments, such as variable transformation or high-precision computing in MATLAB may be required.

Next, the [*ABCD*] polynomial matrix can be numerically evaluated from the polynomials *E(s)*, *F(s)* and *P(s)* by using Eq. (3.22):

	s^6	*s^5*	*s^4*	*s^3*	*s^2*	*s^1*	*s^0*
A(s)	0	7.5328	0	1029.3	0	29302	0
B(s)	0	0	27.725	0	1774.3	0	0
C(s)	2	0	413.76	0	25729	0	4.777e5
D(s)	0	7.5328	0	1029.3	0	29302	0
P(s)	0	1	0	188.41	0	2930.9	0

(3.24)

This overall [*ABCD*] will serve as the starting point of the extraction sequence.

In the following derivation, the inductance L will be replaced by $H = 1/L$ for easy expression. Since the microwave filters discussed here are usually defined in GHz range in terms of center frequency and bandwidth, if an angular frequency value is defined, a capacitance will carry a unit of *nF* by default. Similarly, for convenience, an inductance will carry a unit of *nH*.

Also note that two known transmission zeros are going to be realized directly by two composite type coupling inverters, respectively.

$$z_1 = \sqrt{\frac{H_{12}}{C_{12}}} = 4.1364 \text{ and } z_2 = \sqrt{\frac{H_{23}}{C_{23}}} = 13.0881 \qquad (3.25)$$

Therefore, either $C_{i,j}$ or $H_{i,j}$ (in $M_{i,j}$), $i = 1, 2, \ldots, N-1$ and $j = i+1$ is known, then the other is also known. The assignment of transmission zeros to composite type coupling inverters is arbitrary and interchangeable. The different assignment will yield different values of circuit elements extracted, but the transfer and reflection response will not change.

As shown in Fig. 3.4 (a), a capacitance $sC_{x,1}$ is first to be extracted from the overall [*ABCD*] by using

$$C_{x,1} = \frac{D(s)}{sB(s)}\Big|_{s=jz_1} = -0.62480 \qquad (3.26)$$

It is important to note that this equation is evaluated at $s = jz_1$, the frequency of the transmission zero realized by the composite coupling $M_{1,2}$ ($C_{1,2}$ & $H_{1,2}$) located

behind the *LC* resonator (C_1 and H_1) in the circuit topology. Then the remainder [*ABCD*] polynomial matrix, [*ABCD*]′ after the extraction will be evaluated, according to the steps in Fig. 3.2 by

$$\begin{bmatrix} 1 & 0 \\ -sC_x & 1 \end{bmatrix}\begin{bmatrix} A & B \\ C & D \end{bmatrix} = \begin{bmatrix} A & B \\ C - sC_xA & D - sC_xB \end{bmatrix} = \begin{bmatrix} A' & B' \\ C' & D' \end{bmatrix} \quad (3.27)$$

In numerical form:

	s^6	*s^5*	*s^4*	*s^3*	*s^2*	*s^1*	*s^0*
A'(s)	0	7.5328	0	1029.3	0	29302	0
B'(s)	0	0	27.725	0	1774.3	0	0
C'(s)	6.7065	0	1056.9	0	44037	0	4.777e5
D'(s)	0	24.856	0	2137.9	0	29302	0
P'(s)	0	1	0	188.41	0	2930.9	0

(3.28)

It is interested to have these relationships:

$$C'(s) = C(s) - sC_{x,1}A(s) = (s^2 + z_1^2)C'_d(s) \quad (3.29a)$$

$$D'(s) = D(s) - sC_{x,1}B(s) = (s^2 + z_1^2)D'_d(s) \quad (3.29b)$$

which are critical in the following extraction steps. The [*ABCD*]′ now becomes:

$$\begin{bmatrix} A' & B' \\ C' & D' \end{bmatrix} = \begin{bmatrix} A & B \\ (s^2 + z_1^2)C'_d & (s^2 + z_1^2)D'_d \end{bmatrix} \quad (3.30)$$

The derivation and proof of (3.26) and (3.29) will be presented later in Section 3.4.3.

In next extraction, the remainder [*ABCD*] polynomial matrix, [*ABCD*]′ in previous step will serve as the *new* overall [*ABCD*]. As shown in Fig. 3.4 (b), a susceptance with the admittance

$$\frac{H_{x,1}}{s}(s^2 + z_1^2) \quad (3.31)$$

is extracted from the $[ABCD]'$ by using

$$H_{x,1} = \left.\frac{sD'(s)}{(s^2 + z_1^2)B'(s)}\right|_{s=jz_1} \Rightarrow H_{x,1} = \frac{sD'_d(s)}{B'(s)}|_{s=jz_1} = 0.99032 \qquad (3.32)$$

Note that this equation is also evaluated at $s = jz_1$, as Eq. (3.26). Then the remainder $[ABCD]$ polynomial matrix, $[ABCD]''$ after the extraction will be evaluated by:

$$\begin{bmatrix} 1 & 0 \\ -\frac{H_x}{s}(s^2 + z_1^2) & 1 \end{bmatrix}\begin{bmatrix} A' & B' \\ C' & D' \end{bmatrix}$$

$$= \begin{bmatrix} A' & B' \\ C' - \frac{H_x}{s}(s^2 + z_1^2)A' & D' - \frac{H_x}{s}(s^2 + z_1^2)B' \end{bmatrix} = \begin{bmatrix} A'' & B'' \\ C'' & D'' \end{bmatrix} \qquad (3.33)$$

In numerical form:

	s^6	*s^5*	*s^4*	*s^3*	*s^2*	*s^1*	*s^0*
A"(s)	0	7.5328	0	1029.3	0	29302	0
B"(s)	0	0	27.725	0	1774.3	0	0
C"(s)	-0.7534	0	-90.115	0	-2422	0	-18833
D"(s)	0	-2.6015	0	-89.023	0	-761.59	0
P"(s)	0	1	0	188.41	0	2930.9	0

(3.34)

Again, similar to Eq. (3.29), the following relationships are expected:

$$C'_d(s) - \frac{H_x}{s}A'(s) = (s^2 + z_1^2)C''_d(s) \qquad (3.35a)$$

$$D'_d(s) - \frac{H_{x,1}}{s}B'(s) = (s^2 + z_1^2)D''_d(s) \qquad (3.35b)$$

And having the following,

$$C''(s) = (s^2 + z_1^2)^2 C''_d(s) \qquad (3.36a)$$

$$D''(s) = (s^2 + z_1^2)^2 D''_d(s) \qquad (3.36b)$$

Now, the $[ABCD]''$ becomes:

$$\begin{bmatrix} A'' & B'' \\ C'' & D'' \end{bmatrix} = \begin{bmatrix} A' & B' \\ (s^2 + z_1^2)^2 C''_d & (s^2 + z_1^2)^2 D''_d \end{bmatrix} \qquad (3.37)$$

The remainder [*ABCD*] polynomial matrix, [*ABCD*]″ in (3.37) is a critical preparation for the next step, extracting the composite type coupling inverter $M_{1,2}$. The orders of any polynomials in the [*ABCD*]′ and [*ABCD*]″ have not been reduced yet. Before proceeding to the next extraction, the two circuit elements extracted from the previous two steps are re-examined, by computing the total admittance extracted from the circuit network so far:

$$sC_x + \frac{H_x}{s}(s^2 + z_1^2) = s(C_x + H_x) + \frac{1}{s}H_x z_1^2 = sC_1 + \frac{1}{s}H_1 \qquad (3.38)$$

This clearly indicates that a capacitance C_1 and an inductance H_1 have been extracted, as depicted in Fig. 3.5.

$$C_1 = C_x + H_x = 0.3655$$

$$H_1 = H_x z_1^2 = 16.9443 \qquad (3.39)$$

Although the circuit elements directly extracted from the [*ABCD*] polynomial matrix are not a capacitance and an inductance in parallel, the extracted elements can still be transformed into a *LC* resonator, which readily yield the first *LC* resonator in the circuit model in Fig. 3.3. This simple transformation will not affect the overall [*ABCD*] polynomial matrix and the filter transfer and reflection functions. Some more derivation and discussion about this claim will also be elaborated in a later Section to give more insight.

In the third extraction, similar iteration is carried out, the remainder [*ABCD*] polynomial matrix, [*ABCD*]″ in (3.37) served as the *new* overall [*ABCD*]. As shown

in Fig. 3.4 (c), a composite type coupling inverter $M_{1,2}$ ($C_{1,2}$ & $H_{1,2}$) is extracted from the $[ABCD]''$. An important difference in extracting a coupling inverter from previous two steps is that it is a design freedom to pick the value of $C_{1,2}$ as one, and the value of $H_{1,2}$ can then be calculated from (3.25). The numerical value of $C_{1,2}$ can determine the admittance level of the entire circuit network [14], and can be scaled or normalized in later stage. Therefore, for a simplicity, $C_{1,2}$ is assumed to be one in this step:

$$C_{1,2} = 1 \text{ and } H_{1,2} = 17.110 \tag{3.40}$$

Then the remainder $[ABCD]$ polynomial matrix, $[ABCD]'''$ after the extraction will be evaluated by:

$$\begin{bmatrix} 1 & \frac{-1}{sC_{12}+\frac{H_{12}}{s}} \\ sC_{12}+\frac{H_{12}}{s} & 1 \end{bmatrix} \begin{bmatrix} A'' & B'' \\ C'' & D'' \end{bmatrix} = \begin{bmatrix} \frac{-C''}{\frac{C_{12}}{s}\left(s^2+\frac{H_{12}}{C_{12}}\right)} & \frac{-D''}{\frac{C_{12}}{s}\left(s^2+\frac{H_{12}}{C_{12}}\right)} \\ \frac{C_{12}}{s}\left(s^2+\frac{H_{12}}{C_{12}}\right)A'' & \frac{C_{12}}{s}\left(s^2+\frac{H_{12}}{C_{12}}\right)B'' \end{bmatrix}$$

$$= \left(s^2+\frac{H_{12}}{C_{12}}\right)\begin{bmatrix} -\frac{s}{C_{12}}C_d'' & -\frac{s}{C_{12}}D_d'' \\ \frac{C_{12}}{s}A'' & \frac{C_{12}}{s}B'' \end{bmatrix} = \begin{bmatrix} A''' & B''' \\ C''' & D''' \end{bmatrix} \tag{3.41}$$

From (3.29a) and (3.36a), the degree of C''_d is 2-degree less than C'_d and 4-degree less than $C(s)$. Similarly, from (3.29b) and (3.36b), the degree of D''_d is 2-degree less than D'_d and 4-degree less than $D(s)$. Also, recall the polynomial $P(s)$ is constructed by the multiplication of transmission zeros conjugated pairs in (3.2), so that

$$\frac{1}{P'''(s)} = \frac{(s^2 + H_{12}/C_{12})}{P''(s)} = \frac{(s^2 + z_1^2)}{P(s)} \tag{3.42}$$

Therefore, the polynomial $P'''(s)$ will contain all of transmission zeros, except z_1 as its singularities. Moreover, the degree of $P'''(s)$ will also be reduced by 2. The

$[ABCD]'''$ can be numerically evaluated as:

	s^6	*s^5*	*s^4*	*s^3*	*s^2*	*s^1*	*s^0*
A'''(s)	0	0	0	0.75342	0	64.333	0
B'''(s)	0	0	0	0	2.6015	0	0
C'''(s)	0	0	7.5328	0	1029.3	0	29302
D'''(s)	0	0	0	27.725	0	1774.3	0
P'''(s)	0	0	0	1	0	171.3	0

(3.43)

The degree of all polynomials has been reduced by 2, which indicates a successful extraction of a *LC* resonator *and* a coupling inverter. The degree reduction on $P'''(s)$ also indicates a successful realization of a transmission zero by the extracted composite type coupling inverter. The order of the remaining filter circuit model is also reduced by 1 to *N*-1 (*p*=1, *L*=2 and *N*=3).

$$\frac{1}{3}\begin{bmatrix} 3 & 2 \\ 4 & 3 \end{bmatrix} \Leftrightarrow \frac{1}{p+2L-2}\begin{bmatrix} 2N-3 & 2N-4 \\ 2N-2 & 2N-3 \end{bmatrix} \tag{3.44}$$

In the following extractions, the previous three steps are essentially repeated to extract the next *LC* resonator and coupling inverter for an inline structure. And the extraction procedure will go on till all circuit elements are extracted. The entire circuit model can then be built up.

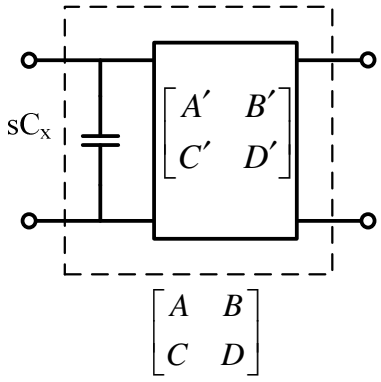

(a)

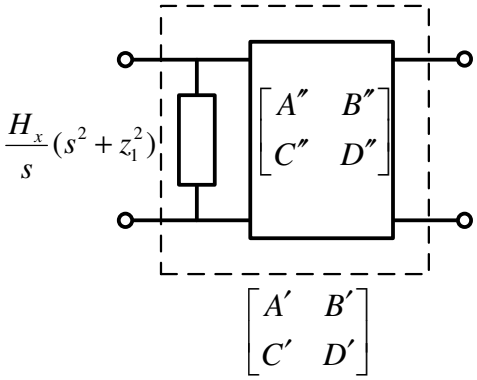

(b)

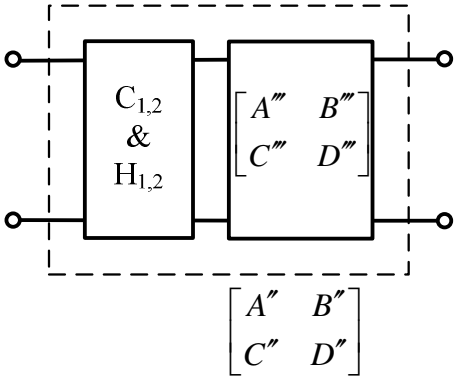

(c)

Figure 3.4. The extraction steps on the first *LC* resonator and the first composite type coupling inverter.

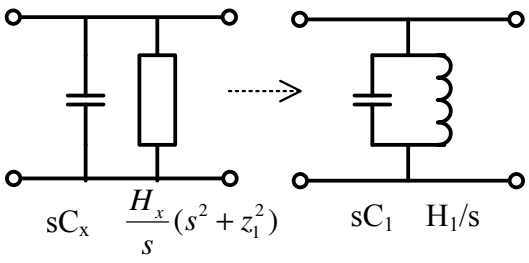

Figure 3.5. The equivalent transform of the first *LC* resonator.

For the second resonator, C_2 and H_2 will be extracted through $C_{x,2}$ and $H_{x,2}$ by using (3.26) and (3.32). First, apply (3.26) to the remainder [*ABCD*] from previous step,

$$C_{x,2} = \left.\frac{D(s)}{sB(s)}\right|_{s=jz_2} \Rightarrow C_{x,2} = 6.6759 \tag{3.45}$$

It is important to note that, in this extraction, the above equation is evaluated at $s = jz_2$, the frequency of the transmission zero realized by the composite coupling $M_{2,3}$ ($C_{2,3}$ & $H_{2,3}$) located behind the *LC* resonator (C_2 and H_2) in the circuit topology. Then the remainder [*ABCD*] polynomial matrix, [*ABCD*]′ after the extraction will be evaluated by (3.30) in a similar manner, and numerically as:

	s^6	*s^5*	*s^4*	*s^3*	*s^2*	*s^1*	*s^0*
A'(s)	0	0	0	0.75342	0	64.333	0
B'(s)	0	0	0	0	2.6015	0	0
C'(s)	0	0	2.5030	0	599.82	0	29302
D'(s)	0	0	0	10.358	0	1774.3	0
P'(s)	0	0	0	1	0	171.3	0

(3.46)

The symbols on some [*ABCD*] polynomial matrix are re-used to show the similarities on the extraction procedure without causing much confusion.

Apply (3.32) to the [*ABCD*]′ in (3.46),

$$H_{x,2} = \left.\frac{sD'(s)}{(s^2 + z_2^2)B'(s)}\right|_{s=jz_{21}} \Rightarrow H_{x,2} = 3.9814 \qquad (3.47)$$

Note that this equation is also evaluated at $s = jz_2$, as Eq. (3.45). Then the remainder [*ABCD*] polynomial matrix, [*ABCD*]″ after the extraction will be evaluated by (3.37) in a similar manner, and numerically as:

	s^6	*s^5*	*s^4*	*s^3*	*s^2*	*s^1*	*s^0*
A"(s)	0	0	0	0.75342	0	64.333	0
B"(s)	0	0	0	0	2.6015	0	0
C"(s)	0	0	-0.4967	0	-170.16	0	-14574
D"(s)	0	0	0	0	0	0	0
P"(s)	0	0	0	1	0	171.3	0

(3.48)

Apply (3.38), and use similar concept as depicted in Fig. 3.5,

$$C_2 = C_{x,2} + H_{x,2} = 10.657$$

$$H_2 = H_{x,2} z_2^2 = 682.01 \qquad (3.49)$$

After the second resonator, C_2 and H_2, the second composite coupling $M_{2,3}$ will be dealt with. Since this coupling inverter is the last one in the entire circuit network, the value of $C_{2,3}$ can no longer be assumed to be one [35].

As suggested in (3.41), $C_{2,3}$ needs to be properly chosen to *normalize* the remainder [ABCD] polynomial matrix, [*ABCD*]‴, so that after extracting composite coupling $M_{2,3}$, the [*ABCD*]‴ is readily shown as the last *LC* resonator. Therefore, the value of $C_{2,3}$ can be evaluated by

$$C_{2,3} = \sqrt{-\frac{c_4}{b_2}} = \sqrt{-\frac{-0.4967}{2.6015}} = 0.43694 \tag{3.50}$$

where c_4 and b_2 are the leading coefficient of the polynomials *C"(s)* and *B"(s)*, respectively as shown in (3.48). The value of $C_{2,3}$, in theory, can also be evaluated from the leading coefficient of the polynomials *D"(s)* and *A"(s)*, but as shown in (3.48), the *D"(s)* has been reduced to zero. The value of $H_{2,3}$ can then be calculated from (3.25),

$$H_{2,3} = 74.846 \tag{3.51}$$

Then the remainder [*ABCD*] polynomial matrix, $[ABCD]'''$ after the extraction will be evaluated by (3.41) in a similar manner, and numerically as

	s^6	*s^5*	*s^4*	*s^3*	*s^2*	*s^1*	*s^0*
A'''(s)	0	0	0	0	0	1.1367	0
B'''(s)	0	0	0	0	0	0	0
C'''(s)	0	0	0	0	0.32920	0	28.109
D'''(s)	0	0	0	0	0	1.1367	0
P'''(s)	0	0	0	0	0	1	0

(3.52)

The degree reduction in (3.52) shows the same pattern as been done in (3.43), which indicated a successful extraction of a *LC* resonator *and* a coupling inverter as well as a successful realization of a transmission zero by the extracted composite type coupling inverter.

Recall the constant $\varepsilon = 0.87974$ in (3.23), so actually the $[ABCD]'''$ in (3.52) is

$$[ABCD] = \begin{bmatrix} 1 & 0 \\ 0.28961s + 24.729/s & 1 \end{bmatrix} \tag{3.53}$$

which clearly shows that the last element in network is a parallel *LC* resonator in shunt. Then C_3 and H_3 can be directly picked out from above [*ABCD*],

$$C_3 = 0.28961 \text{ and } H_3 = 24.729 \tag{3.54}$$

Having finished all of the above extraction steps, all circuit elements shown in Fig. 3.3 have been extracted from the overall [*ABCD*] polynomial matrix representing the filtering characteristic function. The filter responses evaluated from extracted circuit elements are shown in Fig. 3.6 superimposed with the filter responses directly evaluated from the transfer and reflection polynomial functions. The identical responses prove the validation of the extraction procedure and the extracted values of circuit elements.

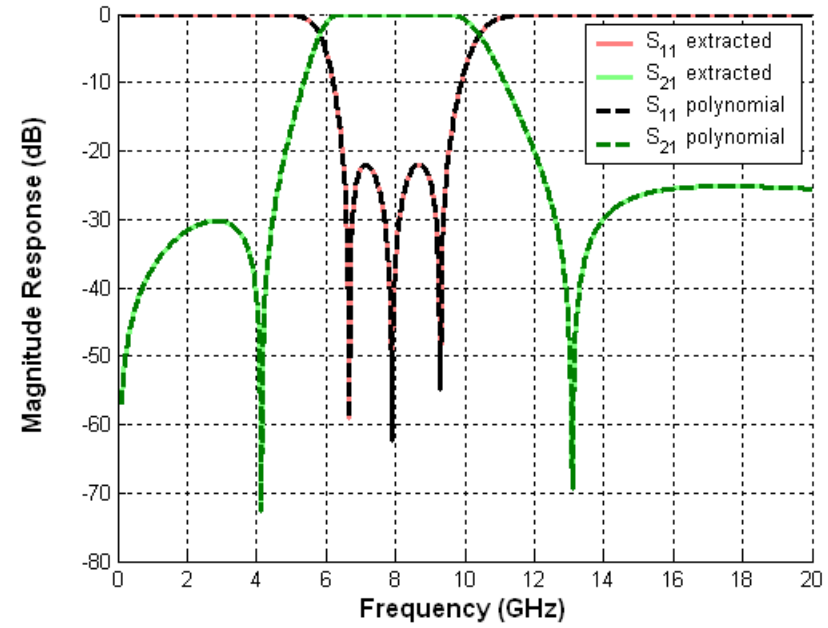

Figure 3.6. Filter responses evaluated from the extracted results and from the characteristic polynomials.

3.4 COMPOSITE TYPE COUPLING INVERTER

3.4.1 Frequency Dependent Coupling Inverter

An ideal impedance inverter is a frequency independent two-port network. If one port of the impedance inverter is terminated by an impedance Z_2, the impedance Z_1 looking into the other port is

$$Z_1 = \frac{K^2}{Z_2} \tag{3.55}$$

where K is a real constant defined as the characteristic impedance of the impedance inverter. The [$ABCD$] matrix of the ideal impedance inverter can be expressed as

$$\begin{bmatrix} A & B \\ C & D \end{bmatrix} = \begin{bmatrix} 0 & \pm jK \\ \mp \dfrac{1}{jK} & 0 \end{bmatrix} \tag{3.56}$$

Similarly, an ideal admittance inverter is a frequency independent two-port network. If one port of the admittance inverter is terminated by an admittance Y_2, the admittance Y_1 looking into the other port is

$$Y_1 = \frac{J^2}{Y_2} \tag{3.57}$$

where J is a real constant defined as the characteristic admittance of the admittance inverter. The [$ABCD$] matrix of the ideal admittance inverter can be expressed as

$$\begin{bmatrix} A & B \\ C & D \end{bmatrix} = \begin{bmatrix} 0 & \pm \dfrac{1}{jJ} \\ \mp jJ & 0 \end{bmatrix} \tag{3.58}$$

A simple approximate practical realization of impedance and admittance inverters is a quarter wavelength of transmission line transformer, having the characteristic impedance or admittance equal to the characteristic impedance or admittance of the inverter, respectively. Such a realization is very common, but can only be applied to a narrow frequency range, since the transmission line can match the ideal impedance and admittance inversion only at single frequency, which limits the application of such realizations to narrow-band filters [36].

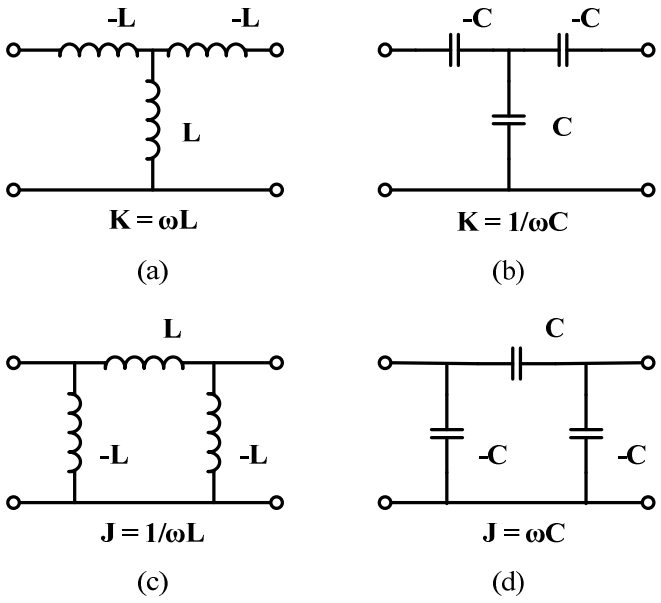

Figure 3.7. Lumped element impedance and admittance inverter.

Lumped element circuits that act as impedance and admittance inverters are shown in Fig. 3.7 along with their equivalent characteristic impedance or admittance [37]. These circuits involve negative values of lumped elements and are frequency dependent. However, the negative elements may be absorbed into the circuit elements

of the adjacent resonant circuits to eliminate them from the overall network. The resultant filter network may consist of *LC* resonators coupled by frequency dependent inverters.

To apply these frequency dependent inverters to practical narrow-band filter design, the values of the inverters (impedance or admittance) at the filter center frequency is chosen to be equal to the values of the mutual couplings between the resonators of the filter network.

Therefore, to model the filtering response over a wide frequency range, the admittance coupling inverters as shown in Fig. 3.7 (c) and (d) are used to couple the shunt *LC* resonators in an equivalent lumped-element circuit model. The type of these frequency dependent admittance coupling inverters can be purely inductive, purely capacitive, or a composite of both as shown in Fig. 2.5 and Fig. 3.8. The impedance coupling inverters as shown in Fig. 3.7 (a) and (b) can be also used in conjunction with the series *LC* resonator. Since these two types of circuit models are inter-changeable due to the dual network theorem, only the former one is thoroughly studied and discussed here.

The [*ABCD*] matrices of three types of frequency dependent admittance coupling inverters, purely inductive, purely capacitive, and a composite of both, can be expressed as the following, respectively:

$$\begin{bmatrix} A & B \\ C & D \end{bmatrix} = \begin{bmatrix} 0 & \pm sL \\ \mp \dfrac{1}{sL} & 0 \end{bmatrix} \tag{3.59}$$

$$\begin{bmatrix} A & B \\ C & D \end{bmatrix} = \begin{bmatrix} 0 & \pm \dfrac{1}{sC} \\ \mp sC & 0 \end{bmatrix} \tag{3.60}$$

$$\begin{bmatrix} A & B \\ C & D \end{bmatrix} = \begin{bmatrix} 0 & \dfrac{1}{sC + \dfrac{1}{sL}} \\ -(sC + \dfrac{1}{sL}) & 0 \end{bmatrix} \tag{3.61}$$

where $s = j\omega$ and ω is the frequency variable.

3.4.2 Analysis of Composite Type Frequency Dependent Coupling Inverter

As shown in Fig. 3.8, two parallel *LC* resonators in shunt are coupled by a composite type coupling inverter, which is represented by two *PI* networks in parallel, one each for inductive coupling (magnetic field) and capacitive coupling (electric field).

This equivalent circuit model is symmetrical, having two identical *LC* resonators. The symmetry plane *T-T'* shown in Fig. 3.9 separates the circuit into two identical halves. Then a perfect electric wall (PEW) or a perfect magnetic wall (PMW) can replace the symmetry plane *T-T'* to analyze the coupling coefficient of the composite coupling inverter [38].

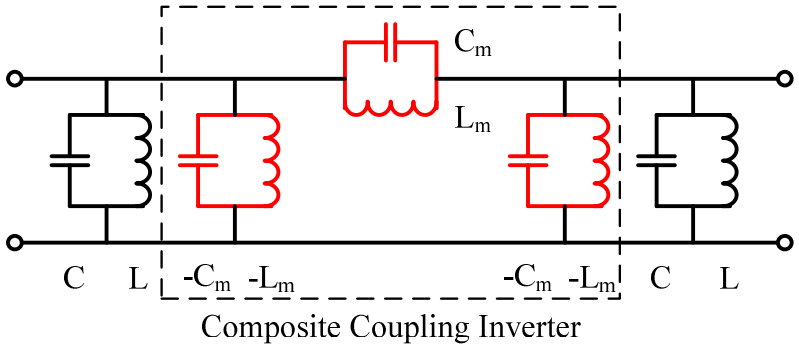

Figure 3.8. Equivalent circuit model of a second-order filter with a composite type coupling inverter.

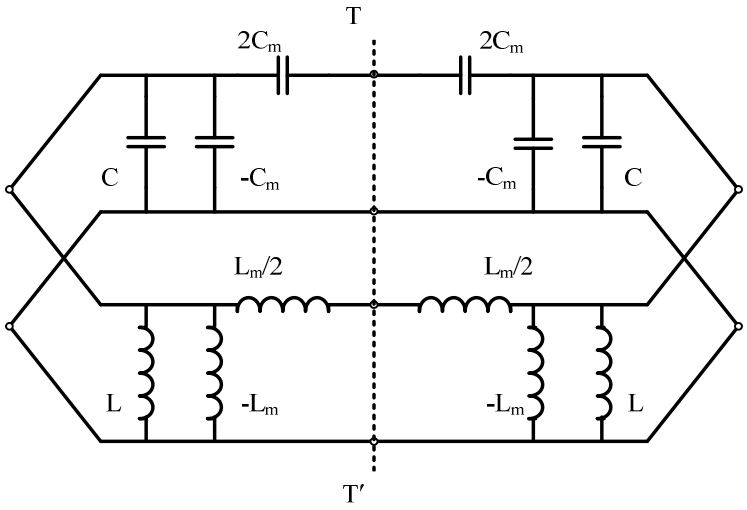

Figure 3.9. Equivalent circuit model with a composite type coupling inverter with a symmetric plane.

If the symmetry plane *T-T'* is replaced by a perfect electric wall, the natural resonant frequency of the resultant circuit can be derived as

$$f_e = \frac{1}{2\pi\sqrt{(C + C_m)\dfrac{LL_m}{L_m + L}}} \tag{3.62}$$

If the symmetry plane *T-T'* is replaced by a perfect magnetic wall, the natural resonant frequency of the resultant circuit can be found as

$$f_m = \frac{1}{2\pi\sqrt{(C - C_m)\dfrac{LL_m}{L_m - L}}} \tag{3.63}$$

The coupling coefficient k_B of a composite type coupling inverter between two identical resonators can be evaluated as

$$k_B = \frac{f_e^2 - f_m^2}{f_e^2 + f_m^2} = \frac{k_M - k_E}{1 - k_M k_E} \tag{3.64}$$

where

$$k_M = \frac{L}{L_m} = \frac{H_m}{H} \text{ and } k_E = \frac{C_m}{C} \tag{3.65}$$

are the coupling coefficients for inductive coupling and capacitive coupling, respectively. Note that (3.64) and (3.65) are different from those given in [36] due to different definition of the equivalent circuit model. In Fig. 3.9, both *LC* resonators are arranged in parallel in the circuit network, and the composite coupling inverter is decomposed by two *PI* networks. This definition is particularly suitable for the microwave filters realized by the combline-like structures presented in the following Sections as design examples.

Eq. (3.64) indicates that, if the coupling coefficients k_M and k_E have the same sign (both are positive by their definition) the absolute value of the coupling coefficient k_B of a composite type coupling is less than the value of k_M or k_E. This is well understood by the interaction of electric and magnetic fields within a physical coupling structure

[39].

A composite type coupling has a shunt *LC* resonator in series in the circuit and should be resonating somewhere in the frequency domain. Therefore if the intrinsic resonance of a composite type coupling is properly selected and carefully designed, it can provide coupling between resonators, and realize a transmission zero close to the filter passband. This transmission zero can be at either the upper side or the lower side of the filter passband without introducing an additional coupling path or other complicated transmission zero generation mechanism.

The inductive coupling k_M is produced by the interaction between magnetic field components in a physical structure. By proper arrangement of the resonators and coupling structures, the magnetic field components responsible for k_M can be in the same direction (in phase) or in the opposite direction (out of phase), resulting in positive or negative signs of k_M, respectively [40].

It is interesting to observe that in (3.64), if the inductive coupling k_M is negative, the absolute value of the coupling coefficient k_B of a composite type coupling is greater than the absolute value of k_M or k_E (the influence of the denominator in (3.64) is omitted for a moment, since usually the product of k_M and k_E is much smaller than 1). Therefore, if a negative inductive coupling and a positive capacitive coupling exist simultaneously in a coupling structure, the *net* total coupling is increased, and the filter bandwidth can be possibly enhanced as well. This is a very useful factor in

designing a wideband microwave filter, since seeking a coupling structure with large coupling is always one of the most challenging tasks in achieving very wide filter bandwidth.

3.4.3 Proof of the Equations Used to Extract Composite Coupling Inverter

As outlined in Sec. 3.3, a third-order filter is given as an example to demonstrate the extraction procedure and some equations used to extract the values of circuit elements. Two key equations (3.26) and (3.32) to extract C_x and H_x are derived in this Section.

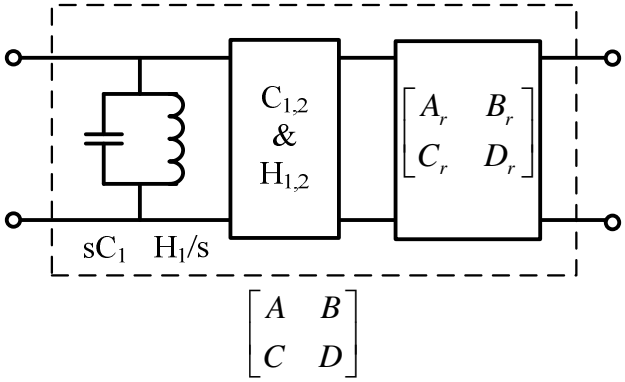

Figure 3.10. The overall [*ABCD*] and the remainder [*ABCD*] after extracting a *LC* resonator and a composite coupling.

Fig. 3.10 shows the overall [*ABCD*] of a filter equivalent circuit model and the remainder [*ABCD*] after extracting an *LC* resonator and a composite coupling. Since the extraction procedure is an iteration process, the order of the filter circuit network

and the number of transmission zeros will both be reduced by one after extracting a *LC* resonator in front of a composite coupling and a composite coupling as a mainline coupling. It is sufficient to study this scenario and derive the extraction equations, since the subsequent steps will be repeated.

According to Fig. 3.10, there is

$$\begin{bmatrix} 1 & 0 \\ sC_1+\dfrac{H_1}{s} & 1 \end{bmatrix} \begin{bmatrix} 0 & \dfrac{1}{sC_{12}+\dfrac{H_{12}}{s}} \\ -\left(sC_{12}+\dfrac{H_{12}}{s}\right) & 0 \end{bmatrix} \begin{bmatrix} A_r & B_r \\ C_r & D_r \end{bmatrix} = \begin{bmatrix} A & B \\ C & D \end{bmatrix} \quad (3.66)$$

where the $[ABCD]_r$ is the remainder $[ABCD]$ after extraction, which can be solved as

$$A_r(s) = \frac{\left(sC_1+\frac{H_1}{s}\right)A(s)-C(s)}{sC_{12}+\frac{H_{12}}{s}} \quad (3.67a)$$

$$B_r(s) = \frac{\left(sC_1+\frac{H_1}{s}\right)B(s)-D(s)}{sC_{12}+\frac{H_{12}}{s}} \quad (3.67b)$$

$$C_r(s) = \left(sC_{12}+\frac{H_{12}}{s}\right)A(s) \quad (3.67c)$$

$$D_r(s) = \left(sC_{12}+\frac{H_{12}}{s}\right)B(s) \quad (3.67d)$$

First, $B_r(s)$ in (3.67b) can be re-written as the following:

$$B_r(s) = \frac{-\frac{s}{C_{12}}}{s^2+\frac{H_{12}}{C_{12}}}\left[D(s)-s\left(C_1-\frac{H_1}{z_1^2}\right)B(s)-\frac{1}{s}\frac{H_1}{z_1^2}\left(s^2+z_1^2\right)B(s)\right] \quad (3.68)$$

Let

$$C_x = C_1 - \frac{H_1}{z_1^2} \tag{3.69}$$

It is argued to find C_x, so that the following equation is valid:

$$D(s) - s\left(C_1 - \frac{H_1}{z_1^2}\right)B(s) = (s^2 + z_1^2)D_d'(s) \tag{3.70}$$

The left hand side of (3.70) is a part of equation in (3.68). This argument can be achieved by using:

$$C_x = \left.\frac{D(s)}{sB(s)}\right|_{s=jz_1} \tag{3.71}$$

which is exact one in (3.26). Substitute (3.70) back into (3.68),

$$B_r(s) = \frac{-\frac{s}{C_{12}}}{s^2 + \frac{H_{12}}{C_{12}}}(s^2 + z_1^2)\left[D_d'(s) - \frac{1}{s}\frac{H_1}{z_1^2}B(s)\right] \tag{3.72}$$

Similar procedures can be applied to $A_r(s)$ (3.67a):

$$A_r(s) = \frac{-\frac{s}{C_{12}}}{s^2 + \frac{H_{12}}{C_{12}}}\left[C(s) - s\left(C_1 - \frac{H_1}{z_1^2}\right)A(s) - \frac{1}{s}\frac{H_1}{z_1^2}\left(s^2 + z_1^2\right)A(s)\right] \tag{3.73}$$

Let

$$C_x = C_1 - \frac{H_1}{z_1^2} \tag{3.74}$$

To find C_x, so that,

$$C(s) - s\left(C_1 - \frac{H_1}{z_1^2}\right)A(s) = (s^2 + z_1^2)C_d'(s) \tag{3.75}$$

This argument can be achieved by using

$$C_x = \left.\frac{C(s)}{sA(s)}\right|_{s=jz_1} \tag{3.76}$$

Substitute (3.75) back into (3.73),

$$A_r(s) = \frac{-\frac{s}{C_{12}}}{s^2 + \frac{H_{12}}{C_{12}}}(s^2 + z_1^2)\left[C_d'(s) - \frac{1}{s}\frac{H_1}{z_1^2}A(s) \right] \tag{3.77}$$

By checking the unitary condition on the [*ABCD*], $AD - BC = 1$, the C_x found in (3.69) and in (3.74) are identical, and either (3.71) or (3.76) can be used to evaluate the value of C_x in the extraction procedure. Moreover, the conditions of (3.70) and (3.75) are valid simultaneously. This can also be seen on the remainder [*ABCD*], $[ABCD]_r$. The numerator polynomial of the A_rD_r has a common factor $s^2+z_1^2$, which implies that the numerator polynomial of the B_rC_r must have the same common factor, *vice versa*. This suggests that the C_x found in (3.70) and in (3.75) are identical.

Next, re-visit (3.72), and let

$$H_x = \frac{H_1}{z_1^2} \tag{3.78}$$

It is argued to find H_x, so that the following equation is valid:

$$D_d'(s) - \frac{1}{s}\frac{H_1}{z_1^2}B(s) = (s^2 + z_1^2)D_d''(s) \tag{3.79}$$

The left hand side of (3.79) is a part of equation in (3.72). This argument can be achieved by using:

$$H_x = \left.\frac{sD_d'(s)}{B(s)}\right|_{s=jz_1} \tag{3.80}$$

which is exact one in (3.32), since *B'(s) = B(s)*. Substitute (3.79) into (3.72),

$$B_r(s) = \frac{-\frac{s}{C_{12}}}{s^2 + \frac{H_{12}}{C_{12}}}(s^2 + z_1^2)^2 D_d''(s) \tag{3.81}$$

Similar procedures can be applied to (3.77), and let

$$H_x = \frac{H_1}{z_1^2} \tag{3.82}$$

To find H_x, so that,

$$C_d'(s) - \frac{1}{s}\frac{H_1}{z_1^2}A(s) = (s^2 + z_1^2)C_d''(s) \tag{3.83}$$

This argument can be achieved by using:

$$H_x = \left.\frac{sC_d'(s)}{A(s)}\right|_{s=jz_1} \tag{3.84}$$

Substitute (3.83) into (3.77),

$$A_r(s) = \frac{-\frac{s}{C_{12}}}{s^2 + \frac{H_{12}}{C_{12}}}(s^2 + z_1^2)^2 C_d''(s) \tag{3.85}$$

Again, by checking the unitary condition on the [$ABCD$], $AD - BC = 1$, the H_x found in (3.78) and in (3.82) are identical, and either (3.80) or (3.84) can be used to evaluate the value of H_x in the extraction procedure. Moreover, the conditions of (3.79) and (3.83) are valid simultaneously.

From (3.69) and (3.78), it is obvious to have

$$C_1 = C_x + H_x$$

$$H_1 = H_x z_1^2 \tag{3.86}$$

which can validate (3.39) in previous Sec. 3.3.

Using (3.81) and (3.85), the remainder [*ABCD*] polynomial matrix, *[ABCD]$_r$* can be re-written as

$$\begin{bmatrix} A_r & B_r \\ C_r & D_r \end{bmatrix} = (s^2 + \tfrac{H_{12}}{C_{12}}) \begin{bmatrix} -\tfrac{s}{C_{12}} C''_d & -\tfrac{s}{C_{12}} D''_d \\ \tfrac{C_{12}}{s} A & \tfrac{C_{12}}{s} B \end{bmatrix} \tag{3.87}$$

which is identical to (3.41) in previous Sec. 3.3. This once again shows that by properly evaluating the value of C_x and H_x, the degree of the remainder [*ABCD*] can be successfully reduced.

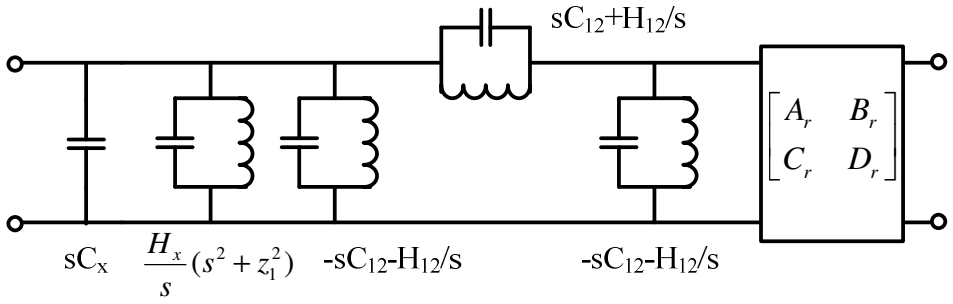

Figure 3.11. Another expression for the circuit model in Fig. 3.10.

Fig. 3.11 shows another expression for the circuit model in Fig. 3.10. When C_x is evaluating as $s = jz_1$, the circuitry immediately behind C_x is open circuit, both in series branch and in shunt branch. Therefore, if looking into the circuit network at the terminal when $s = jz_1$, only C_x is available. After extracting C_x out, the derived equations used to extract H_x is also evaluated as $s = jz_1$. In this case, the circuitry immediately behind H_x is open circuit as well. Therefore, this interpretation on the

circuit network demonstrates another evidence on the derived equations used to extract C_x and H_x.

3.4.4 Examples

To demonstrate the synthesis procedure and give more insight about the composite type coupling inverter, a pair of examples is presented in this section. The filter specifications for two examples are almost identical, namely, second-order 22-db return loss filters with angular center frequency = 3 GHz, and bandwidth = 1 GHz, except that one has a transmission zero at 1.8767 GHz below the filter passband and the other has a transmission zero at 4.1917 GHz above the filter passband.

For the first second-order filter having one transmission zero at dc, namely, $p = 1$ in (3.2), the filtering characteristic function (3.2) is firstly determined, followed by the evaluation of the polynomials *E(s)*, *F(s)*, and *P(s)* in (3.5)

$$\begin{aligned} &E(s): \{1.0000, 4.5747, 21.5470, 27.4213, 71.5009\} \\ &F(s): \{1.0000, 0, 17.3815, 0, 71.5009\} \\ &P(s): \{1.0000, 0, 3.5220, 0\} \\ &\varepsilon = 0.2817 \end{aligned} \tag{3.88}$$

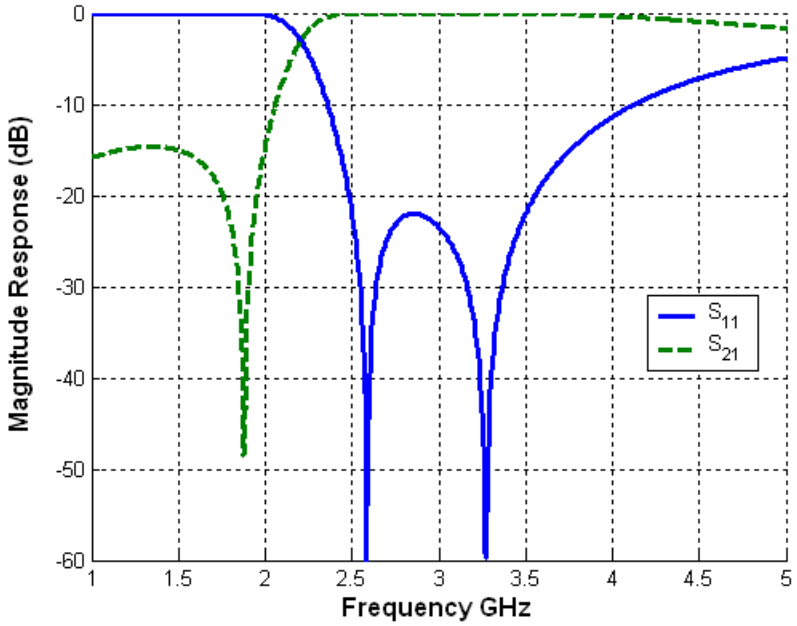

(a)

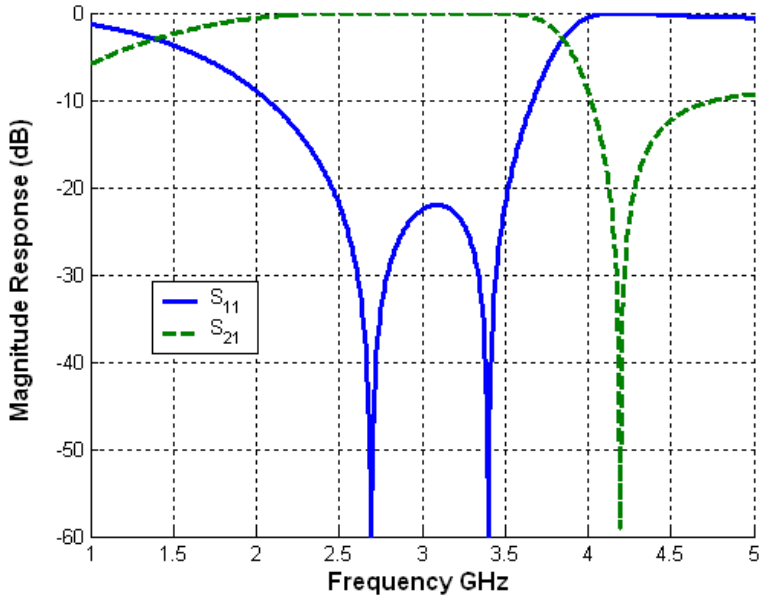

(b)

Figure 3.12. Second-order filter with one transmission zero (a) below filter passband; (b) above filter passband.

The coefficients of the polynomials *E(s)*, *F(s)*, and *P(s)* are shown in the curly brackets with the coefficient of the highest order of *s* at left most and the coefficient of the lowest order s^0 at right most. For this second-order filter ($N = 2$), the highest orders of *s* in both *E(s)* and *F(s)* are four ($2N$). From (3.2), the highest order of *s* in *P(s)* is three. Also, all coefficients are real number.

Then, the [ABCD] polynomial matrix is readily derived from the polynomials *E(s)*, *F(s)* and *P(s)* using (3.22)

$$A(s): \{0, 4.5747, 0, 27.4213, 0\}$$

$$B(s): \{0, 0, 4.1654, 0, 0\}$$

$$C(s): \{2, 0, 38.9285, 0, 143.0019\}$$

$$D(s): \{0, 4.5747, 0, 27.4213, 0\} \qquad (3.89)$$

The coefficients are shown in similar fashion. The degree of each element satisfies those in (3.22b).

Next, using the equivalent circuit model in Fig. 3.8, the values of circuit elements can be extracted from the overall [*ABCD*] polynomial matrix by the equations given in Sec 3.4.4. The extracted values of circuit elements are:

$$C_1 = C_2 = 1.0983,$$

$$L_1 = L_2 = 0.1519,$$

$$C_{1,2} = 0.8521,\ H_{1,2} = 3.0010\ (L_{1,2} = 0.3332). \qquad (3.90)$$

Only the filter responses evaluated from the extracted values of circuit elements are

shown in Fig. 3.12 (a), since they are identical to those evaluated from the polynomials. The coupling coefficient of magnetic coupling, electric coupling, and total coupling can be calculated by using equations (3.64) and (3.65) as the following, respectively.

$$k_M = 0.4559,\ k_E = 0.7758,$$
$$k_B = -0.4951. \tag{3.91}$$

Similar to the first example, the exact analysis and synthesis procedure are carried out to the second one, and the results are listed as the following:

$$E(s)\text{: } \{1.0000,\ 3.5730,\ 22.4480,\ 47.9701,\ 83.7186\}$$
$$F(s)\text{: } \{1.0000,\ 0,\ 18.8005,\ 0,\ 83.7186\}$$
$$P(s)\text{: } \{1.0000,\ 0,\ 17.5774,\ 0\}$$
$$\varepsilon = 0.4275. \tag{3.92}$$

$$A(s)\text{: } \{0,\ 3.5730,\ 0,\ 47.9701,\ 0\}$$
$$B(s)\text{: } \{0,\ 0,\ 3.6476,\ 0,\ 0\}$$
$$C(s)\text{: } \{2,\ 0,\ 41.2485,\ 0,\ 167.4373\}$$
$$D(s)\text{: } \{0,\ 3.5730,\ 0,\ 47.9701,\ 0\} \tag{3.93}$$

$$C_1 = C_2 = 0.9796,$$
$$L_1 = L_2 = 0.0760,$$
$$C_{1,2} = 0.6413,\ H_{1,2} = 11.2718\ (L_{1,2} = 0.0887). \tag{3.94}$$

$$k_M = 0.8571,\ k_E = 0.6546,$$

$$k_B = 0.4612. \tag{3.95}$$

The filter responses evaluated from the extracted values of circuit elements in (3.94) are shown in Fig. 3.12 (b).

It is interesting to observe that the total coupling k_B in (3.91) and (3.95) has a different sign. In first example, the electric coupling is predominant ($k_E > k_M$) so that a transmission zero is generated below the filter passband. The *net* total coupling is a negative number. In second example, the magnetic coupling is predominant ($k_E < k_M$) so that a transmission zero is generated above the filter passband. The *net* total coupling is a positive number. And the absolute value of the total coupling could be smaller than the electric coupling or the magnetic coupling due to the interaction of electric and magnetic fields. Therefore, in order to generate a transmission zero while providing enough coupling between two resonators, a composite type coupling may be required to realize both strong electric coupling and strong magnetic coupling simultaneously. This is an especially critical design consideration and challenge when wideband filter design is concerned.

3.5 INDUCTIVE AND CAPACITIVE COUPLING INVERTER

3.5.1 Overview

In Sec. 3.3.2, the extraction techniques for a *LC* resonator in front of a composite coupling and a composite type coupling inverter as a mainline coupling have been presented in details. As outlined in Sec. 3.2.1, there are other circuit elements in the proposed wideband microwave filter circuit model in Fig. 3.1: inductive and capacitive coupling inverter as a mainline coupling or as a cross coupling, and *LC* resonators in front of these two type coupling inverters. The extraction techniques for these circuit elements will be covered in this section [41].

Inductive and capacitive type coupling inverters can be treated as a special case of a composite type coupling inverter. The equations used to extract them are also regarded as a simplified version of those used to extract composite type coupling inverter.

The synthesis procedure shares the same steps to derive the overall [*ABCD*] polynomial matrix, which are not repeated anymore and are assumed to be known. Moreover, the extraction sequence for the general folded cross-coupled form in Fig. 3.1 will also be referenced.

3.5.2 Extraction Equations

The second-order circuit model in Fig. 3.8 is used again with the composite coupling inverter replaced by purely inductive coupling inverter or purely capacitive coupling inverter in Fig. 3.7 (c) and (d), respectively.

If the frequency-dependent coupling inverter is a purely inductive type, the capacitance C_1 in an *LC* resonator in front of an inductive type inverter can be evaluated using

$$C_1 = \left.\frac{D(s)}{sB(s)}\right|_{s\to j\infty} \quad or \quad \left.\frac{C(s)}{sA(s)}\right|_{s\to j\infty} \tag{3.96}$$

$$\frac{1}{P'(s)/\varepsilon}\begin{bmatrix} A'(s) & B'(s) \\ C'(s) & D'(s) \end{bmatrix} = \frac{1}{P(s)/\varepsilon}\begin{bmatrix} A(s) & B(s) \\ C(s)-sC_1A(s) & D(s)-sC_1B(s) \end{bmatrix} \tag{3.97}$$

Note that the unprimed symbols represent the original overall [*ABCD*] polynomial matrix before extraction and the primed symbols represent the remainder [*ABCD*] polynomial matrix after extraction. At each step, two values for each element are evaluated, one from *A(s)* and *C(s)* polynomials and the other from *B(s)* and *D(s)* polynomials. Basically, they should be of the same value. But in practice, only one set of polynomials should be used to extract the element value. A successful extraction will indicate that the degrees of both *C(s)* and *D(s)* have decreased.

Comparing (3.96) to (3.71) and (3.76), the former is evaluated at $s = j\infty$, while the later at $s = jz_1$, which is the frequency of the transmission zero realized by the

composite coupling. For an inductive coupling inverter, it can be regarded as realizing a transmission zero at infinity, since it is open circuit at infinity frequency. Sharing this similarity, a composite type coupling is used to realize a transmission zero in general, while an inductive coupling inverter is used to realize a transmission zero at infinity.

After the extraction of the capacitance C_1, the inductance L_1 in the same LC resonator can be extracted using

$$L_1 = \left.\frac{B(s)}{sD(s)}\right|_{s\to j\infty} or \left.\frac{A(s)}{sC(s)}\right|_{s\to j\infty} \tag{3.98}$$

$$\frac{1}{P'(s)/\varepsilon}\begin{bmatrix} A'(s) & B'(s) \\ C'(s) & D'(s) \end{bmatrix} = \frac{1}{P(s)/\varepsilon}\begin{bmatrix} A(s) & B(s) \\ C(s)-\dfrac{A(s)}{sL_1} & D(s)-\dfrac{B(s)}{sL_1} \end{bmatrix} \tag{3.99}$$

Comparing (3.98) to (3.80) and (3.84), once again, they are identical, except that the former is evaluated at $s = j\infty$, while the later at $s = jz_1$.

Next, if the frequency-dependent coupling inverter is a purely capacitive type, the inductance L_1 of an LC resonator in front of a capacitive type inverter should be extracted using

$$L_1 = \left.\frac{B(s)}{sD(s)}\right|_{s\to 0} or \left.\frac{A(s)}{sC(s)}\right|_{s\to 0} \tag{3.100}$$

And the capacitance C_1 in the same LC resonator follows

$$C_1 = \left.\frac{D(s)}{sB(s)}\right|_{s\to 0} or \left.\frac{C(s)}{sA(s)}\right|_{s\to 0} \tag{3.101}$$

The equations evaluating the remainder [*ABCD*] polynomial matrix after extracting L_1 and C_1 in this case are identical to those given in (3.99) and (3.97), respectively. But the values of L_1 and C_1 are evaluated as $s = j0$ instead of $s = j\infty$ in (3.96) and (3.98), respectively.

For a capacitive coupling inverter, it can be regarded as realizing a transmission zero at zero, since it is an open circuit at dc. Therefore, the key is that, in order to properly evaluate the circuit element values of *LC* resonator, the type of coupling inverter behind this *LC* resonator must be first determined. And the equations used to extract the value of *LC* resonator will be evaluated at the location of the transmission zero realized by this coupling inverter.

The frequency-dependent coupling inverter $M_{1,2}$ may be treated as either mainline coupling or cross coupling. The extraction of mainline coupling is relatively simple, since mainline coupling may be evaluated as a *unity* inverter. Therefore, the values of circuit elements are equal to one, namely, $L_{1,2} = 1$ or $C_{1,2} = 1$. Regardless of the value of the circuit element, the remainder [*ABCD*] polynomial matrix after extracting a mainline coupling is:

$$\frac{1}{P'(s)/\varepsilon}\begin{bmatrix} A'(s) & B'(s) \\ C'(s) & D'(s) \end{bmatrix} = \frac{1}{P(s)/\varepsilon}\begin{bmatrix} -sL_{1,2}C(s) & -sL_{1,2}D(s) \\ \dfrac{A(s)}{sL_{1,2}} & \dfrac{B(s)}{sL_{1,2}} \end{bmatrix} \qquad (3.102)$$

or

$$\frac{1}{P'(s)/\varepsilon}\begin{bmatrix} A'(s) & B'(s) \\ C'(s) & D'(s) \end{bmatrix} = \frac{1}{P(s)/\varepsilon}\begin{bmatrix} -\dfrac{C(s)}{sC_{1,2}} & -\dfrac{D(s)}{sC_{1,2}} \\ sC_{1,2}A(s) & sC_{1,2}B(s) \end{bmatrix} \tag{3.103}$$

for inductive or capacitive type mainline coupling, respectively.

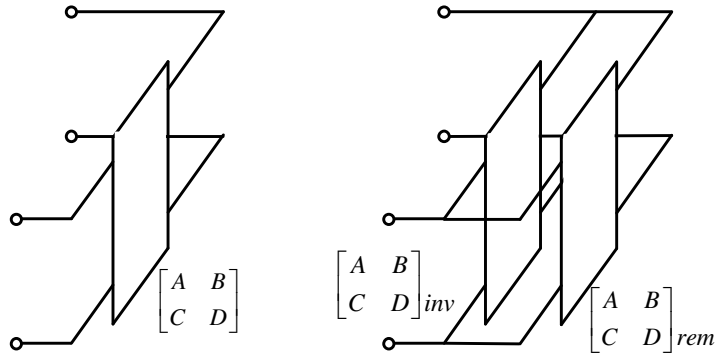

Figure 3.13. Extraction of cross coupling inverter: (a) the overall [*ABCD*]; (b) an inverter represented by $[ABCD]_{\text{inv}}$ in parallel with the remainder $[ABCD]_{\text{rem}}$.

For cross coupling inverter, the overall [*ABCD*] polynomial matrix is first converted to an overall [*Y*] polynomial matrix. The cross coupling inverter is represented by the [*Y*] polynomial matrix, $[Y]_{inv}$. The remainder [*Y*] polynomial matrix, $[Y]_{rem}$ of the circuit network after the cross coupling inverter is extracted, and then converted back to the remainder [*ABCD*] polynomial matrix. This step is illustrated in Fig. 3.13 [24]. For inductive type cross coupling, the value of circuit element is extracted as

$$L_1 = \left.\frac{B(s)}{sP(s)/\varepsilon}\right|_{s\to j\infty} \tag{3.104}$$

$$\frac{1}{P'(s)/\varepsilon}\begin{bmatrix} A'(s) & B'(s) \\ C'(s) & D'(s) \end{bmatrix} = \frac{1}{P(s)/\varepsilon - \dfrac{B(s)}{sL_1}}\begin{bmatrix} A(s) & B(s) \\ C(s) + 2\dfrac{P(s)/\varepsilon}{sL_1} - \dfrac{B(s)}{s^2L_1^2} & D(s) \end{bmatrix}$$

(3.105)

For capacitive type cross-coupling, the value of a circuit element is extracted as

$$C_1 = \left.\frac{P(s)/\varepsilon}{sB(s)}\right|_{s\to 0} \tag{3.106}$$

$$\frac{1}{P'(s)/\varepsilon}\begin{bmatrix} A'(s) & B'(s) \\ C'(s) & D'(s) \end{bmatrix} = \frac{1}{P(s)/\varepsilon - B(s)sC_1}\begin{bmatrix} A(s) & B(s) \\ C(s) + 2P(s)/\varepsilon sC_1 - B(s)s^2C_1^2 & D(s) \end{bmatrix}$$

(3.107)

When finite transmission zeros are present, the degree of $P(s) > 0$, it is essential to extract cross coupling inverter in order to decrease the order of $P(s)$. Moreover, the rules to be observed when extracting a folded prototype network can refer to the summary in [24], except those exclusively stated hereby.

3.5.3 Examples

Two synthesis examples are presented in this section to demonstrate the extraction procedure. The first example is a sixth-degree 22-dB return loss filter with angular center frequency = 6 GHz and bandwidth = 4 GHz. It is known that the maximum number of transmission zeros that can be realized in a folded network is no more than N-2, if the couplings between source and load nodes or between source/load and any

inner resonator are not presented [42]. Therefore, four transmission zeros are implemented above the passband of this filter to generate an equi-ripple level at the upper stopband. Therefore, all possible cross couplings as shown in Fig. 3.1 will be presented.

Following the synthesis procedure introduced, the overall [*ABCD*] polynomial matrix for this filter is derived through the coefficients of the transfer and reflection polynomials functions. And the transmission zero at dc is chosen as one for this example.

Fig. 3.14 (a) shows the topology and coupling diagram of this filter. All mainline couplings and cross couplings are extracted as inductive type coupling inverters, denoted by *L*.

Using the extraction equations given in this Section, all of the circuit elements shown in Fig. 3.14 (a) should be successfully extracted. As mentioned, the extraction procedure should be following a specific sequence for the folded network:

> 1) C_1 and L_1 for the first *LC* resonator, 2) turn network, 3) C_6 and L_6 for the sixth *LC* resonator, 4) cross coupling M_{16}, 5) mainline coupling M_{56}, 6) C_5 and L_5, 7) cross coupling M_{15}, 8) turn network, 9) mainline coupling M_{12}, 10) C_2 and L_2, 11) cross coupling M_{25}, 12) turn network, 13) mainline coupling M_{45}, 14) C_4 and L_4, 15) cross coupling M_{24}, 16) turn network, 17) mainline coupling M_{23}, 18) C_3 and L_3, 19) coupling M_{34}.

The extraction works on the two terminals of the circuit network alternatively. The resonator node is first extracted. The mainline coupling is usually extracted as a *unity* inverter. And the cross coupling can only be extracted after the two resonator nodes of this coupling have been extracted. A coupling cannot be extracted unless any other couplings in front of it have been extracted.

The extraction procedure usually commences from one terminal for the first *LC* resonator. The procedure of turn network means to change the working terminal to the other one for a two-port network. In the [*ABCD*] matrix, it is simply to inter-change the element *A* and *D* [8]. At the end of extraction procedure, the polynomials *P(s)*, *A(s)*, *B(s)*, *C(s)* and *D(s)* are either zero or constant (constant for the evaluation of the circuit element value of last inverter $M_{3,4}$).

For this example, the extracted values of circuit elements are C_i = [0.2259, 0.0095, 0.5328, 1.1964, 0.0095, 0.2259], L_i = [0.1036, 2.4948, 0.0409, 0.0140, 2.4603, 0.1036], $L_{12} = L_{23} = L_{45} = L_{56} = 1$, $L_{34} = 0.2009$, $L_{16} = 47.8427$, $L_{15} = 18.9739$, $L_{25} = 23.5012$, and $L_{24} = 1.4375$. One may find that it is more meaningful to represent the extracted values of circuit elements after normalization in doing physical implementation using (2.128). As mentioned before, the last inverter can no longer be assumed to be 1 in order to maintain the admittance level of the entire circuit model. So the L_{34}, the last mainline coupling inverter for this case is evaluated, while other mainline couplings are 1.

The filter responses obtained from polynomials and those obtained from the extracted circuit elements are shown in Fig. 3.14 (b). The exact match between these responses validates the extraction procedure.

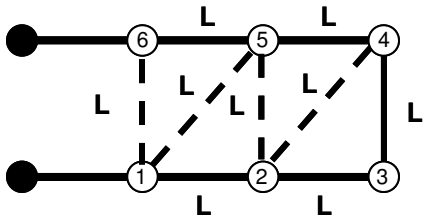

(a)

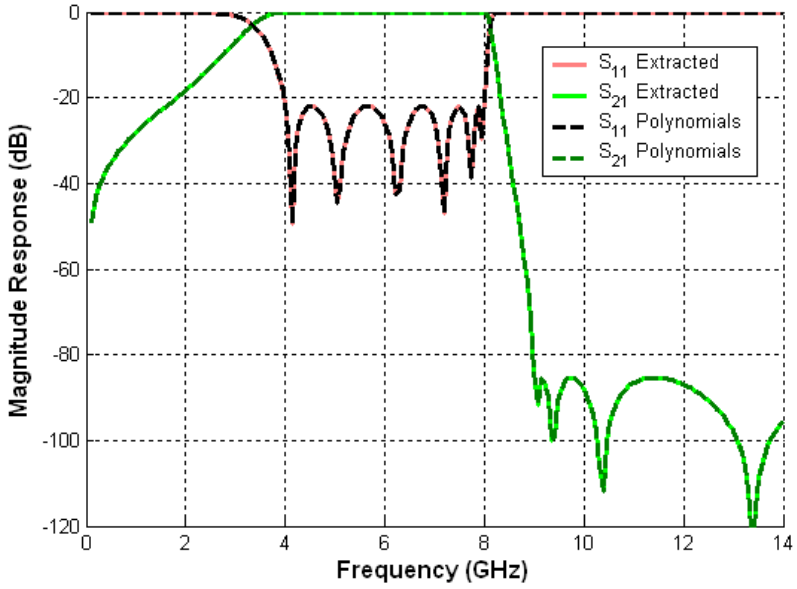

(b)

Figure 3.14. (a) Topology and coupling diagram and (b) frequency responses of the first six-degree filter example. The solid circles are the source/load nodes. The empty circles are the *LC* resonators. The solid lines are the coupling inverters: *L* denotes the inductive type, *C* denotes the capacitive type, and *L/C* denotes the composite type.

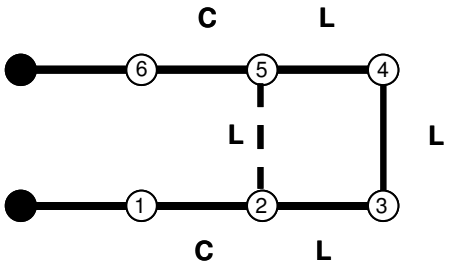

(a)

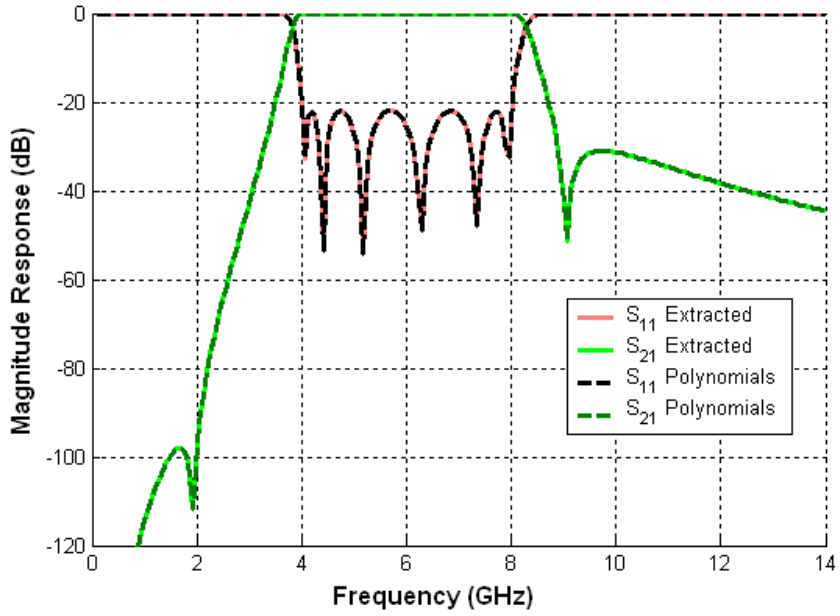

(b)

Figure 3.15. (a) Topology and coupling diagram and (b) frequency responses of the second six-degree filter example.

The same filter specification is taken for the second example, except that there is one transmission zero at each side of the filter passband. The resonators topology and coupling scheme of this filter example is shown in Fig. 3.15 (a). For this example, both inductive and capacitive frequency-dependent coupling inverters are presented.

Moreover, in order to avoid the asymmetric cross-coupling $M_{2,4}$ or $M_{1,5}$, the locations of two transmission zeros should be carefully selected. The order of transmission zero at dc is chosen as five.

The same synthesis and extraction procedures are carried out. The extracted values of circuit elements are: C_i = [0.3207, 11.3379, 0.000479, 0.000479, 11.3379, 0.3207], L_i = [0.1351, 0.0028, 48.8170, 48.8091, 0.0028, 0.1351], $C_{12} = L_{23} = L_{45} = C_{56} = 1$, L_{34} = -125.8058, and L_{25} = 0.0361. The filter responses from the polynomials and from the extracted circuit elements are shown in Fig. 3.15 (b). Again, there is no observed difference between these responses. The asymmetry on the locations of two transmission zeros about the center frequency is observed, although the values of coupling inverters and the resonators are symmetric about the horizontal middle-plane of the circuit network.

Chapter 4 Wideband Microwave Filters Designs

4.1 DESIGN METHODOLOGY

4.1.1 Overview

Several examples of filter designs and realizations are given in this Chapter to demonstrate the synthesis technique introduced in the previous two Chapters. Also some design aspects previously discussed will be further clarified according to the physical designs. These filter examples are realized using Low Temperature Co-fired Ceramic (LTCC) technology, which has been briefly introduced in Chapter One.

4.1.2 Coupling Structures

In Section 1.2, a combline-like resonator realized in LTCC technology has been introduced. Four coupling structures formed by combline-like resonators are investigated in this sub-Section. As shown in Fig. 1.3 (b), the magnetic field is circulating around the post. By placing two posts close to each other, the magnetic fields will interact to provide inductive coupling between the two resonators. One type of magnetic coupling structure is shown in Fig. 4.1, where two posts are shorted

at the same ground plane (arranged in the same direction). The amount of magnetic coupling can be controlled by the distance *D*. The bottom view of magnetic fields is shown in Fig. 4.1 (d). The dimensions shown in Fig. 4.1 result in the resonant frequency f_0 = 3.8623 GHz, the magnetic coupling coefficient k_M = 0.2813, and the electric coupling coefficient k_E = -0.0197. The definition of these parameters and how to obtain these parameters will be given in the next sub-section.

Another type of magnetic coupling structure is shown in Fig. 4.2, where two posts are shorted at the opposite ground plane (arranged in the opposite direction). The amount of magnetic coupling can be also adjusted by the distance *D*. But the field vector of magnetic fields in Fig 4.2 (d) displays completely different pattern than those in Fig 4.1 (d). Therefore, the interaction of magnetic fields between the two posts in one structure is in-phase, while in the other structure out-of-phase. Importantly, the in- and out-of-phase of magnetic fields can represent positive and negative inductive coupling in practical filter design, respectively. In both cases, magnetic field coupling is predominant. The dimensions shown in Fig. 4.2 result in the resonant frequency f_0 = 3.8379 GHz, the magnetic coupling coefficient k_M = -0.2756, and the electric coupling coefficient k_E = 0.0516.

As shown in Fig. 1.3 (a), the electric fields are concentrated between the conductor patch and the ground plane. By overlapping the conducting patches, the electric fields will interact to provide capacitive coupling between the two resonators. One type of electric coupling structure is shown in Fig. 4.3, where an additional floating

conductor patch is inserted between the patches of the resonators and the ground plane. A conducting wall is placed between the two posts of the resonators, blocking the coupling of magnetic fields. An opening window is made on the conducting wall so that the floating patch can pass through, avoiding being shorted to the ground. The field pattern of electric fields in resonator area is shown in Fig. 4.3 (d), whereas the electric fields are confined between the floating patch and the patches of two resonators. The floating patch acts as a *medium* to electrically couple the two resonators. The amount of electric coupling can be controlled by the size of the overlapping area between the floating patch and the patches of the two resonators. As shown in Fig. 4.3 (c), if the width of the floating patch is fixed to the width of the resonator patches, the length of the floating patch D can be adjusted to control the electric coupling. The dimensions shown in Fig. 4.3 result in the resonant frequency f_0 = 4.2131 GHz, the magnetic coupling coefficient k_M = 0.0412, and the electric coupling coefficient $k_E = 0.1550$.

Another type of electric coupling is shown in Fig. 4.4, where the two resonators are directly coupled by their patches with one resonator flipped and shorted at the opposite ground plane. Two additional ground planes are inserted in the middle of the structure so that the patches of the two resonators are sandwiched in between. The main purpose of these two additional ground planes is to enhance the capacitance between the patches of the two resonators and the ground planes so that stronger electric coupling can be achieved. An extra feature is of course to block a portion of magnetic field coupling. Similarly to the previous structure, an opening aperture

slightly larger than the cross section of the resonator posts is made on each middle ground plane so that the post of the resonator can pass through, avoiding being shorted to the middle ground plane. The field pattern of electric fields in the resonator area is shown in Fig. 4.4 (d), whereas it is clear that most of the electric field is confined within the overlapping area of the two resonator patches. Due to the small gap, relatively large capacitance can be achieved. Therefore, the amount of electric coupling can be simply adjusted by the size of this overlapping area, which as shown in Fig. 4.4 (b) and (c) is controlled by the distance *D*. In both cases, electric field coupling is predominant. The dimensions shown in Fig. 4.4 result in the resonant frequency f_0 = 2.9222 GHz, the magnetic coupling coefficient k_M = -0.0093, and the electric coupling coefficient k_E = 0.2709.

For all examples and realizations shown from Fig. 4.1 to Fig.4.4, the dielectric constant of LTCC substrate is 7.7 and the thickness of each LTCC layer is 3.94 mil. The finite element electromagnetic (EM) simulator HFSS, High Frequency Structure Solver from Ansys [58] is used in this and subsequent Sections. The simulation results from HFSS have been compared extensively with another EM simulation technique, Mode-Matching [59] for accuracy. Also, the simulation results from HFSS have also been compared against measurement results. Some of measurement results will be given in subsequent Sections.

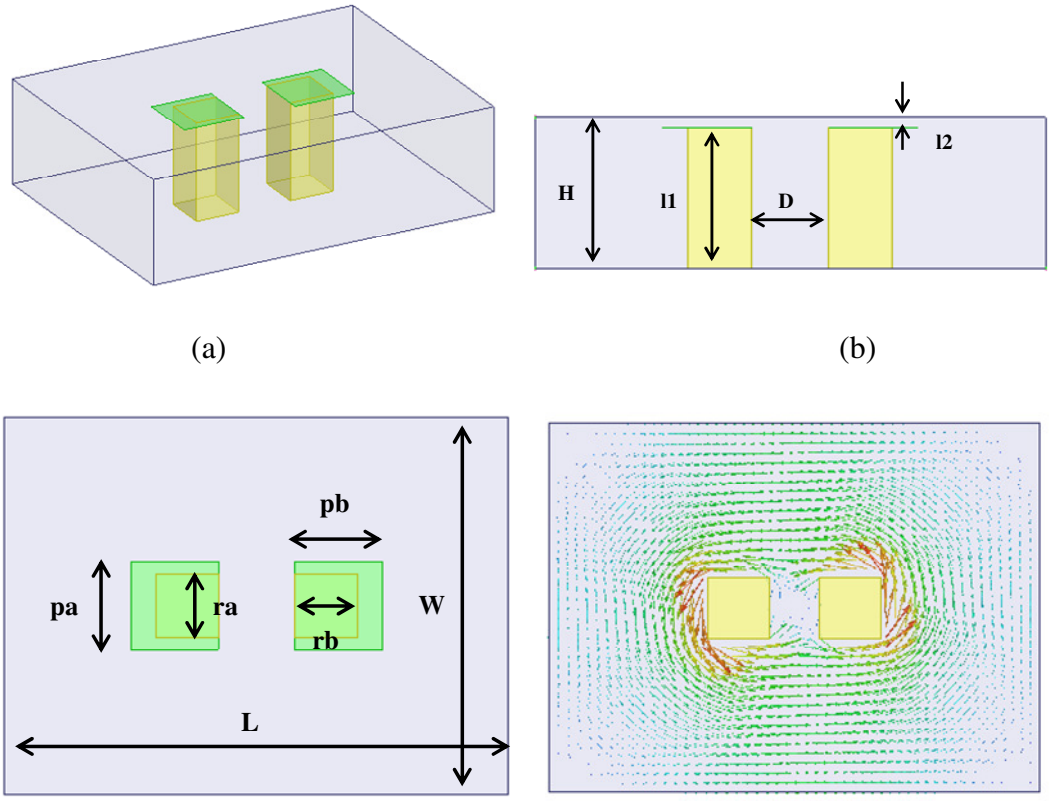

(a) (b)

(c) (d)

Figure 4.1. Magnetic coupling structure I, (a) resonators are in the same direction; (b) and (c) dimensions; (d) the surrounding magnetic field (bottom view). Dimensions in mil: $W = 300$, $L = 400$, $pa = 70$, $pb = 70$, $ra = 50$, $rb = 50$, $H = 118.2$, $D = 70$, $l1 = 110.32$, and $l2 = 7.88$. (Dielectric constant = 7.7).

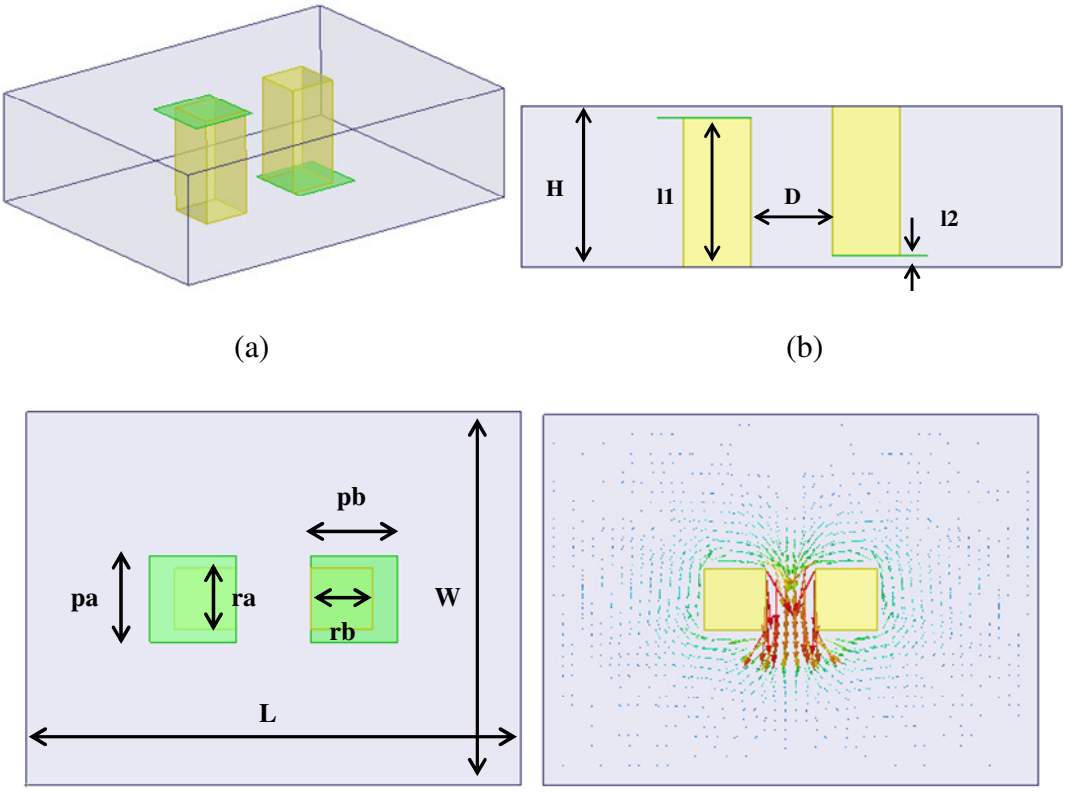

(a) (b)

(c) (d)

Figure 4.2. Magnetic coupling structure II, (a) resonators are in the opposite direction; (b) and (c) dimensions; (d) the surrounding magnetic field (bottom view). Dimensions in mil: W = 300, L = 400, pa = 70, pb = 70, ra = 50, rb = 50, H = 118.2, D = 70, $l1$ = 110.32, and $l2$ = 7.88. (Dielectric constant = 7.7).

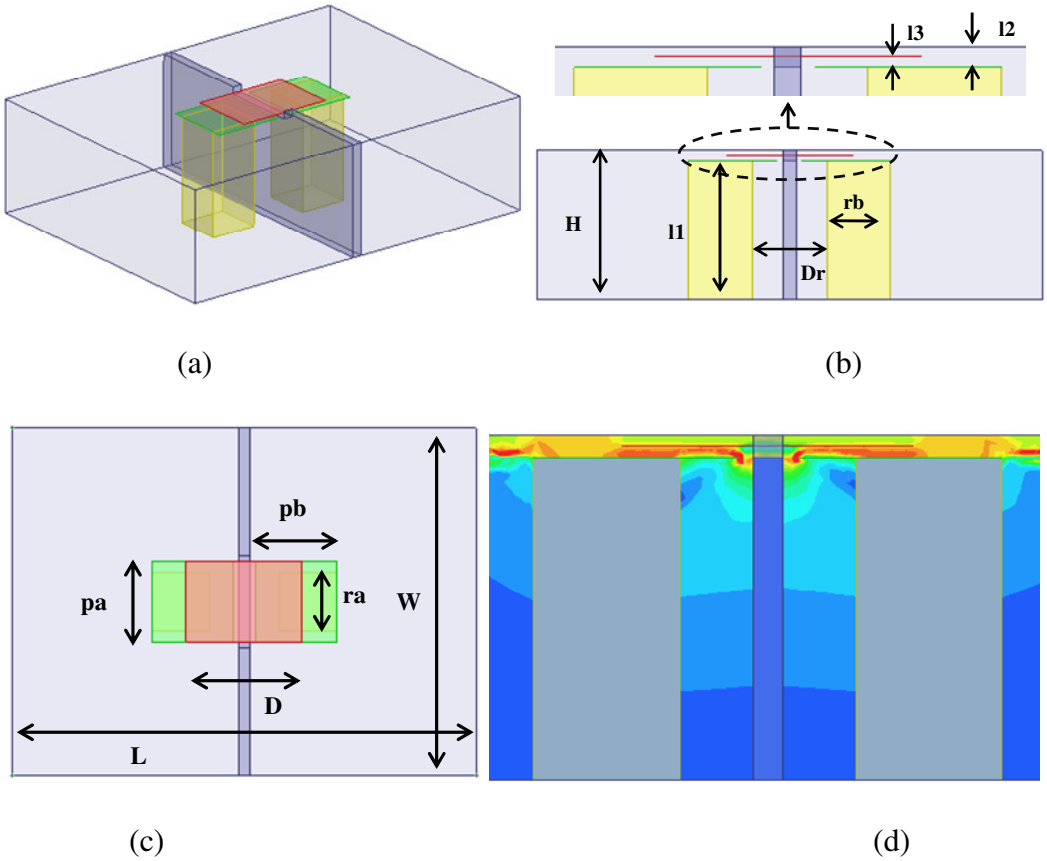

(a) (b)

(c) (d)

Figure 4.3. Electric coupling structure I, (a) coupled by an additional floating conductor patch; (b) and (c) dimensions; (d) the electric field in patches area (side view). Dimensions in mil: W = 300, L = 400, pa = 70, pb = 70, ra = 50, rb = 50, H = 118.2, D = 100, $l1$ = 110.32, $l2$ = 7.88, $l3$ = 3.94, and Dr = 60. (Dielectric constant = 7.7).

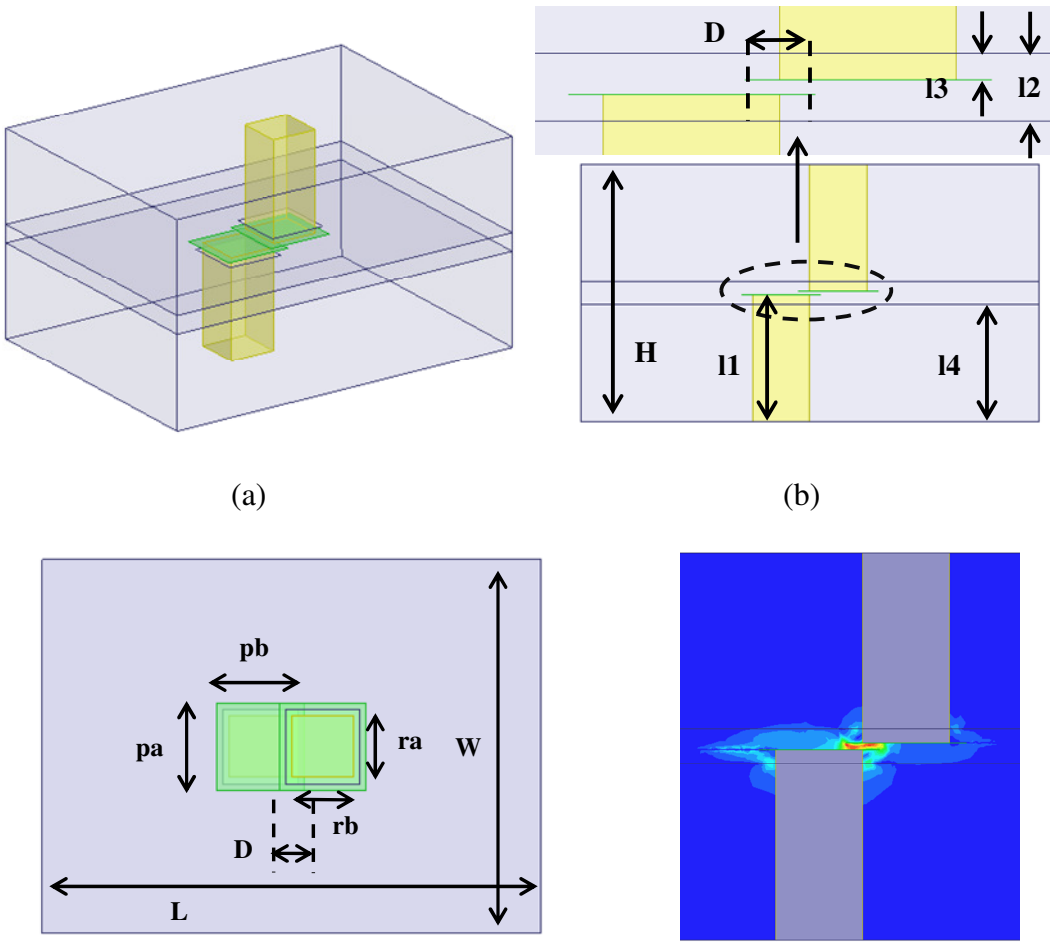

Figure 4.4. Electric coupling structure II, (a) directly coupled by the overlapping of two conductor patches; (b) and (c) dimensions; (d) the electric field in patches area (side view). Dimensions in mil: $W = 300$, $L = 400$, $pa = 70$, $pb = 70$, $ra = 50$, $rb = 50$, $H = 224.58$, $D = 20$, $l1 = 110.32$, $l2 = 19.7$, $l3 = 7.88$, and $l4 = 102.44$. (Dielectric constant = 7.7).

4.1.3 Resonant Frequency and Coupling Coefficient

Since the dimensions of the two resonators are identical for the four coupling structures mentioned in the previous sub-Section, the equivalent circuit model of a second-order filter with a composite type coupling inverter shown in Fig. 3.8 are used to analyze the coupling coefficient for all four coupling structures.

The element values of the equivalent circuit can be extracted from the EM simulation results of coupling structures with the method of even- and odd-mode excitation. The detailed derivation of extraction method is presented in Appendix B. The extracted values can be normalized using similar equations mentioned in (2.128)

$$\omega_{0i} = \frac{1}{\sqrt{L_i C_i}}$$

$$k_{ij}^{L} = \frac{1/\left(\omega_0 L_{ij}\right)}{\sqrt{1/\left(\omega_{0i} L_i\right) \cdot 1/\left(\omega_{0j} L_j\right)}}$$

$$k_{ij}^{C} = \frac{-\omega_0 C_{ij}}{\sqrt{\omega_{0i} C_i \omega_{0j} C_j}}$$

$$Q_{e1} = \omega_{01} C_1, Q_{en} = \omega_{0n} C_n \tag{4.1}$$

where ω_0 is the center angular frequency of the filter passband, ω_{0i} is the resonant angular frequency of the *i*th resonator, k_{ij}^{L} and k_{ij}^{C} are the inductive (magnetic field) and capacitive (electric field) coupling coefficients, respectively, and Q_{e1} and Q_{en} are the external Q factor for input and output couplings, respectively. Assuming the two resonators are identical and the resonant frequency is also identical to the center

frequency, Eq. (4.1) can be simplified as

$$k_M = \frac{L}{L_m} \text{ and } k_E = \frac{C_m}{C} \tag{4.2}$$

where $k_M = k_{ij}^L$, $k_E = k_{ij}^C$, $L = L_i = L_j$, $C = C_i = C_j$, $L_m = L_{ij}$, and $C_m = C_{ij}$ for the second-order filter. Eq. (4.2) is the exact one found in (3.65), which have been previously defined as the coupling coefficients.

For the magnetic coupling structures in Fig. 4.1 and Fig. 4.2, k_M is predominant and k_E is a spurious coupling element, and the magnetic coupling is primarily controlled by the distance *D*. The curves of the coupling coefficient versus the distance *D* are given in Fig. 4.5 (a) and (b), respectively. Note that the extracted k_M has different sign in these two curves, which evidently shows the positive and negative inductive couplings. The curves of the resonant frequency f_0 versus the distance *D* are also given in Fig. 4.5 (a) and (b), respectively. Due to the similarity between the two structures, the change of the f_0 is in very similar trend in the two curves.

For the electric coupling structures in Fig. 4.3 and Fig. 4.4, k_E is predominant and k_M is a spurious coupling element, and the electric coupling is primarily controlled by the distance *D* as well. The curves of the coupling coefficient versus the distance *D* are given in Fig. 4.5 (c) and (d), respectively. Note that the extracted k_E in Fig. 4.5 (d) is relatively larger than those in Fig. 4.5 (c), which is expected. The curves of the resonant frequency f_0 versus the distance *D* are also given in Fig. 4.5 (c) and (d),

respectively. Due to the patches of the resonators in Fig. 4.4 (a) are heavily loaded with the middle ground planes, it is seen that the f_0 in Fig. 4.5 (d) is significantly lower than those in Fig. 4.5 (a) - (c), though the physical dimensions of the resonators remain identical. Therefore, the size of the patch and/or the length of the post may need to be adjusted in order to obtain the proper resonant frequency.

The coupling coefficient k and resonant frequency f_0 curves shown in this sub-Section may serve as an essential tool in practical filter design. After the element values of the equivalent filter circuit model are synthesized using the techniques introduced in either Chapter Two or Chapter Three, the critical initial dimensions of physical structures can be interpolated from these or similar coupling coefficient curves. This is one of most important steps in filter design practice, since accurate initial dimensions can quickly lead to the converged optimum solution with minimum effort of optimization.

In addition to the coupling coefficients, the input and output couplings can also be extracted from EM simulation results through the external Q_e factors given in Eq. (4.1). Since the tapped-in stripline is used as the input/output coupling structure, the amount of input/output couplings is usually proportional to the width of the input/output stripline. Therefore, it is very straightforward to obtain.

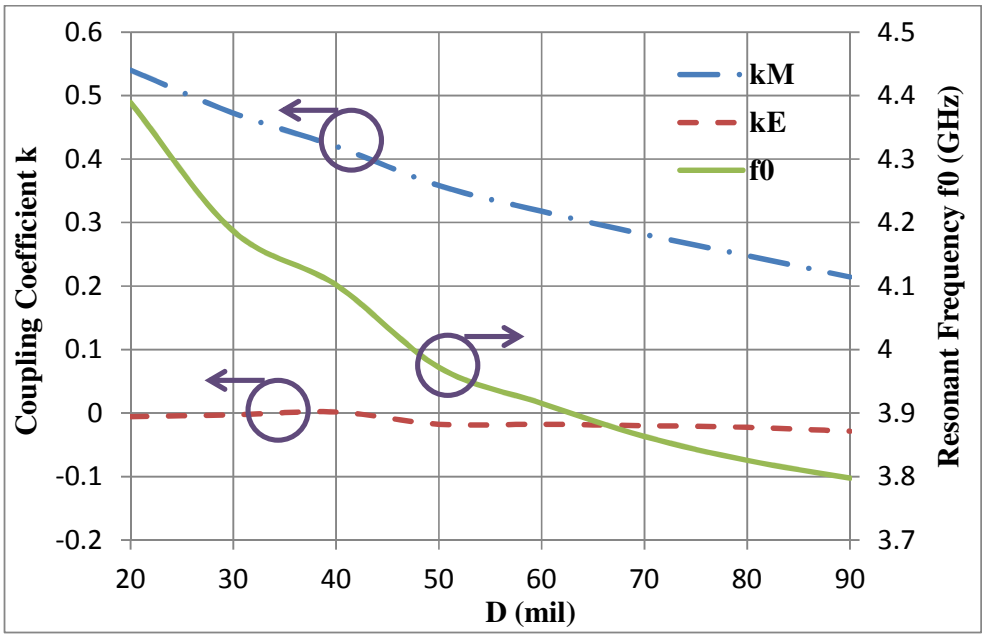
Coupling Coefficient k
Resonant Frequency f0 (GHz)
D (mil)
kM
kE
f0
0.6
0.5
0.4
0.3
0.2
0.1
0
-0.1
-0.2
4.5
4.4
4.3
4.2
4.1
4
3.9
3.8
3.7
20
30
40
50
60
70
80
90

(a)

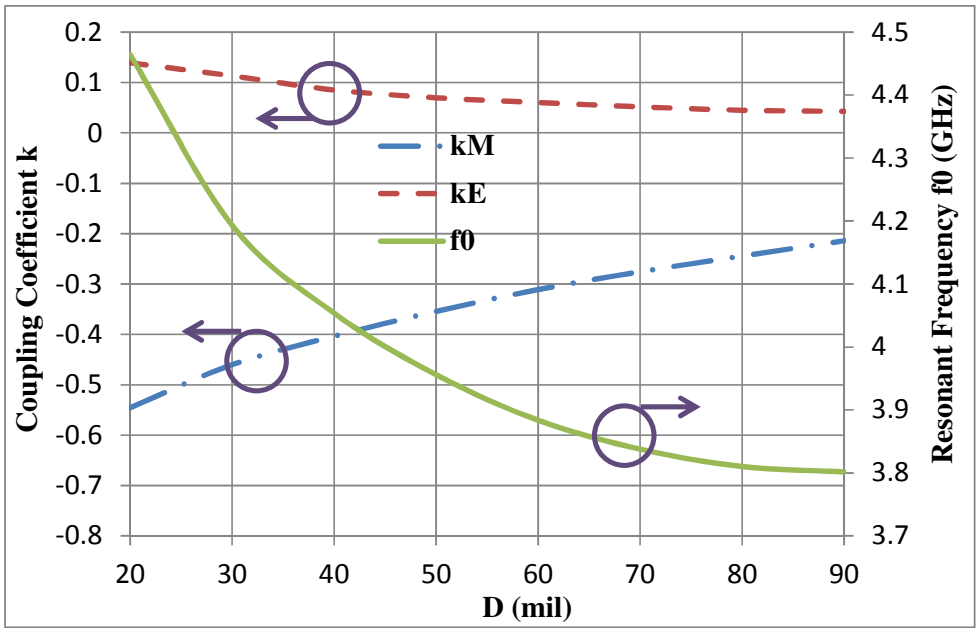
Coupling Coefficient k
Resonant Frequency f0 (GHz)
D (mil)
kM
kE
f0
0.2
0.1
0
-0.1
-0.2
-0.3
-0.4
-0.5
-0.6
-0.7
-0.8
4.5
4.4
4.3
4.2
4.1
4
3.9
3.8
3.7
20
30
40
50
60
70
80
90

(b)

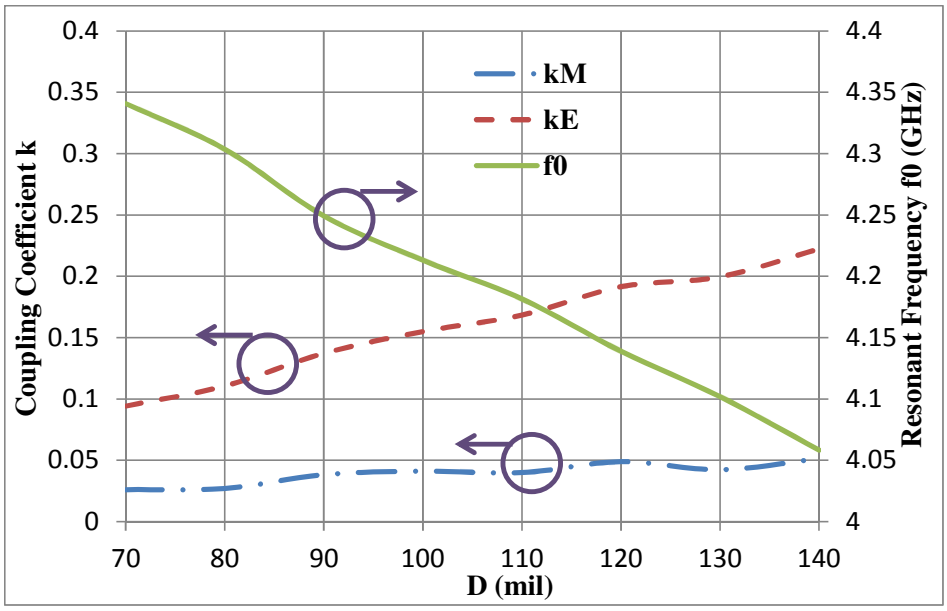

(c)

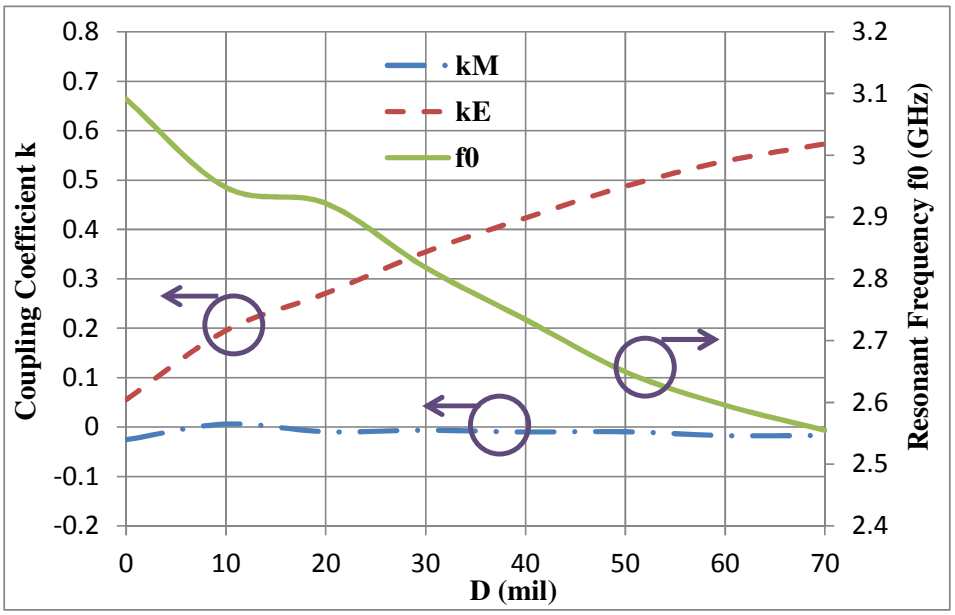

(d)

Figure 4.5. Magnetic and electric coupling coefficient k and resonant frequency f_0 curves of the four coupling structures versus the distance D: (a) for the structure in Fig. 4.1 (a); (b) for the structure in Fig. 4.2 (a); (c) for the structure in Fig. 4.3 (a); (d) for the structure in Fig. 4.4 (a).

4.2 ALL INDUCTIVE-COUPLED AND ALL CAPACITIVE-COUPLED LTCC FILTERS

4.2.1 All Inductive Coupled LTCC Filter

Two design examples of microwave filters are presented using the synthesis techniques introduced in Section 2.6, implemented and simulated in EM simulator HFSS to demonstrate the validity of the synthesis techniques. The first example is a fourth-degree 22-dB return loss filter with center frequency f_0 = 3.9 GHz and bandwidth BW = 2.1 GHz (54% relative bandwidth). This filter is realized with all inductive coupling elements in an inline structure as shown in Fig. 4.6 (a).

Using the synthesis technique outlined in Section 2.6, the synthesized values of circuit elements are: L (in nH) = $diag$(0.0224, 0.0380, 0.0380, 0.0224); C (in nF) = $diag$(0.0646, 0.0380, 0.0380, 0.0646); L_{12} = 0.0644 nH, L_{23} = 0.1148 nH, and L_{34} = 0.0644 nH. The number p (order of transmission zero at zero frequency) in the characteristic function (2.8) is prescribed as one. One may find that it would be more convenient to represent the circuit parameters in terms of normalized elements $f_0/k/Q_e$ in (4.1), instead of L/C. The filter responses from the synthesized circuit elements are shown in Fig. 4.6 (b).

The combline-like resonators in Fig. 1.2 with the coupling structure in Fig. 4.1 (a) are used to realize this filter, since the inductive couplings are going to be realized

among resonators according to the synthesized circuit elements. The EM model of the physical structure in HFSS is shown in Fig. 4.7. Usually, the cross section and length of the metallic post is fixed, and then the resonant frequency of the resonator is adjusted by the dimensions of the conductor patch. The initial distances between the metallic posts, primarily determining the amount of inductive coupling are interpolated from the coupling coefficient curve similarly to that shown in Fig. 4.5 (a). By implementing this scheme, the resonant frequencies of the resonators and the couplings between the resonators can be controlled independently.

After obtaining the initial dimensions, the complete EM model is simulated and fine-tuned in HFSS. Since this filter structure is relatively simple and the initial dimensions are very close to the final ones, the full-wave optimization may not be required for this case, although the optimization on the 3D physical model is very useful and applied in other more complex filter structures in the following sections. The EM simulation results are also given in Fig. 4.6 (b), which are very close to the responses from the synthesized circuit model.

The EM model with solid vertical walls in Fig. 4.7 (a) is then converted to the model, conventionally called *via* model as showing in Fig. 4.8 (a), using the implementation of LTCC technology given in Fig. 1.1. Additionally, the stripline transitions from the input/output coupling striplines of the filter structure to 50 Ohm and the launches used by probe station for measurement are included in the final realization. The measurement setup is shown in Fig. 4.8 (b) with a fabricated filter

device. Four resonator posts can be clearly observed from the device.

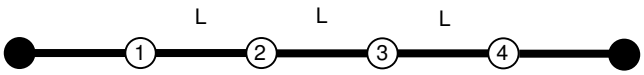

(a)

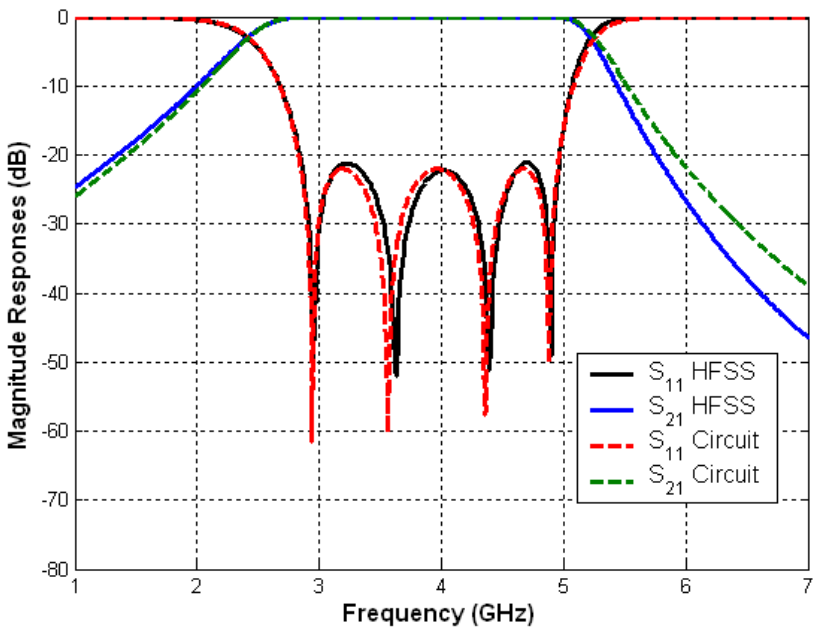

(b)

Figure 4.6. (a) Topology and coupling diagram and (b) the responses of the fourth-degree filter example. The solid circles are the source/load nodes. The empty circles are the *LC* resonator. The solid lines are the coupling inverters, *L* denotes the inductive type.

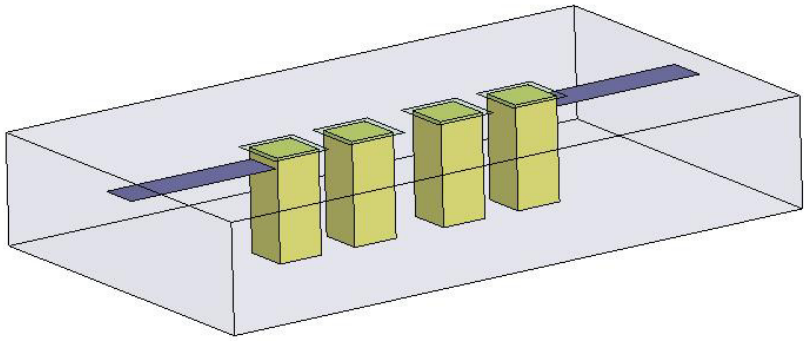

(a)

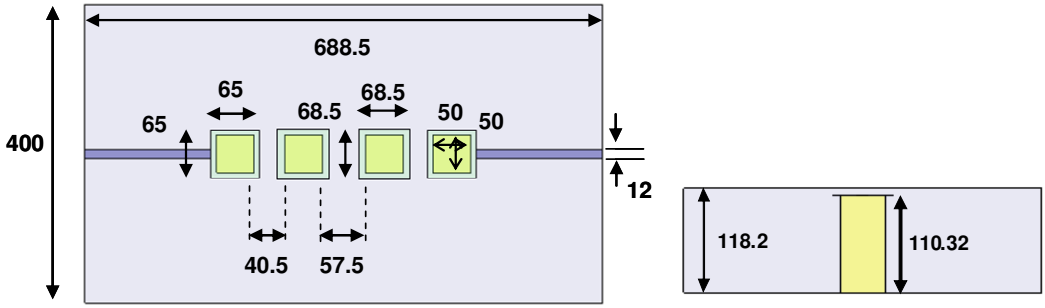

(b)

Figure 4.7. (a) Physical structure and (b) dimensions of the fourth-degree filter example in HFSS. (unit: mil, dielectric constant = 7.6)

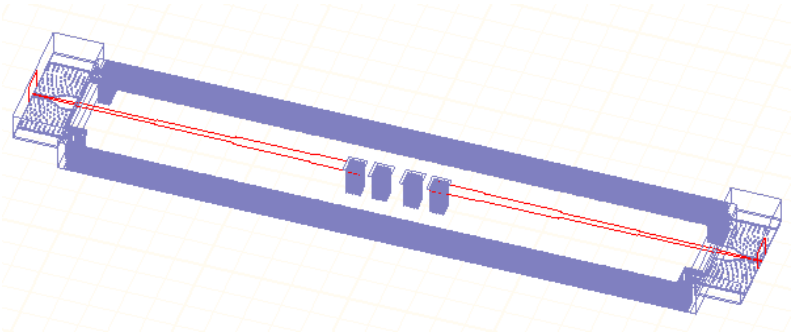

(a)

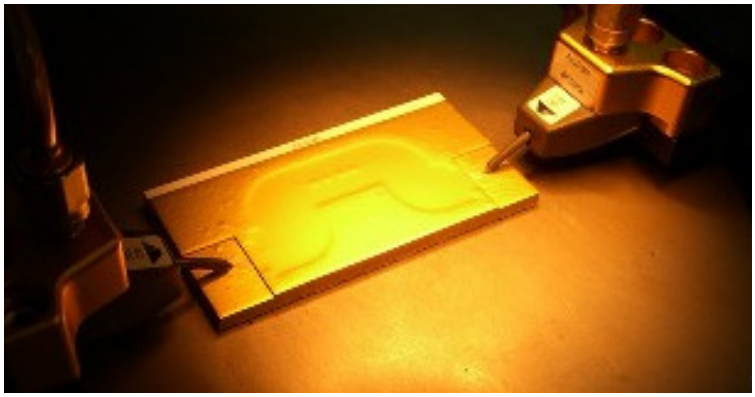

(b)

Figure 4.8. (a) Final realization of the fourth-degree filter example in via model with stripline transitions and launches in HFSS simulator. (b) Fabricated filter example in measurement.

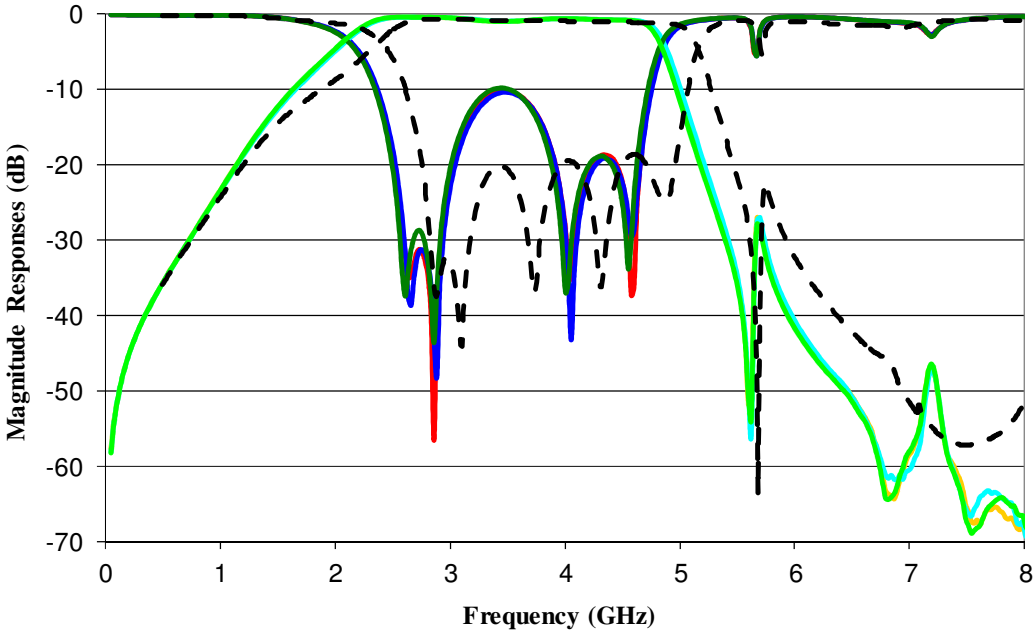

Figure 4.9. Measurement results of the fourth-degree filter example: the dashed lines are from HFSS simulation of final realization model; all other solid lines are from measurements of different fabricated filters.

Several measurement results are superimposed together in Fig. 4.9, along with HFSS simulation result of the final realization model. The measured results are very consistent among different pieces of fabricated filters, but a frequency down shift on filer pass-band is observed. The deteriorated in-band return-loss may be caused by incorrect inductive couplings, but the filter bandwidth is properly maintained.

4.2.2 All Capacitive Coupled LTCC Filter

The second design example is to demonstrate an inline realization with all

capacitive coupling elements as shown in Fig. 4.10 (a). This filter is designed as third-degree 20-dB return loss with center frequency f_0 = 1.42 GHz and bandwidth BW = 0.42 GHz (30% relative bandwidth).

Again, the synthesis technique outlined in Section 2.6 is used. The synthesized values of circuit elements are: L (in nH) = *diag*(0.0397, 0.1184, 0.0397); C (in nF) = *diag*(0.3465, 0.1184, 0.3465); $C_{12} = C_{23} = 0.0584$ nF. The number p in the characteristic function (2.8) is prescribed as five for this example. As shown in the simulation results of the synthesized circuit elements in Fig. 4.10 (b), the response is significantly sharper in the lower stopband than that in the upper stopband, since the number of transmission zeros at infinity is much less than that at zero frequency.

For this example, the combline-like resonators in Fig. 1.2 are used, and the capacitive couplings are realized by the direct overlapping of the conductor patches. The EM model of physical structure in HFSS is shown in Fig. 4.11. The design methodology is similar to the fourth-degree filter in the previous sub-Section. The strength of capacitive coupling is proportional to the size of the overlapping area, if the gap between the two conductor patches is fixed to one LTCC layer. The actual size can be interpolated from the coupling coefficient curves similar to that shown in Fig. 4.5 (d). Additional, conducting walls are placed between resonators to block the inductive couplings, which is similar to the implementation in Fig. 4.3. The EM simulation results are also given in Fig. 4.10 (b), which are very close to the responses from the synthesized circuit model.

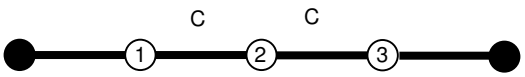

(a)

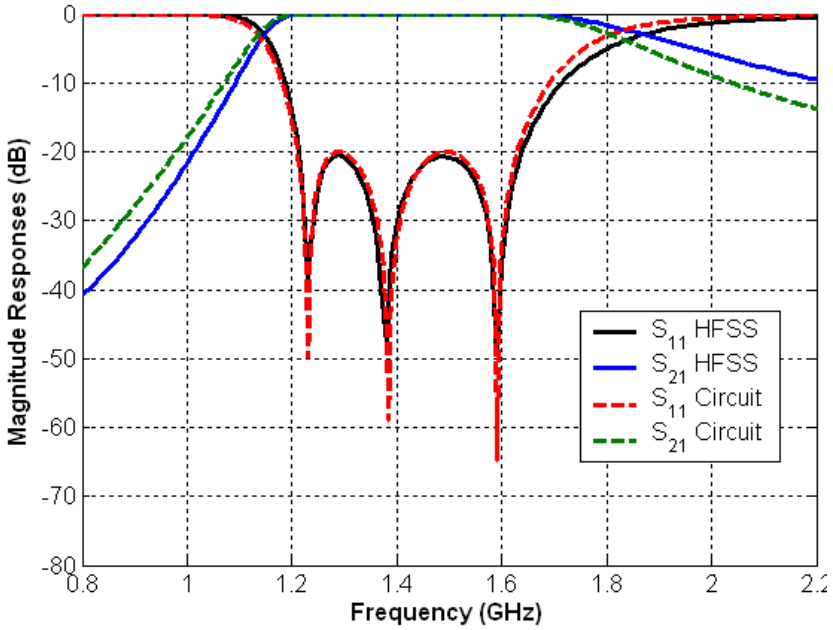

(b)

Figure 4.10. (a) Topology and coupling diagram and (b) the responses of the third-degree filter example. *C* denotes the capacitive coupling.

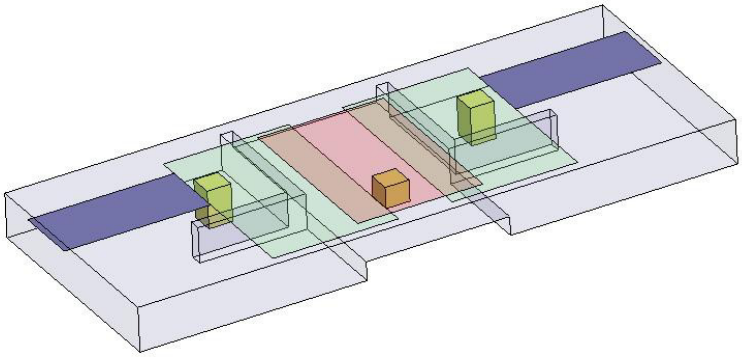

(a)

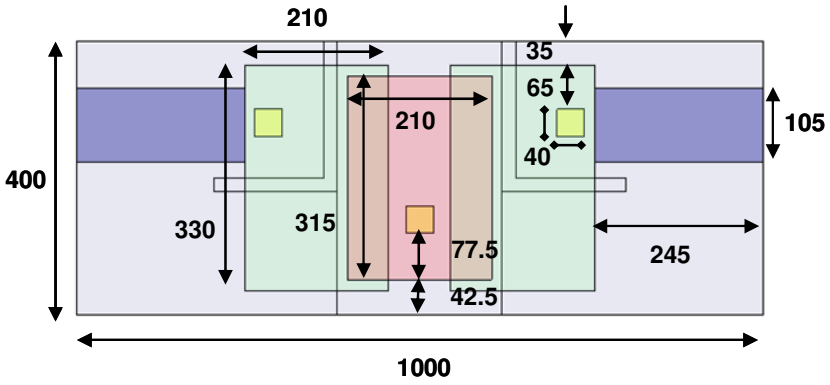

(b)

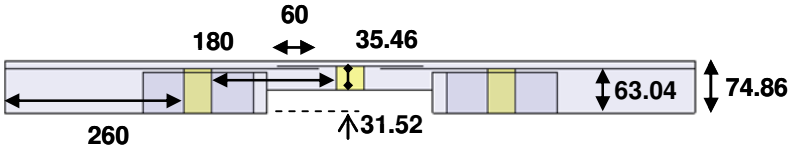

(c)

Figure 4.11. (a) Physical structure and (b)-(c) dimensions of the third-degree filter example in HFSS. (unit: mil, dielectric constant = 7.7)

4.3 WIDEBAND RIDGE WAVEGUIDE AND COMBLINE-LIKE FILTERS

4.3.1 Wideband Ridge Waveguide Filter

Ultra-wideband ridge waveguide filters in LTCC realization have been introduced in [53]-[54]. The evanescent mode coupling between ridge sections can be treated as dominant inductive couplings. Therefore, conventional ridge waveguide filters without cross couplings are a form of an inline filter structure with all inductive coupled elements as presented in Section 4.2.1.

Both the analytical synthesis techniques by coupling matrix approach in Section 2.6 and by cascade synthesis of circuit network approach in Section 3.5 are capable of obtaining the values of circuit elements. In this sub-section, a ridge waveguide filter is used to demonstrate that the synthesized values of circuit elements from the two different approaches are essentially identical.

The filter example is a seventh-degree 22-dB return loss filter with center frequency f_0 = 7.28 GHz and bandwidth BW = 3 GHz (41% relative bandwidth). The coupling diagram is shown in Fig. 4.12 (a).

Using the synthesis technique outlined in Section 2.6, the synthesized values of circuit elements are:

L_i (in nH): 0.0090, 0.0211, 0.0213, 0.0214, 0.0213, 0.0211, 0.0090

C_i (in nF): 0.0494, 0.0211, 0.0213, 0.0214, 0.0213, 0.0211, 0.0494

L_{12} (= L_{67} in nH) = 0.0412, L_{23} (= L_{56} in nH) = 0.0900

and L_{34} (= L_{45} in nH) = 0.0952 (4.3)

Using the synthesis technique outlined in Section 3.5, the synthesized values of circuit elements are:

L_i (in nH): 0.0090, 0.3148, 0.0045, 0.2855, 0.0045, 0.3148, 0.0090

C_i (in nF): 0.0494, 0.0014, 0.1020, 0.0016, 0.1020, 0.0014, 0.0494

$L_{12} = L_{23} = L_{34} = L_{45} = L_{56} = L_{67}$ (in nH) = 0.1592 (4.4)

It is obvious that the values shown in (4.3) and (4.4) are completely different, except for a few elements. Applying the equations in (4.1) to normalize the circuit element values in (4.3) and (4.4), the same normalized values are obtained:

f_i (in GHz): 7.5576, 7.5493, 7.4559, 7.4470, 7.4559, 7.5493, 7.5576

k^L_{ij}: 0.3464, 0.2429, 0.2297, 0.2297, 0.2429, 0.3464

$Q_{e(1,n)}$: 2.3475, 2.3475 (4.5)

Therefore, it is best to design the filter based on the normalized values of circuit elements after the synthesis of circuit model is carried out by either technique. The design of ridge waveguide filter can be implemented by the Mode-Match technique [59] or other means [60], and is not repeated here.

The EM structure of ridge waveguide filter and its dimensions are shown in Fig. 4.13. Both the simulation results of the circuit model with synthesized circuit element values and the EM model in HFSS are superimposed in Fig. 4.12. They agree with each other very well over a broad frequency range.

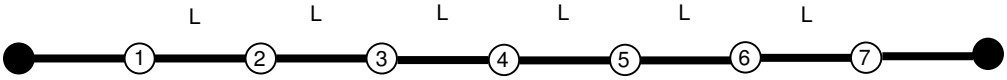

(a)

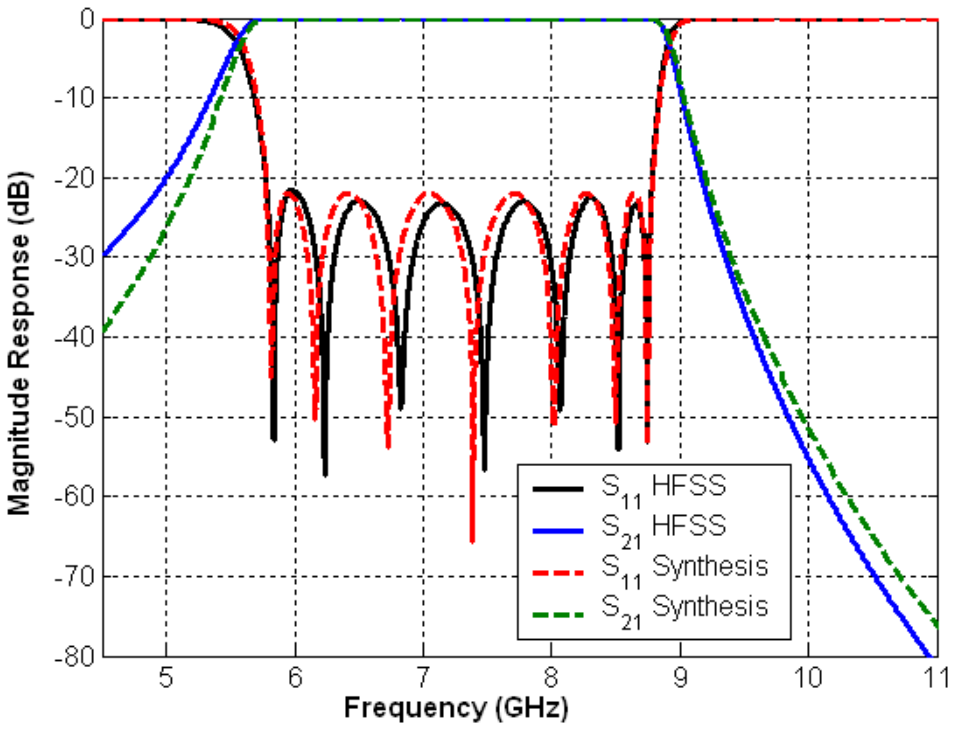

(b)

Figure 4.12. (a) Topology and coupling diagram and (b) the responses of the seventh-degree ridge waveguide filter.

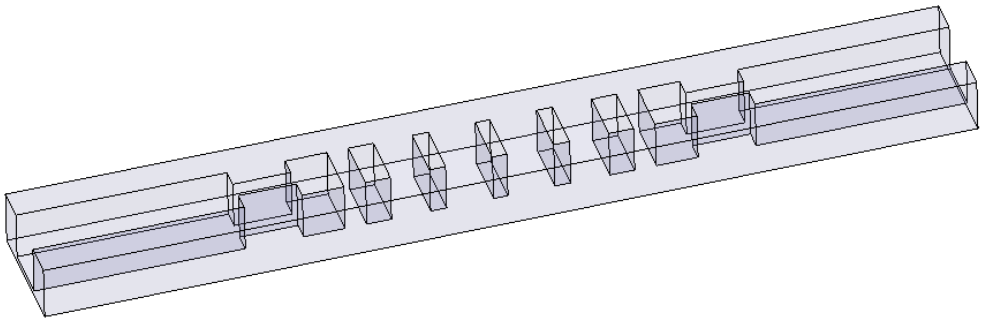

(a)

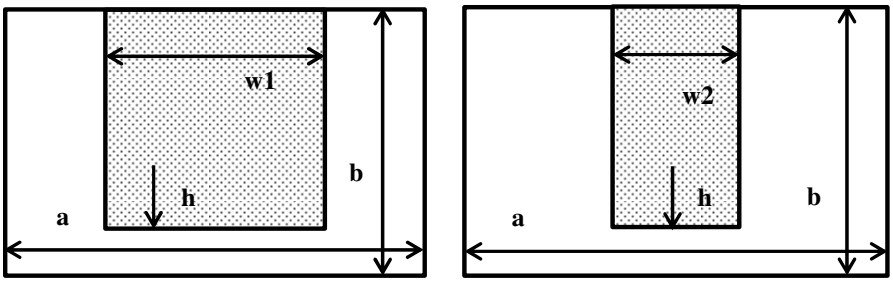

(b)

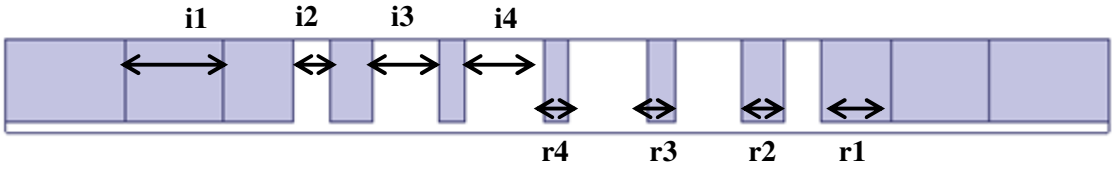

(c)

Figure 4.13. (a) Physical structure and (b)-(c) dimensions of the seventh-degree LTCC ridge waveguide filter in HFSS. (unit: mil, dielectric constant = 7.6): *a* = 180, *b* = 78.8, *h* = 7.88, *w1* = 81, *w2* = 27, *r1* = 59.23, *r2* = 35.19, *r3* = 22.80, *r4* = 20.46, *i1* = 82.61, *i2* = 30.66, *i3* = 55.58, and *i4* = 66.53.

4.3.2 Wideband Combline-Like LTCC Filter with Alternative Capacitive and Inductive Couplings

The design example in this sub-section is a seventh-order filter with alternative capacitive and inductive couplings. The filter has 20-dB return loss with center frequency f_0 = 1 GHz and bandwidth BW = 0.56 GHz (56% relative bandwidth). Due to the consideration on the filter layout and physical realization, the sequence of coupling elements is selected as, C_{12}, L_{23}, C_{34}, C_{45}, L_{56}, and C_{67} as shown in Fig. 4.14 (a).

As explained before, there is no analytic synthesis method for this case by coupling matrix approach in Chapter Two. Therefore, the optimization approach in Section 2.7 is used to get the values of coupling elements as well as resonant frequencies of resonators and external Q factors. The optimization routine in MATLAB converges in seconds. The optimized values are: f_{01} (= f_{07}) = 0.8654, f_{02} (= f_{06}) = 0.9615, f_{03} (= f_{05}) = 0.9684 and f_{04} = 0.8752 (GHz); k^C_{12} (= k^C_{67}) = -0.4771, k^L_{23} (= k^L_{56}) = 0.3177 and k^C_{34} (= k^C_{45}) = -0.3236; Q_{e1} (=Q_{e7}) = 1.9262. Because there are two inductive couplings and four capacitive couplings, the number p in the characteristic function (2.8) is prescribed as nine. The filter responses from the optimized circuit elements are shown in Fig. 4.14 (b).

Again, the combline-like resonator in Fig. 1.2 is used to realize the LC resonator in LTCC technology. The coupling structure in Fig. 4.4 is used to realize the capacitive

coupling, while the coupling structure in Fig. 4.1 is used to realize the inductive coupling. Therefore, this realization is a composite of two filter design examples in Section 4.2. The EM model of physical structure in HFSS is shown in Fig. 4.15. The initial dimensions of the distances between posts and the size of the overlapping of patches can be obtained from the corresponding curves of coupling coefficients, similar to previous filter design examples. Also, several conducting walls are placed to block inductive couplings among non-adjacent resonators, and two middle ground planes are inserted into the structure due to the requirement of capacitive coupling structure in Fig. 4.4. All conductor patches of the resonators are placed between these two middle ground planes. For a high-order filter example, the full-wave optimization on the entire EM model is necessary. As explained before, since the resonant frequencies and the inductive or capacitive couplings can be separately controlled by individual dimensions in one-to-one correspondence, the direct optimization in HFSS is very efficient to obtain an equi-ripple response as shown in Fig. 14 (b). There is excellent agreement between circuit and EM simulation results.

(a)

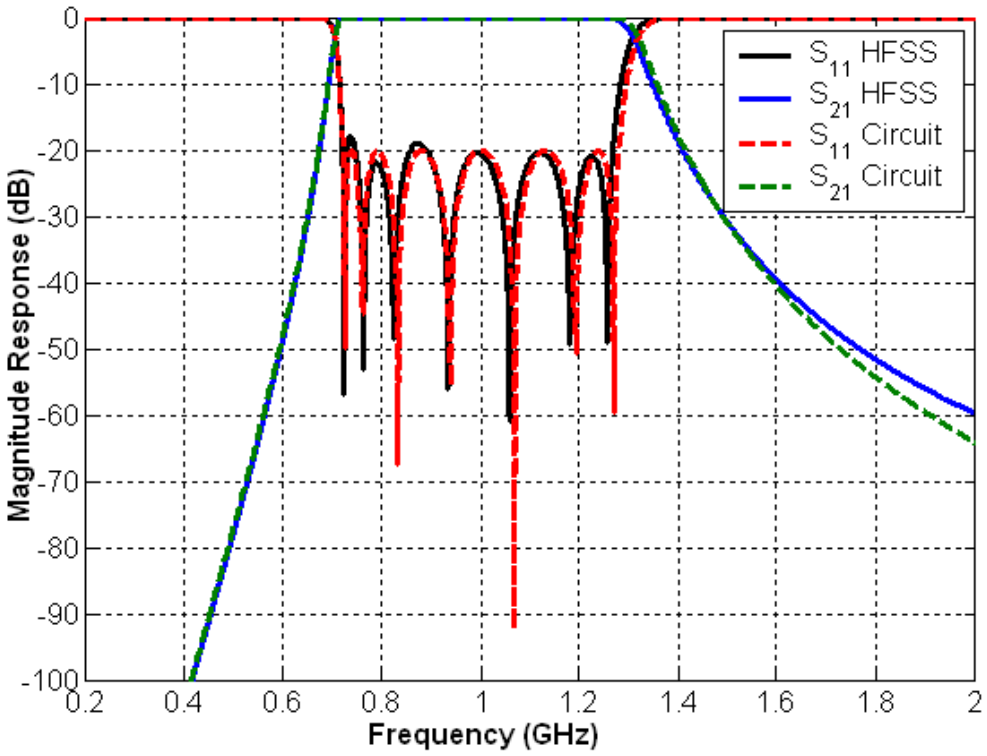

(b)

Figure 4.14. (a) Topology and coupling diagram and (b) the responses of the seventh-degree combline-like LTCC filter.

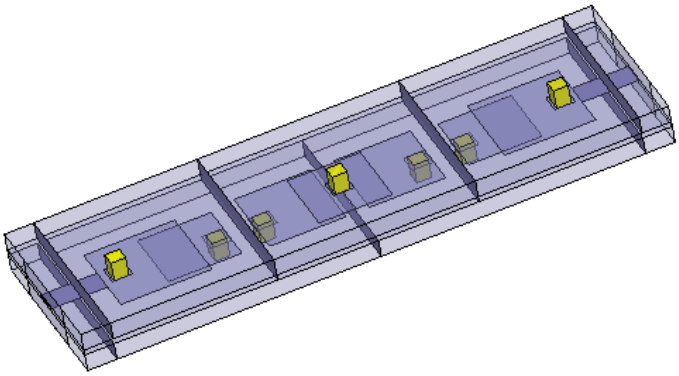

(a)

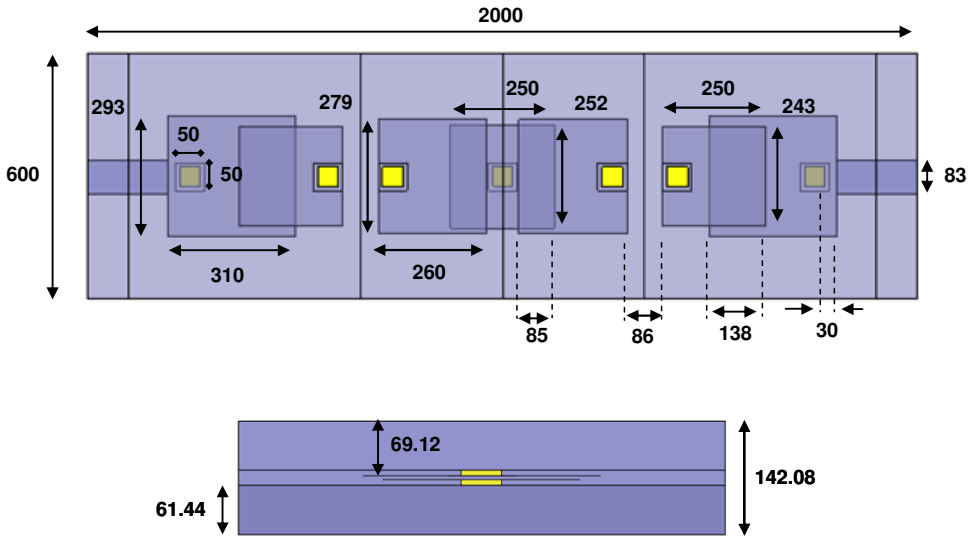

(b)

Figure 4.15. (a) Physical structure and (b) dimensions of the seventh-degree combline-like LTCC filter in HFSS. (unit: mil, dielectric constant = 7.7)

4.4 BANDWIDTH ENHANCEMENT BY NEGATIVE INDUCTIVE COUPLING

4.4.1 Negative Inductive Coupling

As introduced in Section 4.1, two magnetic coupling structures in Fig. 4.1 (a) and Fig. 4.2 (a) produced in- and out-of-phase magnetic field surrounding the resonator posts as shown in Fig. 4.1 (d) and Fig. 4.2 (d), respectively, representing positive and negative inductive couplings. This phenomenon is further investigated in this Section.

Fig. 4.16 (a) shows a two-pole filter realized in LTCC, where two metallic posts are shorted at the same bottom ground plane. Fig. 4.16 (b) shows another two-pole filter configuration in which the second post and its conducting patch are flipped so that the second post is shorted at the top ground plane. Note that the position and width of coupling striplines are also adjusted. According to the coupling coefficient definition in terms of the even- and odd-mode resonant frequency and the curves in Fig. 4.5 (a) and (b), the inductive coupling in Fig. 4.16 (a) is positive, and the inductive coupling in Fig 4.16 (b) is negative.

Fig. 4.17 shows the phase responses of S21 for the filter structures in Fig. 4.16 (a) and (b). There is almost 180-degree phase difference across the frequency range. Magnetic fields patterns similar to those shown in Fig. 4.1 (d) and Fig. 4.2 (d) indicate that when the magnetic field lines responsible for the coupling between two

resonators are in the same direction, the resulting coupling will be positive, while if the fields are in opposite direction, the coupling will be negative.

The frequency responses by EM simulator HFSS are also shown in Fig. 4.18, represented by solid lines and dot-dashed lines for the filter structures in Fig. 4.16 (a) and (b), respectively. Using the extraction method by even- and odd-mode excitation mentioned in Appendix B, the values of circuit elements according to the equivalent circuit model in Fig. 3.8 can be easily found from EM simulation results:

	k_M	k_E	*Bandwidth (GHz)*
(a)	0.3097	-0.0278	1.75
(b)	-0.2971	0.0425	1.94
(c)	-0.2984	0.0583	2.12

(4.6)

where the normalized coupling value k_M (magnetic coupling) and k_E (electric coupling) are derived according to Eq. 4.2. The positive k_M for (a) and negative k_M for (b) are clearly evident.

It is also observed from Fig. 4.18 that the bandwidth of the second structure is slightly increased. Therefore, for the third filter structure in Fig. 4.16 (c), the conductor patch is shifted by Dp = 10 mil toward the center, so that the capacitive coupling formed between the patches within the coupling structure is purposely enhanced. The frequency responses by HFSS are also shown in Fig. 4.18 by dashed lines, where the increment on the filter bandwidth is evident. The extracted coupling

coefficients in (4.6) show the increase of the electric coupling coefficient k_E, while the magnetic coupling coefficient k_M stays almost the same.

The filter bandwidths taken at 18 dB return-loss for the three filters are also given in (4.6), which indicate the progressive increment on the filter bandwidths. Therefore, the combination of negative inductive coupling and capacitive coupling will result in the increase of the *net* total coupling, which subsequently will increase the filter bandwidth. This statement can also be accommodated by Eq. (3.64), where the combination of negative k_M and positive k_E will increase the absolute value of the numerator.

Note that the sizes of the conducting patches for the three filter structures in Fig. 4.16 are not changed. But the tap-in position and the width of striplines are necessarily adjusted in order to maintain the same return-loss level.

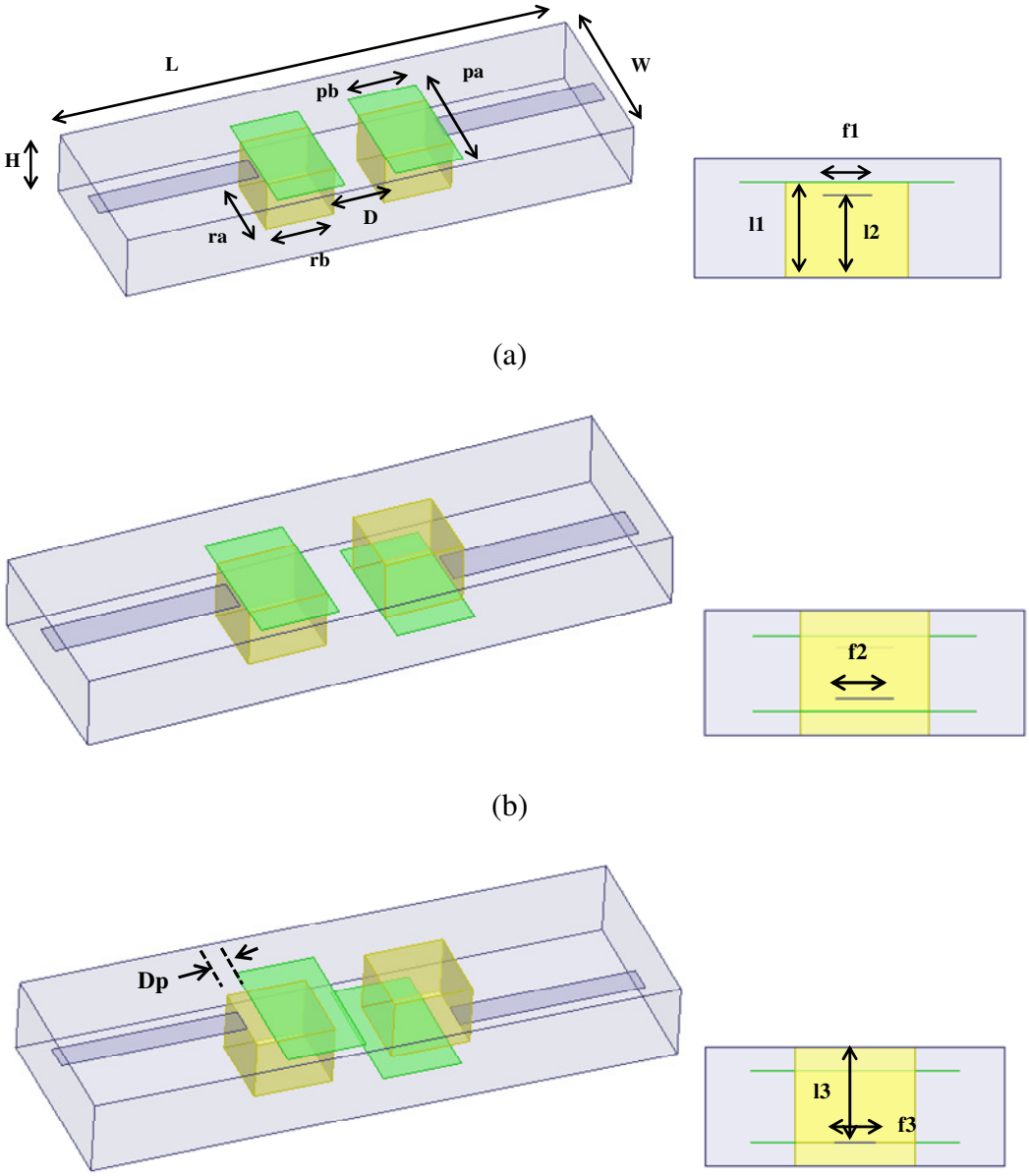

Figure 4.16. 2-pole filter in LTCC: (a) two posts are both shorted at bottom ground plane. (b) The second post is flipped and shorted at the top ground plane. (c) Two patches are shifted. Dimensions in mil: $W = 100$, $L = 300$, $pa = 70$, $pb = 40$, $ra = 40$, $rb = 40$, $H = 39.4$, $l1 = 31.52$, $l2 = 27.58$, $l3 = 31.52$, $f1 = 16$, $f2 = 18$, $f3 = 13.5$, $D = 30$, $Dp = 10$. Dielectric constant = 7.8.

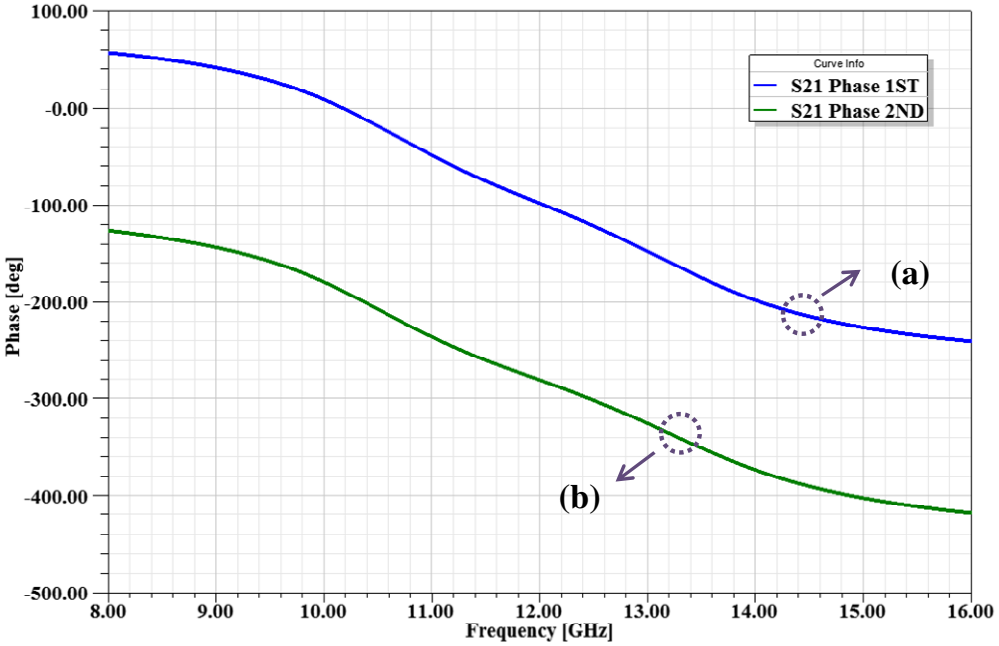

Figure 4.17. The phase of S21 for the filter structures in Fig. 4.16 (a) and (b).

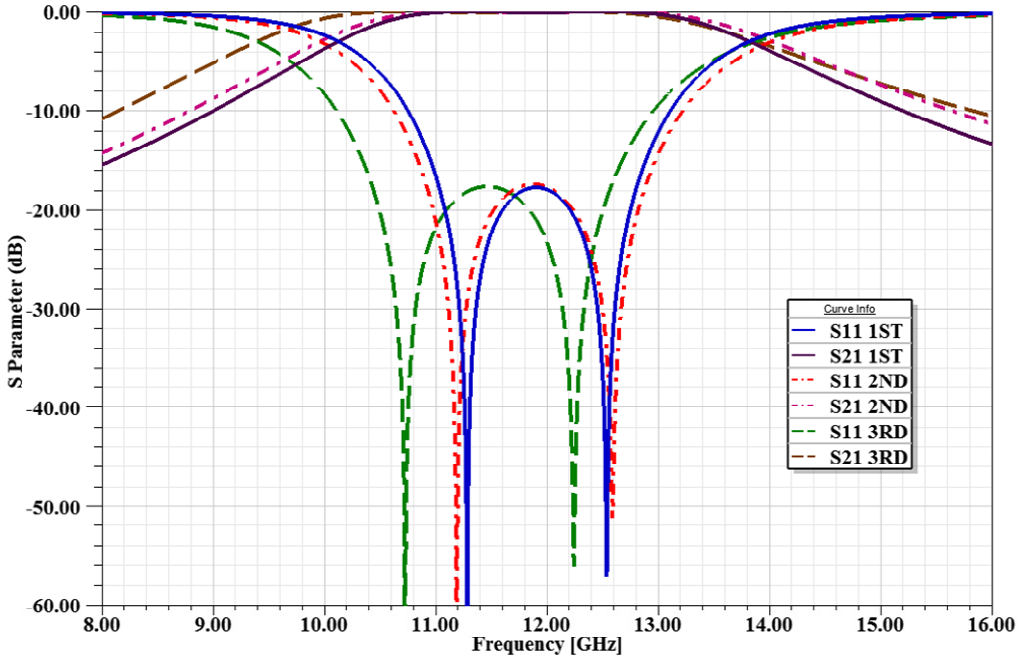

Figure 4.18. The frequency responses of the three filter structures in Fig. 4.16: solid lines for (a), dot-dashed lines for (b), and dashed lines for (c).

4.4.2 Bandwidth Enhancement

Fig. 4.19 (a) shows a 3-pole filter also realized in LTCC, with the first and third posts shorted at the bottom ground plane and the second (center) post alternatively shorted at the top ground plane. The conducting patches of the first and third posts are retreated from the center, avoiding the capacitive coupling with the conducting patch of the center post as much as possible.

In the other two configurations shown in Fig. 4.19 (b) and (c), the conducting patches of the first and third posts are moving inward towards the center by $Dp1$ = 20 mil and $Dp2$ = 30 mil respectively, increasing the overlapping area with the patch of the center post. Note that the sizes of the patches are slightly changed. Therefore, the capacitive coupling realized by the electric fields between conducting patches are subsequently enhanced.

As demonstrated in the previous sub-section, since the center post is grounded at the top, the inductive couplings between the center post and the first and third posts are both negative. If the capacitive couplings within the coupling area are increased, the total *net* coupling k_{12} and k_{23} (also k_B in Eq. 3.64) will be increased as well. Therefore, the filter bandwidth should be also enlarged if the input/output couplings for each case are accordingly adjusted.

The phenomenon of bandwidth enhancement is clearly observed from Fig. 4.20, where the three filter structures in Fig 4.19 are simulated by EM simulator HFSS and the frequency responses are displayed. The filter bandwidths taken at 20-dB return loss for three filters are 1.10, 1.55, and 1.74 GHz respectively.

As stated previously, for this structure, the inductive couplings by magnetic fields surrounding the posts are predominant, which is primarily controlled by the physical distances between the posts. For a wideband microwave filter requiring large couplings, the physical distances between the posts have to be shortened, which sometimes presents significant design challenges. The configuration setup shown in this sub-section introduces a new approach to enlarging the coupling value and increasing the filter bandwidth without physically moving the metallic posts. This approach, realized in LTCC layer stacks gives designers some extra freedom when the filter dimensions are implemented in physical structures.

Again, the widths of the striplines for input/output couplings are necessarily adjusted in order to maintain the same return-loss level. All of the other dimensions are unchanged for the three filters structures, except for the shift of the patches. A disadvantage can also be observed from Fig. 4.20, where the high-side rejection / the slope of insertion loss above filter passband have become worse as the filter bandwidth is increased.

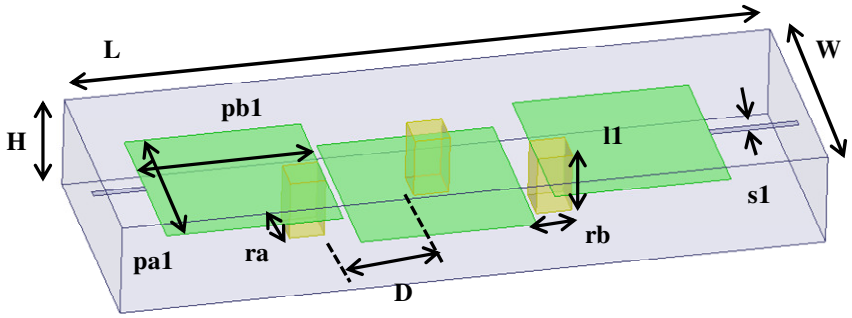

(a)

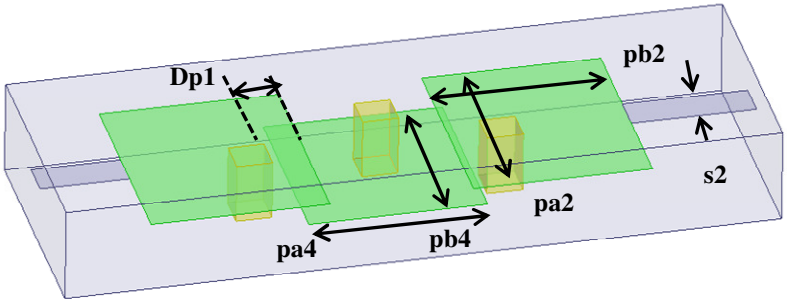

(b)

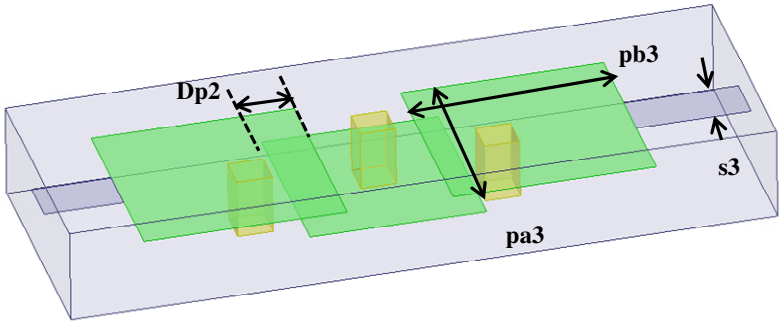

(c)

Figure 4.19. 3-pole filter in LTCC: (a) no overlapping between the conductor patches. (b) The conductor patches are shifted by *Dp1* = 20 mil. (c) The conductor patches are shifted by *Dp2* = 30 mil. Dimensions in mil: *W* = 140, *L* = 400, *ra* = 20, *rb* = 20, *H* = 55.16, *pa1* = 102.7, *pb1* = 100, *pa2* = 120.2, *pb2* = 100, *pa3* = 115.2, *pb3* = 115, *pa4* = 106, *pb4* = 100, *D* = 50, *l1* = 35.46, *s1* = 4.5, *s2* = 21, and *s3* = 28. Dielectric constant = 7.8.

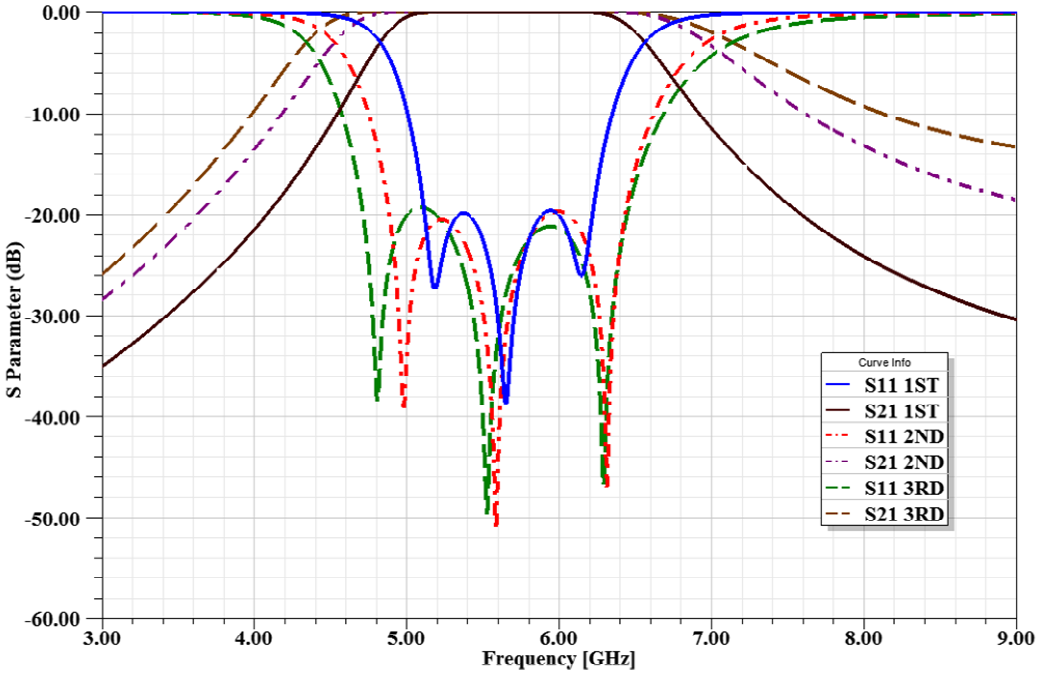

Figure 4.20. The frequency responses of three filter structures in Fig. 4.19: solid lines for (a), dot-dashed lines for (b), and dashed lines for (c).

4.5 INLINE QUASI-ELLIPTIC FILTER WITH COMPOSITE TYPE COUPLINGS

4.5.1 Composite Type Coupling

As discussed in Sec. 3.4, a composite type coupling inverter can provide coupling between two resonators, and also generate a transmission zero, due to the interaction between the inductive and capacitive couplings co-existing in the composite coupling. The realized transmission zero can be solely controlled by the intrinsic resonance of the composite coupling itself without an additional coupling path or other complicated transmission zero generation mechanism.

In this sub-subsection, two realizations of composite type coupling are given. Recall the electric coupling structure in Fig. 4.3, in which the capacitive coupling by electric fields is predominant. As shown in Fig. 4.5 (c), the amount of electric coupling can be controlled by the size of the overlapping area between the inserted floating patch and the patches of the resonators. A conducting wall is placed between the two posts of the resonators, blocking the coupling of magnetic fields. An opening window is made on the conducting wall so that the floating patch can pass through. Also shown in Fig. 4.5 (c), the magnetic coupling as a stray coupling still exists, and can be controlled by the size of the opening window.

Therefore, if the distance between the two posts of the resonators is fixed, the

predominant electric coupling can be adjusted by the size of the overlapping area between the patches, while the weak magnetic coupling can be separately adjusted by the size of the opening window on the conducing wall. A new structure is created in Fig. 4.21 for the composite type coupling. A typical frequency response of the filter structure in Fig. 4.21 by EM simulator HFSS is shown in Fig. 4.22. Since the filter structure can be represented by the equivalent circuit model in Fig. 3.8, the values of circuit elements can be easily extracted from the EM simulation results by even- and odd-excitation:

$$k_E = 0.3163 > k_M = 0.1119 \tag{4.7}$$

where the normalized coupling value k_E (electric coupling) and k_M (magnetic coupling) are derived according to Eq. 4.2. As discussed in Sec. 3.4.4, if the electric coupling is predominant ($k_E > k_M$) in a composite coupling, a transmission zero is generated below the filter passband. A transmission zero at 5.85 GHz below the filter passband is clearly seen in Fig. 4.22.

Recall the magnetic coupling structure in Fig. 4.1, in which the inductive coupling by magnetic fields is predominant. As shown in Fig. 4.5 (a), the amount of magnetic coupling can be controlled by the distance between the metallic posts of the resonators, and the electric coupling as a stray coupling still exists. A small floating patch can be inserted between the conductor patches of the resonators and the top ground plane, which can enhance the electric coupling within the coupling area as shown in Fig. 4.23.

Therefore, a typical frequency response of the filter structure in Fig. 4.23 by the EM simulator HFSS is shown in Fig. 4.24. Again, since the filter structure can be represented by the equivalent circuit model in Fig. 3.8, the values of circuit elements can be easily extracted from the EM simulation results by even- and odd-excitation:

$$k_M = 0.5286 > k_E = 0.2238 \qquad (4.8)$$

Similarly, as discussed in Sec. 3.4.4, if the magnetic coupling is predominant ($k_M > k_E$) in a composite coupling, a transmission zero is generated above the filter passband. A transmission zero at 15.41 GHz above the filter passband is clearly displayed in Fig. 4.24.

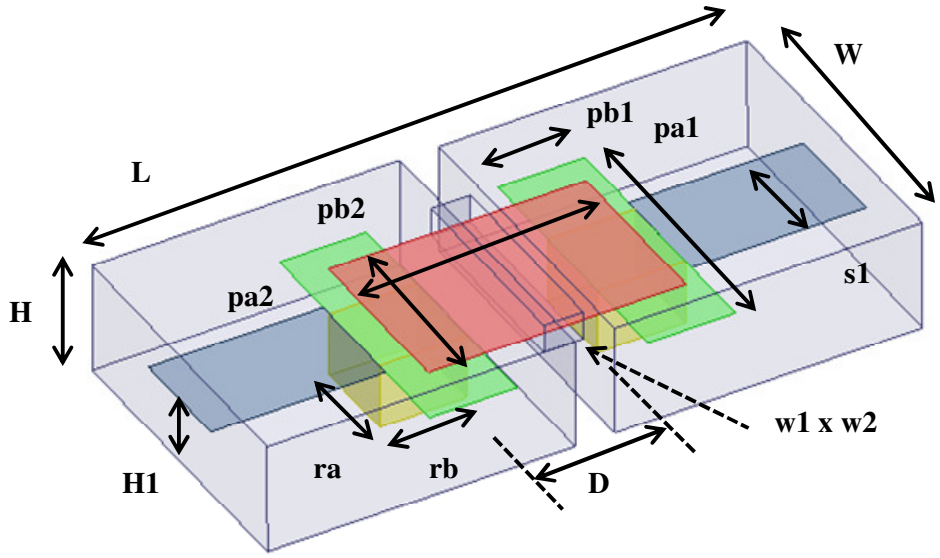

Figure 4.21. Realization of composite type coupling, with strong capacitive coupling and weak inductive coupling. Dimensions in mil: W = 140, L = 300, ra = 40, rb = 40, H = 52.2, $H1$ = 30.6, $pa1$ = 102, $pb1$ = 40, $pa2$ = 80, $pb2$ = 118, D = 60, $s1$ = 50, $w1$ = 90, and $w2$ = 13.5. Dielectric constant = 7.8.

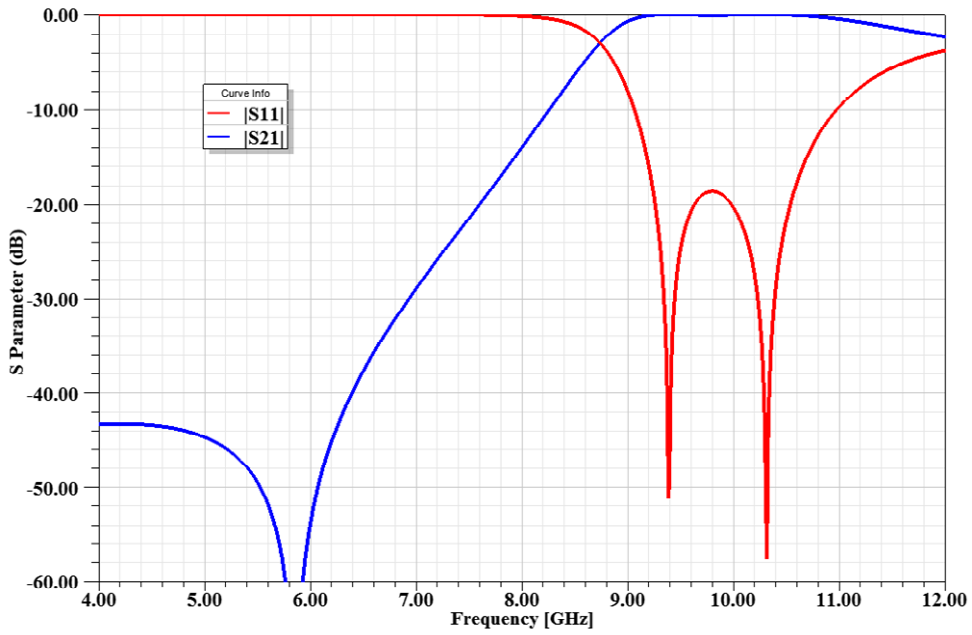

Figure 4.22. Frequency responses of the filter structure in Fig. 4.21.

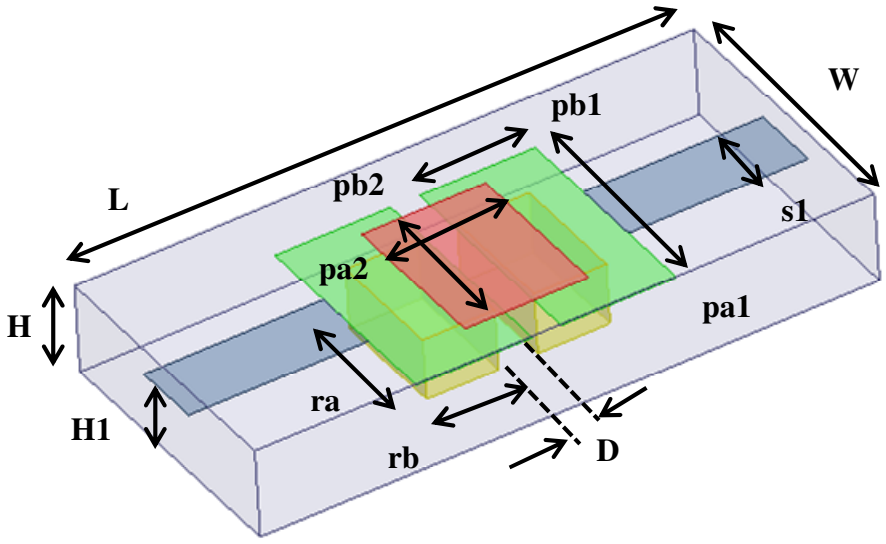

Figure 4.23. Realization of composite type coupling, with strong inductive coupling and weak capacitive coupling. Dimensions in mil: W = 140, L = 300, ra = 60, rb = 35, H = 44.1, $H1$ = 30.6, $pa1$ = 110, $pb1$ = 56, $pa2$ = 80, $pb2$ = 60, D = 19, $s1$ = 35. Dielectric constant = 7.8.

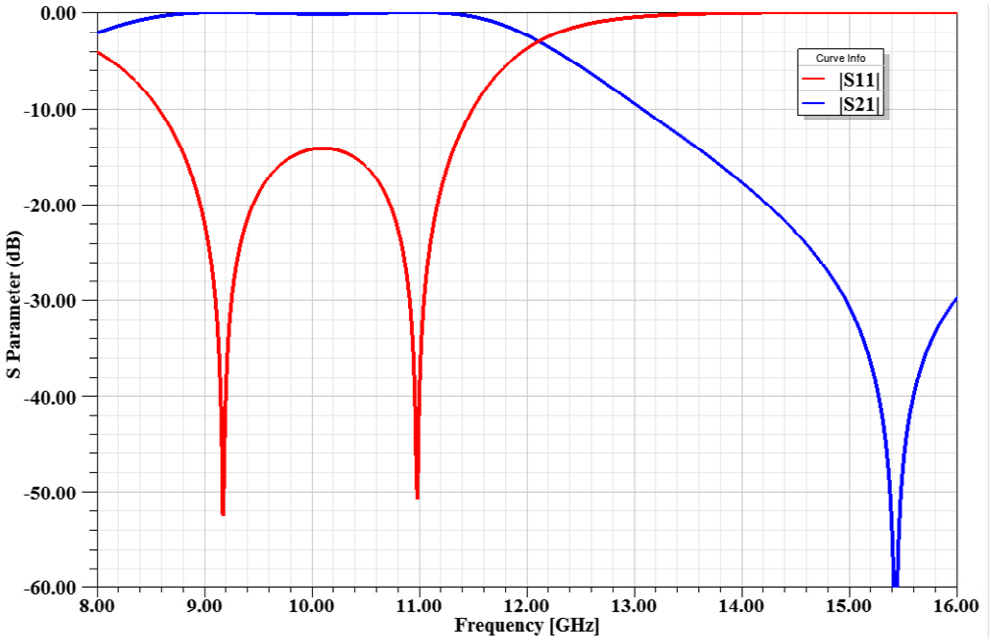

Figure 4.24. Frequency responses of the filter structure in Fig. 4.23.

4.5.2 Inline Quasi-Elliptic Filter

A fourth-degree quasi-elliptic inline filter with two transmissions, one below filter passband and the other above filter passband is designed in this sub-section. The circuit model of this filter is shown in Fig. 4.25. The composite coupling $M_{1,2}$ is responsible for the transmission zero below filter passband, and the realization similar to the filter structure in Fig. 4.21 will be applied. The composite coupling $M_{3,4}$ will generate the transmission zero above filter passband, and the realization similar to the filter structure in Fig. 4.23 will be utilized. A purely inductive coupling $M_{2,3}$ will be used to assemble two structures (two 2-pole filters).

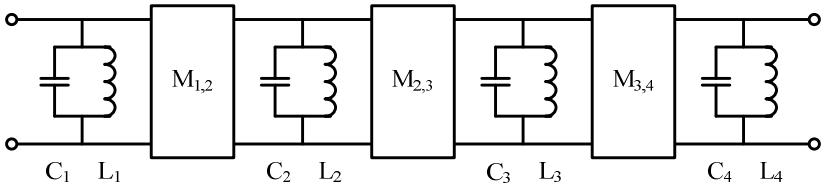

Figure 4.25. Circuit model of fourth-degree inline quasi-elliptic filter with composite type couplings.

The inline filter with center frequency = 10 GHz, bandwidth = 2.9 GHz, and return-loss level at 21 dB is firstly synthesized using the cascade synthesis technique introduced in Section 3.3, according to the circuit topology described in Fig. 4.25. The synthesized values of the circuit elements are

$$f_1 = 9.2168, f_2 = 9.6460, f_3 = 10.5804, f_4 = 10.7863$$

$$k_{M,1} = 0.1186, k_{M,2} = 0.1900, k_{M,3} = 0.4746$$

$$k_{E,1} = 0.3991, k_{E,2} = 0, k_{E,3} = 0.2077$$

$$Q_{e,1} = 3.3329, Q_{e,2} = 3.5216 \qquad (4.9)$$

where the normalization in (4.1) are used.

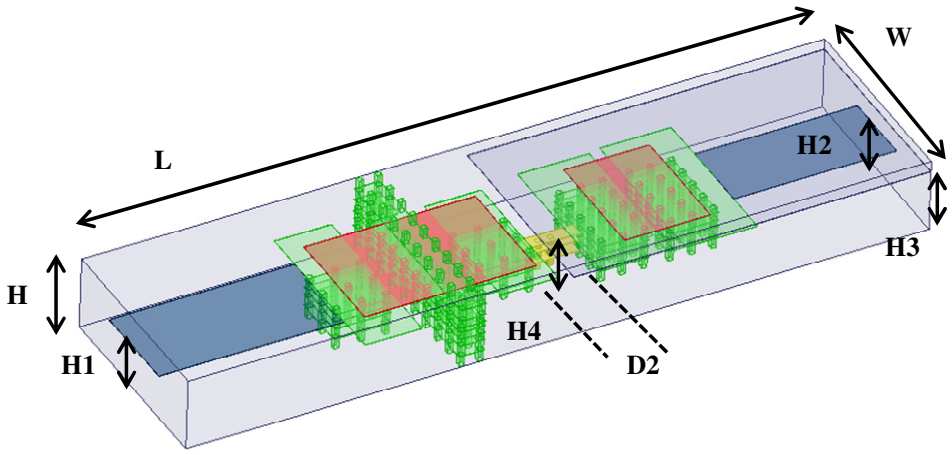

Figure 4.26. Realization of fourth-degree inline filter in HFSS with via model. Dimensions in mil: *W* = 140, *L* = 520, *H* = 52.2, *H1* = 30.6, *H2* = 30.6, *H3*= 44.1, *H4* = 21.6, *D2* = 40.06. Dielectric constant = 7.8.

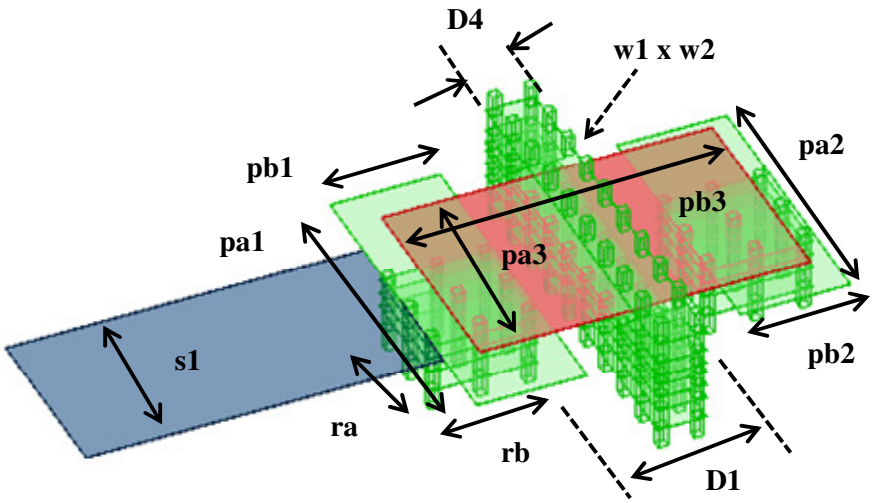

Figure 4.27. Realization of the first and second resonators in Fig. 4.26. Dimensions in mil: *ra* = 40, *rb* = 40, *pa1* = 119.35, *pb1* = 40, *pa2* = 100.78, *pb2* = 40, *pa3* = 80, *pb3* = 120.11, *D1* = 60, *D4* = 18, *s1* = 65.36, *w1* = 90, *w2* = 13.5. Dielectric constant = 7.8.

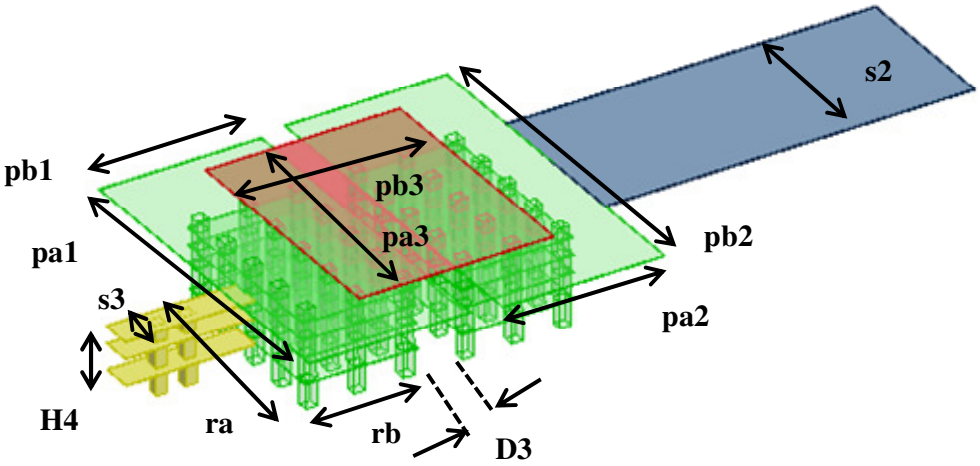

Figure 4.28. Realization of the third and fourth resonators in Fig. 4.26. Dimensions in mil: *ra* = 60, *rb* = 35, *pa1* = 109.01, *pb1* = 50, *pa2* = 113.34, *pb2* = 50, *pa3* = 80, *pb3* = 60, *D3* = 13.47, *s2* = 51.63, *s3* = 10. Dielectric constant = 7.8.

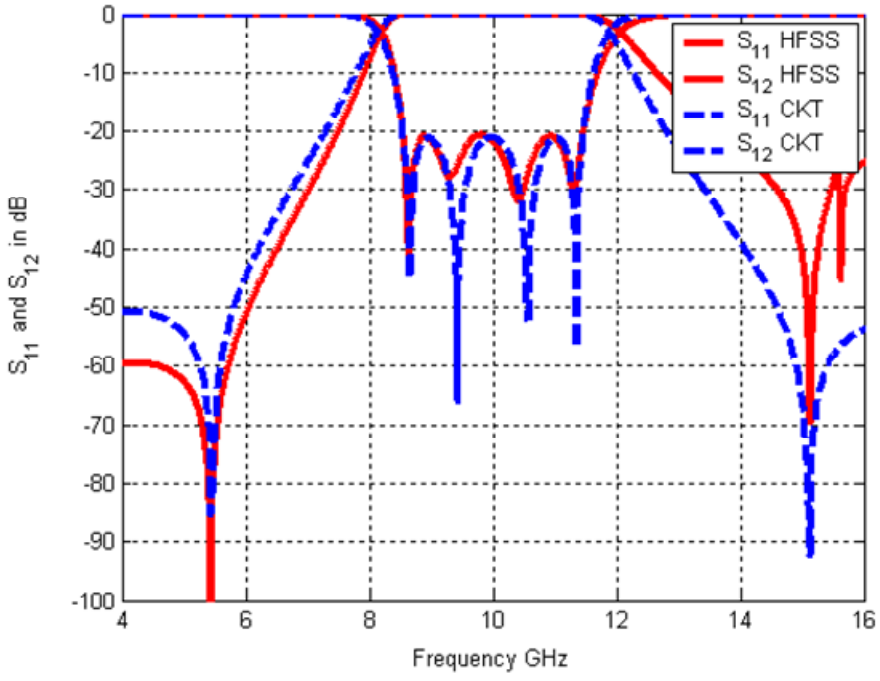

Figure 4.29. Frequency responses of fourth-degree inline filter from the HFSS model and from the circuit model.

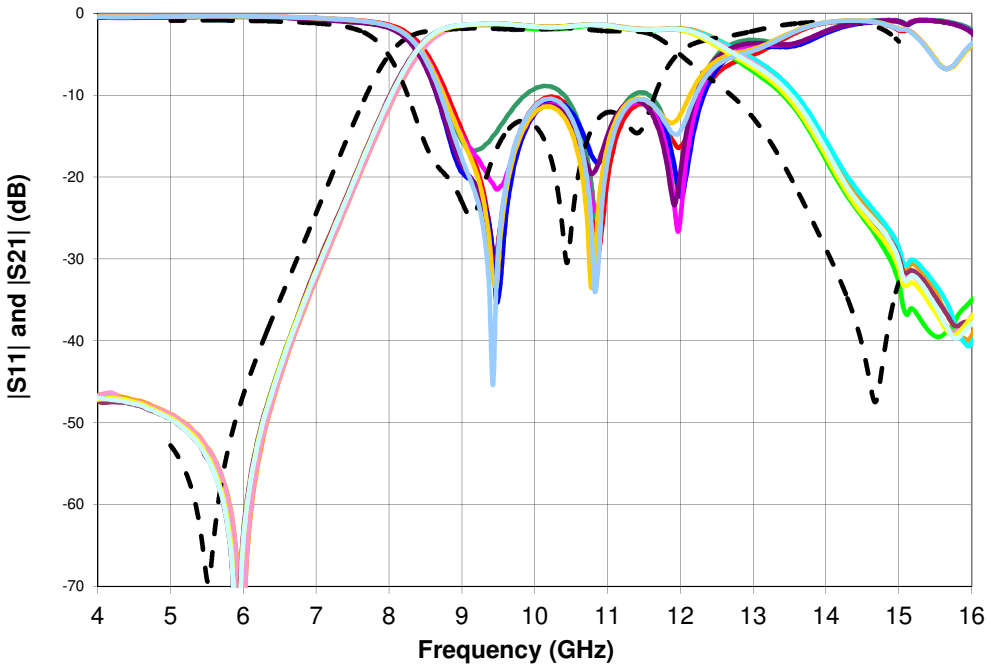

(a)

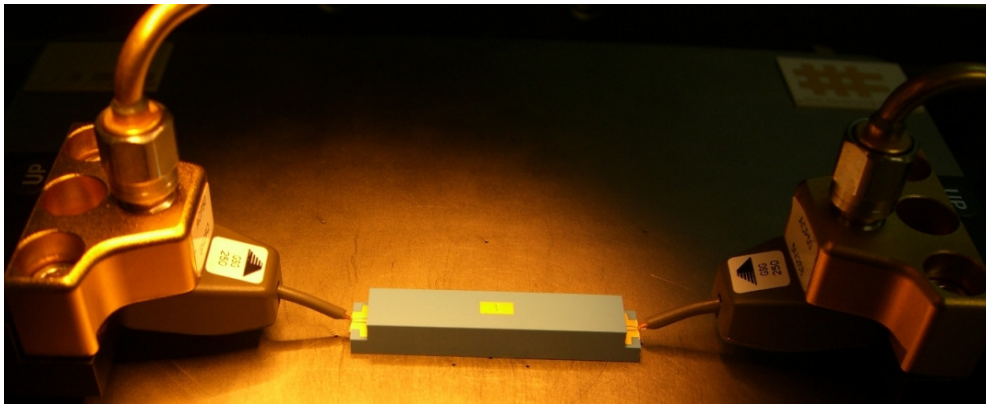

(b)

Figure 4.30. (a) Frequency responses of fourth-degree inline filter: the dashed lines are from HFSS simulation of the entire filter model with stripline transitions and launches; all other solid lines are from measurements of different fabricated filters. (b) Fabricated filter example in measurement.

From the synthesized values in (4.9), the resonant frequencies of the first and second resonator (f_1 and f_2) are very close in value. Therefore, for initial design, f_1, $k_{M,1}$, $k_{E,1}$, and $Q_{e,1}$ are implemented by the structure in Fig. 4.21. Similarly, since f_3 and f_4 are very close in value, f_4, $k_{M,3}$, $k_{E,3}$, and $Q_{e,2}$ are implemented by the structure in Fig. 4.23 to find the initial dimensions.

Then the fourth-order inline filter is assembled from two small structures as shown in Fig. 4.26. Variant schemes for cascading modular blocks to build a high order filter have been available [61]-[64]. But the filter responses quickly deteriorate upon cascading the modular blocks. For the filter structure in Fig. 4.26, a small ridge is used to connect the resonator post 2 and 3. The design of this small ridge follows similar design method used to design ridge waveguide filter in Section 4.3.

Upon the completion of building up the entire physical model, the optimization by EM simulator HFSS is used to explore the optimum solution, which will maintain the bandwidth and the locations of transmission zeros. The model in Fig. 4.26 has been implemented in half version of via model, where the solid 3D objects are replaced by rows of via and the metallization plates in each LTCC stack layer as those shown in Fig. 1.1. The enclosure remains as solid wall so that the simulation time of the entire model on a computer is adequate to run optimization.

The final EM simulation results from HFSS as well as the frequency responses from

the circuit model are superimposed in Fig. 4.29. They are almost identical, which validates the synthesis technique and the design approach.

Since the characteristic impedances of the input/output microstrip lines are not 50 Ohm, simple stripline transitions are added, which run from the existing lines tapped-in the first and forth resonators to 50 Ohm lines. Also, the launches are added at the end of 50 Ohm lines in order to take measurement by probe station. The final EM simulation of the entire filter structure in full version of via model with stripline transitions and launches are plotted in Fig. 4.30. The filter is fabricated by LTCC technology and the measurement is taken from 7 pieces of fabricated filters. The frequency responses of all measurement are also shown in Fig. 4.30.

The measured results in Fig. 4.30 are very consistent among 7 pieces of fabricated devices, except that there is about 500 MHz shift from the simulated results. The same filter bandwidths from measured results are maintained, and the two transmission zeros, one below filter passband and the other above filter passband are clearly observed.

Chapter 5 Microwave Wideband Transition Designs

5.1 INTRODUCTION

Transitions between various microwave components are important elements in wideband communication systems. The transition, in most cases acting as transmission lines is capable of connecting components in substrate or on board, transforming impedance levels between different elements, and directly realizing passive components with certain functionality, such as power dividing, phase shifting, and so on [65]-[68].

The challenge of realizing a transition is that, quite often the transition requires customized designs to fit within specific area and stringent requirements, for instance, very wide operating bandwidth, large difference in impedance levels, tight spacing and restricted area, limitation from physical implementation, and so on. The design novelty of the transition can also help alleviate the increased performance demand on other components, to which the transition is connected.

Because of the layered stack structure in LTCC technology, a microwave stripline structure implemented by metallization traces between ceramic layers is naturally a good candidate for a transmission line. Therefore, in this Chapter, novel transition

structures in LTCC are introduced to cope with variant stringent requirements.

5.2 COAXIAL TO STRIPLINE TRANSITION INTEGRATED WITH LOWPASS FILTER

In this section, a transition, which can provide dual functionality, transforming the impedance level between two connectors and acting as a filtering structure is introduced with detailed design procedures. Several transitions with dual or multiple functionality have been addressed [69]-[70], and all of them require additional design effort due to the increased complexity.

As shown in Fig. 5.1 (a), the original proposed design consists of a coaxial connector, a coaxial to stripline transition, a bandpss filter, and a co-planar waveguide launcher. The physical structure models of the coaxial connector and the launcher are fixed without modification. The coaxial to stripline transition and the bandpass filter are separately designed to satisfy individual requirements.

The stripline transition from coaxial connector should provide 50 Ohm impedance level over the frequency band of interest. The filter passband is specified from 10.8 to 14.1 GHz, which has center frequency f_0 = 12.34 GHz and bandwidth BW = 3.3 GHz (relative BW = 26.75%). It also requires minimum 50 dB rejection at only the filter upper stopband from 22.6 to 27.2 GHz.

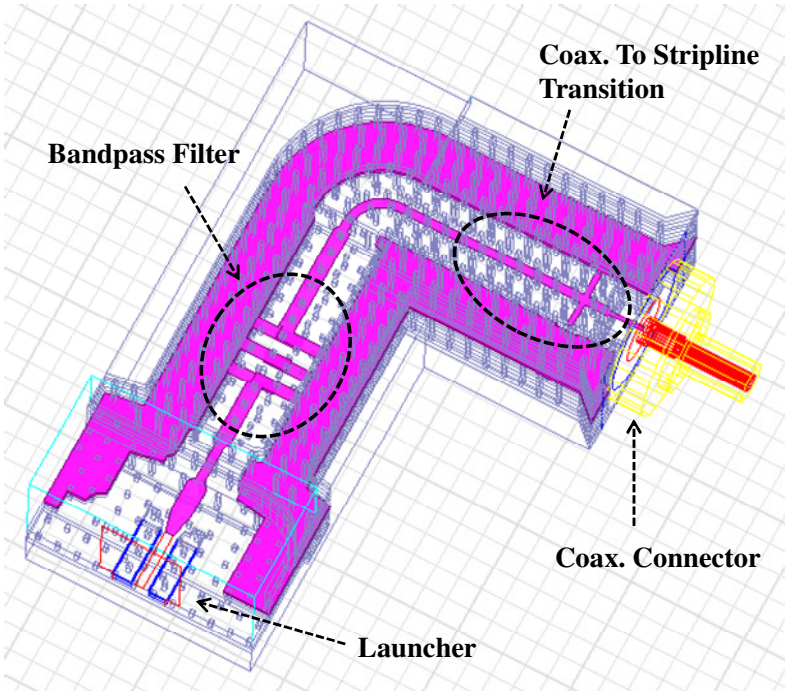

(a)

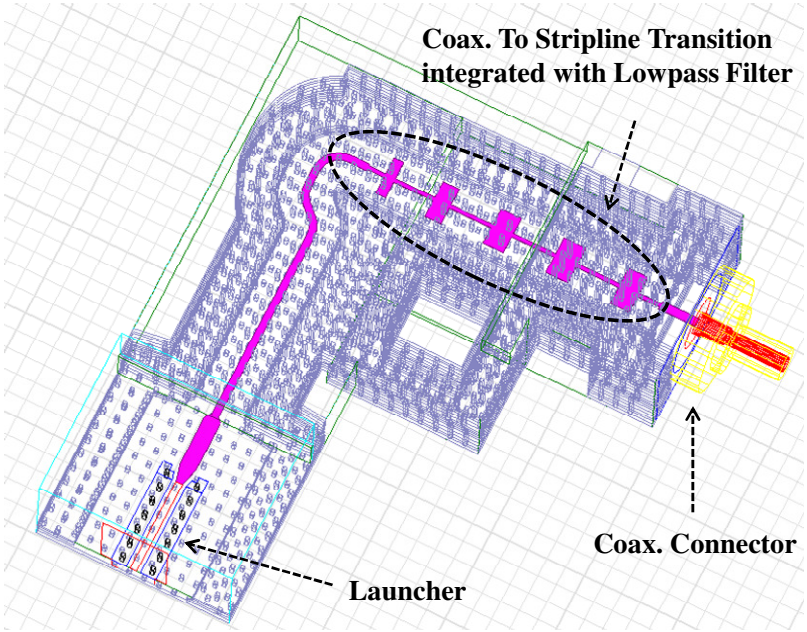

(b)

Figure 5.1. (a) Original design, there are two components: a coaxial to stripline transition and a bandpass filter. (b) New design with only one component: a coaxial to stripline transition integrated with a lowpass filter.

Since there is no rejection requirement in the filter's lower stopband, the specifications can also possibly be realized by a lowpass filter, with the cut-off frequency of the lowpass filter properly located between the upper edge of the passband 14.1 GHz and the lower bound of the rejection 22.6 GHz. Moreover, this lowpass filter can be implemented by alternative high- and low-impedance stripline structures, which is by nature altering the impedance levels. Therefore, it is possible to design an alternative high- and low-impedance stripline structure, acting as both a lowpass filter and a transition from a coaxial connector.

As shown in Fig. 5.1 (b), the new proposed configuration contains only one component between the coaxial connector and the launcher. The design of the coaxial to stripline transition integrated with lowpass filtering function is proposed and will be covered in details with design steps.

The design of a lowpass filter is first carried out, which is straightforward following the procedures given in [20]. Fig. 5.2 shows an *n*th-degree lowpass filter prototype (for this case, n is an odd number). The design parameters g_i for an 11th-degree lowpass filter prototype with 0.01 dB in-band ripple level are listed in Table 5.1. Moreover, $g_0 = 1$ and $g_{12} = 1$ are normalized impedances of the source and load, respectively. The series inductor is going to be realized by a high-impedance stripline, while the shunt capacitor is implemented by a low-impedance stripline. Note that the design parameters g_i are symmetric.

In LTCC technology, the nominal value of dielectric constant is usually pre-determined, and the maximum number of layers, namely the total thickness or height of substrate is also limited. Therefore, for the implementation of stripline in LTCC technology, the realizable characteristic impedance of stripline is restricted, especially for the highest possible characteristic impedance value. Usually, the minimum width of a metallization trace from the standard process is capable of 3 to 4 mil. As shown in Fig. 5.3, the characteristic impedance of a stripline with width wl = 3 mil is 73.7 Ohm, which is taken as high impedance line, Z_{oH} = 73.7 Ohm. Similarly, the characteristic impedance of a stripline with width wl = 35 mil (though this width can be further increased) is 21.7 Ohm, which is treated as a low impedance line, Z_{oL} = 21.7 Ohm.

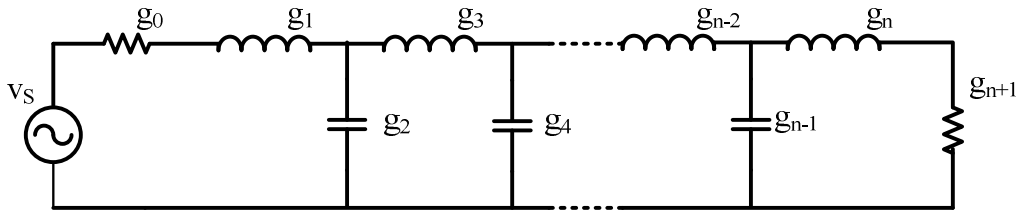

Figure 5.2. Lowpass filter prototype. (n is odd)

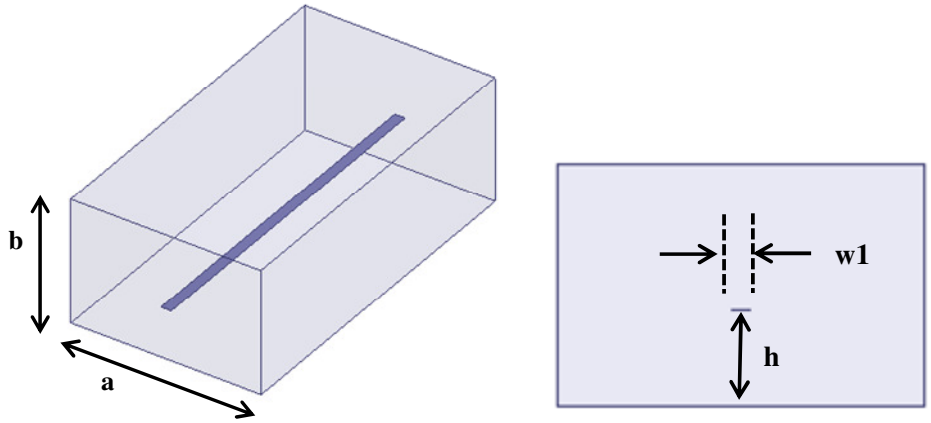

Figure 5.3. Realization of stripline in LTCC. (Dimension in mil): a = 55, b = 36, h = 14.4, $w1$ = 3. (Dielectric constant = 7.8).

The normalized design parameters g_i in Table 5.1 are given in a lowpass prototype with normalized angular cut-off frequency $\omega'_0 = 1$ and normalized characteristic impedance $R'_0 = 1$. Therefore, the de-normalized values of L_i (from series g_i) and C_i (from shunt g_i) can be derived from

$$L_i = \frac{R_0}{R'_0}\frac{\omega'_0}{\omega_0} g_i \qquad (5.1a)$$

$$C_i = \frac{R'_0}{R_0}\frac{\omega'_0}{\omega_0} g_i \qquad (5.1b)$$

where ω_0 is the de-normalized angular cut-off frequency, which is chosen at 16.25 GHz for this design, and R_0 is the de-normalized characteristic impedance, typically equal to 50 Ohm. The evaluated values of L_i and C_i from (5.1) are also listed in Table 5.1.

For the realization of L_i by high-impedance stripline, the length of stripline can be

found from

$$sl_{Li} = \frac{v}{\omega_c}\sin^{-1}\left(\frac{\omega_c L_i}{Z_{oH}}\right) \cong \frac{vL_i}{Z_{oH}} \tag{5.2}$$

As mentioned, the realizable maximum impedance of stripline in LTCC technology is restricted, which has been chosen as 3 mil width stripline or the characteristic impedance Z_{oH} = 73.7 Ohm. Therefore, the function $\sin^{-1}$ may be invalid for some evaluated values of L_i, since the function $\sin^{-1}$ has the evaluated value not greater than one. The approximation in (5.2) is then taken as a temporary solution.

Similarly, for the realization of C_i by low-impedance stripline, the length of stripline can be derived from

$$sl_{Ci} = \frac{v}{\omega_c}\sin^{-1}(\omega_c C_i Z_{oL}) \cong vC_i Z_{oL} \tag{5.3}$$

As shown in Table 5.1, the evaluated values of the function $\sin^{-1}$ in (5.3) are very small, so another approximation is taken to derive the stripline length as well. The evaluated lengths of striplines from (5.2) and (5.3) are listed in Table 5.1 under the column *Length1*. The discontinuity between the high-impedance and low-impedance lines is neglected, but is taken into account in the EM simulations.

After obtaining the initial design parameters calculated from design formulas, the physical structure model of the lowpass filter is realized in EM simulator HFSS as shown in Fig. 5.4 (b). The frequency responses are also given in Fig. 5.4 (a) shown as solid lines. With the approximations made in (5.2) and (5.3), the performance of the lowpass filter is not significantly deteriorated, though the cut-off frequency is noticeably shifted downward to 13.5 GHz.

Table 5.1. Design Table for Lowpass Filter

	g_i	*Li*	*Ci*	*Length1*	*Length2*	*Length3*
1	0.8234	0.4032		23.14	23.81	23.45
2	1.4442		0.2829	25.96	15.11	20.60
3	1.8298	0.8961		51.42	43.03	45.57
4	1.7437		0.3416	31.35	23.97	23.73
5	1.9554	0.9576		54.95	44.06	45.56
6	1.7856		0.3498	32.10	25.70	21.84
7	1.9554	0.9576		54.95	44.06	45.04
8	1.7437		0.3416	31.36	23.97	17.43
9	1.8298	0.8961		51.42	43.03	42.22
10	1.4442		0.2829	25.96	15.11	10.43
11	0.8234	0.4032		23.14	23.81	18.20

Note: *Li* in nH, *Ci* in pF, *Length1* (in mil) is the calculated stripline length for LPF from formulas, *Length2* (in mil) is the optimized stripline length for LPF only, *length3* (in mil) is the optimized stripline length for LPF together with transition.

To restore the performance of the lowpass filter, the length of the stripline is first scaled by a factor 13.5/16.25, and then optimized by the optimization routine in HFSS. Note that the symmetry of the structure is still preserved, and only sl_i, i = 1, 2, ..., 6 are included as optimized variables. The frequency responses evaluated from the optimized parameters are also given in Fig. 5.4 (a) shown as dash-dotted lines, where the horizontal bars are the limits of the filter specification, clearly satisfied by dash-dotted lines. The lengths of striplines after optimization are also listed in Table 5.1 under the column *Length2*.

The physical model of the coaxial connector in HFSS is shown in Fig. 5.5 (b) with its frequency responses shown in Fig. 5.5 (a) as dash-dotted lines, which clearly displays that the performance of the coaxial connector to a 50 Ohm stripline is out of specification. After the design of the lowpass filter is well accomplished, the lowpass filter will be directly attached to the coaxial connector, and the physical model of the entire transition is depicted in Fig. 5.5 (c).

A two-step optimization strategy is used to obtain the optimum dimensions. First, the symmetry of the lowpass filter is again preserved, and only sl_i, i = 1, 2, ..., 6 are included as optimized variables. All remaining dimensions are untouched. Second, based on the optimized results from the first step, all lengths of striplines, sl_i, i = 1, 2, ..., 11 are chosen as optimized variables without symmetry enforced. All of the optimization is carried out in HFSS.

The frequency responses of the coaxial to stripline transition integrated with lowpass filter are shown in Fig. 5.5 (a) as solid lines, after using optimization to obtain the optimum dimensions of the stripline lengths. For obtaining the frequency responses in HFSS, one wave port is set at the open end of the coaxial connector, and the other wave port is set at the 50 Ohm stripline end. The lengths of striplines after final optimization are listed in Table 5.1 under the column *Length3*.

The frequency responses in Fig. 5.5 (a) clearly indicate the effectiveness of combining the impedance level transforming and the lowpass filtering function, and

the successfulness of obtaining the final design parameters by described optimization strategy. The filter specifications illustrated by horizontal bars are well satisfied. The complete design in via model ready for LTCC manufacturing process has already been shown in Fig. 5.1 (b), where the coaxial to stripline transition integrated with lowpass filter has been highlighted. Note that the transition is also bent to fit into a tight space.

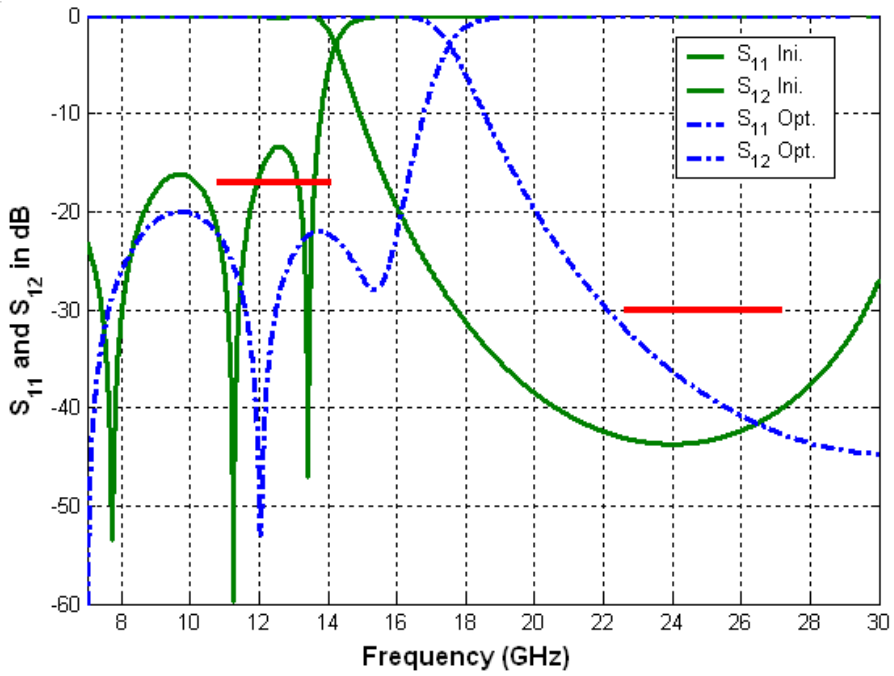

(a)

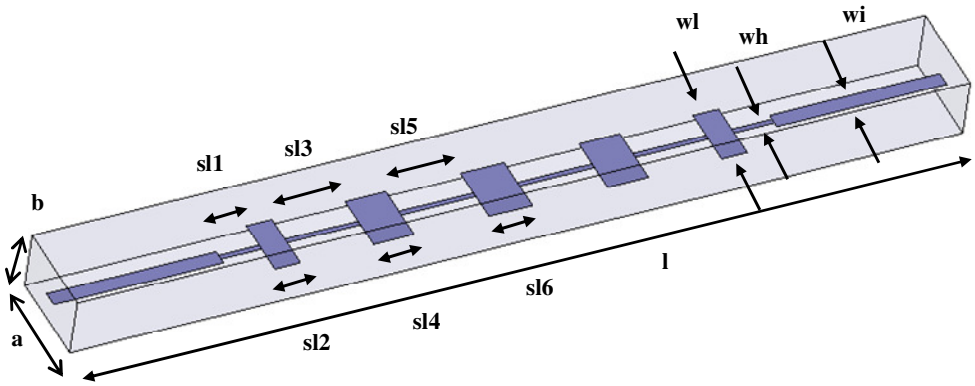

(b)

Figure 5.4. Realization of lowpass filter in LTCC, (a) frequency responses from initial design parameters (calculated from formulas) and optimized parameters, (b) physical model in HFSS. (Dimension in mil), *sl1-sl6* refers to Table 5.1, a = 55, b = 36, wi = 9, wh = 3, wl = 35. (Dielectric constant = 7.8).

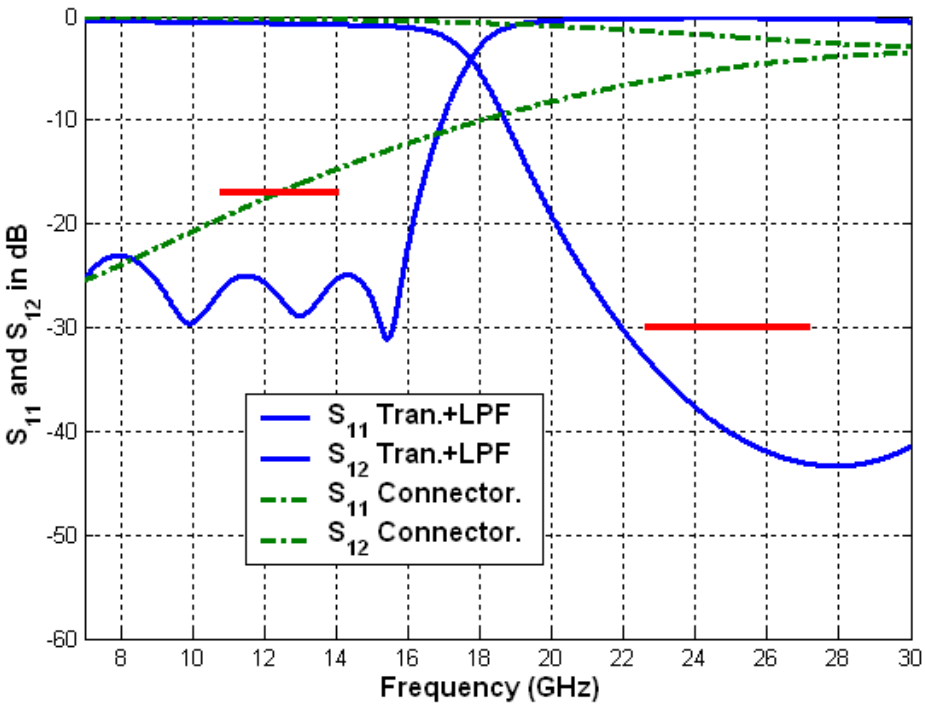
0
-10
-20
-30
-40
-50
-60
8
10
12
14
16
18
20
22
24
26
28
30
S11 and S12 in dB
Frequency (GHz)
S11 Tran.+LPF
S12 Tran.+LPF
S11 Connector.
S12 Connector.

(a)

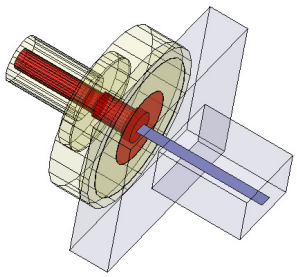

(b)

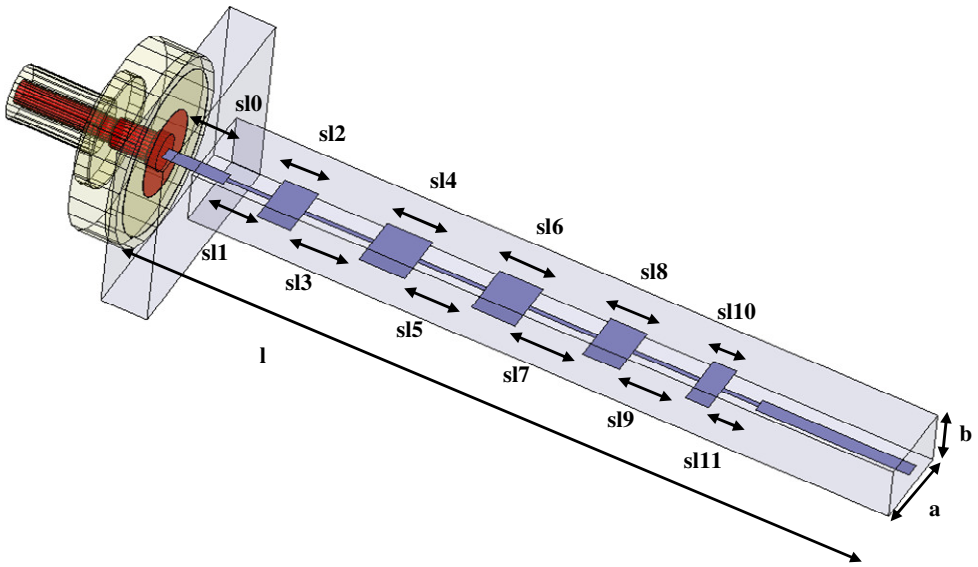

(c)

Figure 5.5. Realization of coaxial to stripline transition integrated with lowpass filter in LTCC, (a) frequency responses from coaxial connector and final optimized design parameters, (b) physical model of coaxial connector to one stripline section, and (c) physical model of entire transition design in HFSS. (Dimension in mil), *sl1-sl11* refers to Table 5.1, the width of lines is the same as that in Fig. 5.4, a = 55, b = 36, *sl0* = 40, l = 454. (Dielectric constant = 7.8).

5.3 WIDEBAND COAXIAL TO STRIPLINE TRANSITION COVERING 14-50 GHZ

In this section, another coaxial connector to stripline transition is introduced. For this transition, there is no more specification on out-of-band rejection, but it requires a -20 dB return-loss level over an extremely wide frequency range, from 14 to 50 GHz.

Following a similar approach introduced in last section, a 7th-degree lowpass filter with cut-off frequency f_c = 55 GHz and 0.01 dB in-band ripple level is first designed and realized in LTCC technology. The design procedures are exactly the same as those given in last section, which therefore are omitted in this section.

The physical structure of the coaxial connector alone is shown in Fig. 5.6, and the frequency responses simulated in EM simulator HFSS are given in Fig. 5.8 as dash-dotted lines, which clearly show the poor performance. Then the lowpass filter will be directly attached to the coaxial connector, where the synthesized and designed dimensions of the lowpass filter will be served as initial parameter values for the stripline structure of the transition. The realization of coaxial to stripline transition is shown in Fig. 5.7, in which the entire transition consists of seven sections of alternative high- and low-impedance striplines with one additional 50 Ohm stripline at the end.

Adopting a similar optimization strategy dividing with steps, first, all lengths of striplines will be used as optimized variables, and all remaining dimensions are untouched. In the next step, based on the optimization results from the first step, all widths of striplines will also be chosen as optimized variables in addition to already optimized lengths of striplines. The same optimization routine will be repeated. Moreover, the dimensions of the housing of striplines are also possibly included as optimized variables in the following step. All of the optimization is carried out in HFSS.

The optimized lengths and widths of the striplines are given as the following:

$$l_i: \{11.99, 8.42, 13.52, 4.97, 9.36, 3.50, 6.59\}$$

$$w_i: \{4.79, 25.26, 4.90, 21.91, 1.98, 17.75, 5.82\}$$

$$i = 1, 2, ..., 7 \qquad (5.4)$$

The total length of the transition is 58.33 mil only. The frequency responses of the complete coaxial to stripline transition with the optimized parameter values are shown in Fig. 5.8 as solid lines, where the -20 dB return-loss requirement over 14 to 50 GHz illustrated by horizontal bar is clearly satisfied.

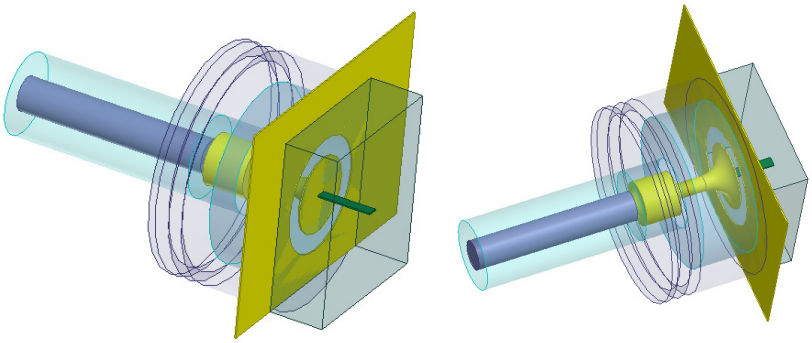

Figure 5.6. Physical structure of coaxial connector with one stripline section.

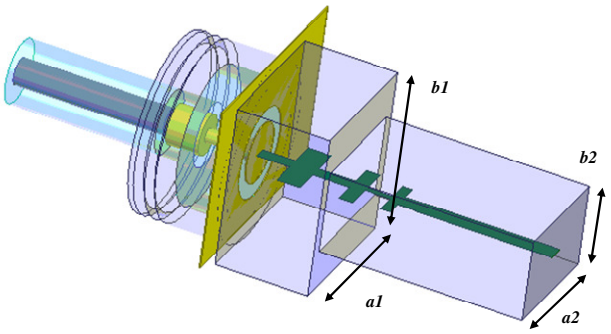

(a)

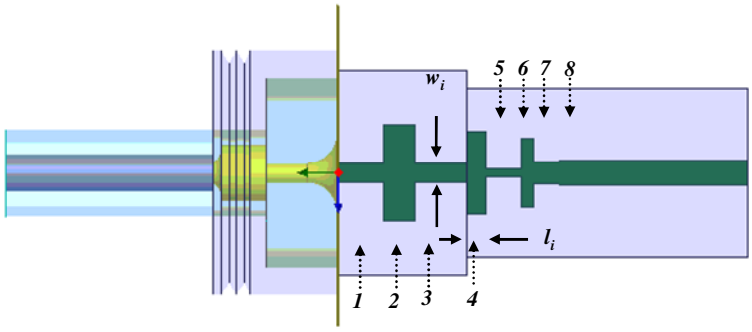

(b)

Figure 5.7. Realization of coaxial to stripline transition. (Dimensions in mil): *a1* = 54.2, *b1* = 60, *a2* = 45, *b2* = 30, *w8* = 6.5, and other dimensions are given in (5.4). (Dielectric constant = 8.8).

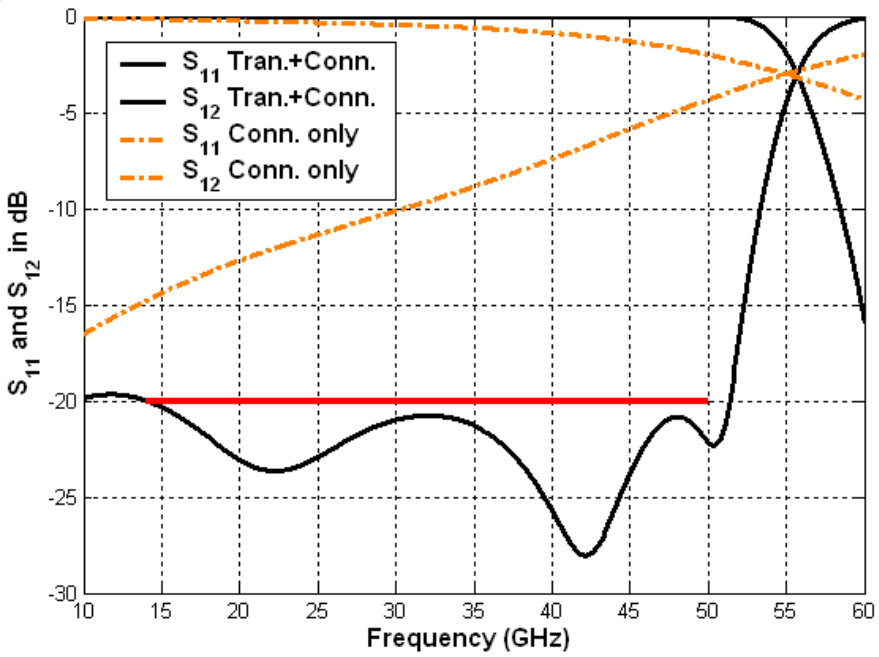

Figure 5.8. Frequency responses of coaxial to stripline transition.

5.4 LTCC SUBSTRATE TO AIR-FILLED WAVEGUIDE TRANSITION

In this section, a LTCC substrate waveguide to air-filled hollow waveguide transition is presented. The physical model of this transition in EM simulator HFSS is shown in Fig. 5.9 (a). The dimensions of the LTCC waveguide are predetermined as *a1* = 95 and *b1* = 50 (in mil). The air-filled waveguide is a standard WR-28 waveguide, *a2* = 280 and *b2* = 140 (in mil). The operating frequency range of this transition is specified from 28 to 32 GHz.

A connected four-step physical structure realized by LTCC substrate shown in Fig. 5.9 (b) is inserted into air-filled waveguide in Fig. 5.9 (a), which looks like a cascaded ridge waveguide structure from multiple cross sections, except that the ridges are made of LTCC substrate instead of metal material. By utilizing this stepped structure, the characteristic impedance of LTCC substrate waveguide can be gradually transformed to the characteristic impedance of air-filled waveguide over the frequency range of interest.

The LTCC substrate used for this project has dielectric constant = 8.8, and the layer thickness is set to 5 mil. Therefore, the thickness of the steps t_i in the structure in Fig. 5.9 (b) must be a multiplication of 5 mil. Moreover, the height of air-filled waveguide for the steps h_i is trimmed to ease the gradual change of the cross-section dimensions and give better impedance level matching between adjacent steps. Note that the

height h_i is also pre-selected.

$$t_i \text{ (in mil): } \{40, 30, 20, 10\},\ i = 1, 2, 3, 4$$
$$h_i \text{ (in mil): } \{60, 80, 100, 120\} \tag{5.5}$$

There are in total four steps. Then the width w_i and the length l_i of all four steps (except w_1) are chosen as optimized variables, and the entire structure is directly optimized in HFSS. The optimized parameter values are

$$w_i \text{ (in mil): } \{95, 92.3, 52.4, 40.1\},\ i = 1, 2, 3, 4$$
$$l_i \text{ (in mil): } \{49.6, 34.8, 130.9, 185.4\} \tag{5.6}$$

The frequency responses of the entire LTCC substrate to air-filled waveguide transition are displayed in Fig. 5.10, where the in-band return-loss level over 28 to 32 GHz is well below -25 dB.

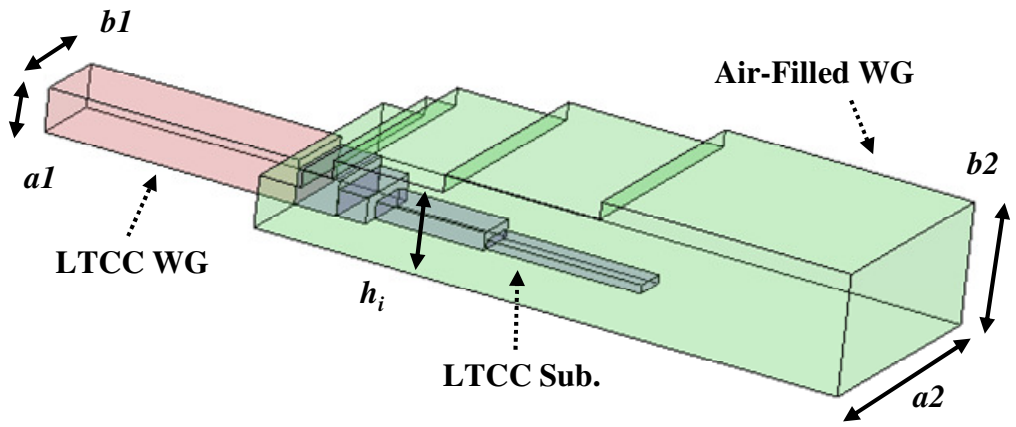

(a)

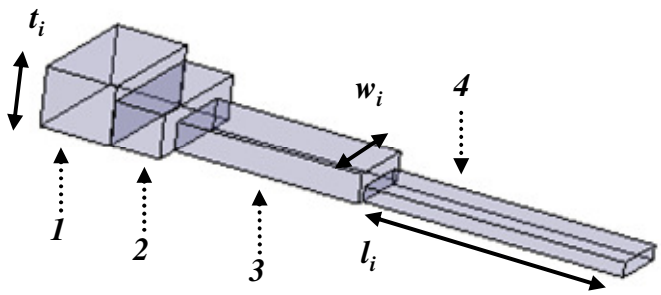

(b)

Figure 5.9. Realization of LTCC substrate to air-filled waveguide transition in LTCC. (Dielectric constant = 8.8).

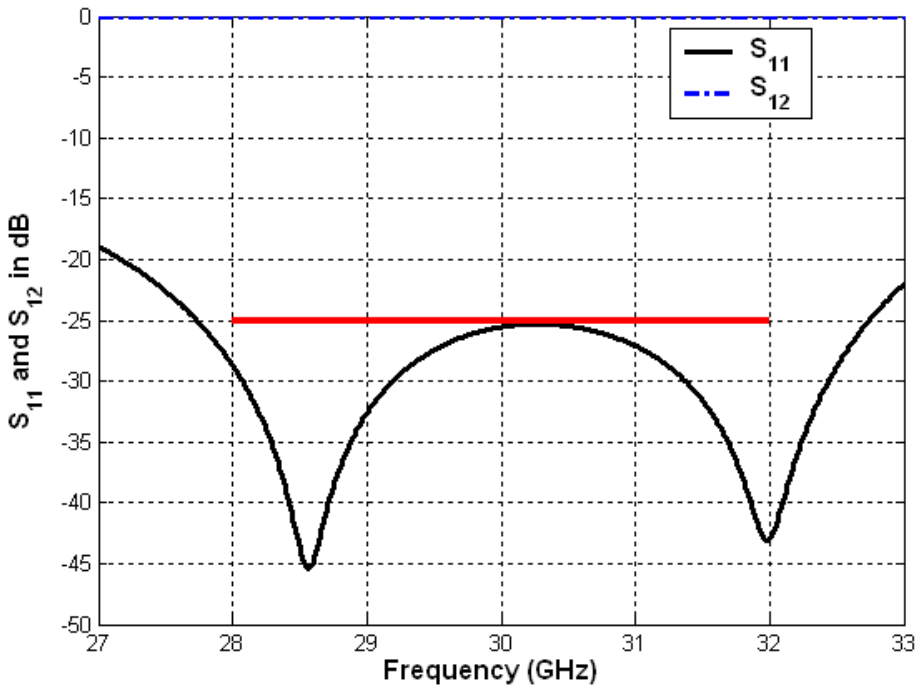

Figure 5.10. Frequency responses of LTCC substrate to air-filled waveguide transition.

Chapter 6 Conclusions and Future Research

6.1 CONCLUSIONS

The work presented in this dissertation has explored the synthesis and design of wideband microwave filters and other components.

The synthesis techniques of wideband multi-coupled resonators filters represented by coupling matrix have been successfully developed in Chapter Two. Based on similar approaches for the narrowband case, both the approximation problem and the synthesis problem for wideband applications have been extended and solved in the bandpass domain to cover a very wide frequency range. Three types of frequency dependent couplings are used to replace the frequency independent coupling.

The cascade synthesis techniques of wideband microwave filters by extracting the values of circuit elements from the [*ABCD*] matrix have been successfully developed in Chapter Three. Again, three types of frequency dependent coupling inverters are investigated, and included in the equivalent circuit model. In contrast to narrowband case, the extraction procedures and the equations used to extract the element values are more complicated.

Based on the newly developed synthesis techniques in Chapter Two and Three, various wideband microwave filters have been designed and demonstrated in Chapter Four. This again proves the powerfulness of the synthesis techniques, and clearly indicates the usefulness of the wideband equivalent circuit model representing the filter frequency responses over a very wide frequency range.

In Chapter Five, several novel microwave transitions designs realized in LTCC technology have been demonstrated, which have integrated more functionality into conventional transition design, such as very wide bandwidth, embedded filtering function, and so on.

6.2 FUTURE RESEARCH

Both equivalent circuit models in Chapter 2 and 3 consist of LC resonators and frequency dependent couplings. Only the first resonant mode of the resonators is considered. In the filter realizations in Chapter 4, the demonstrated resonant structure is also simply represented by single mode resonator. Overall, the synthesis, design and realization of microwave filters in this dissertation are focused on the main passband of the filters, even though a very wide bandwidth has been achieved and excellent performance has been obtained. In another aspect of practical filter design, the stopband performance of a filter is also very critical. Especially the effect of the second resonant mode of the resonators or the first harmonic will sometimes deteriorate the stopband performance severely. Therefore, is it possible that the wider frequency range concerning both filter passband and filter stopband can be studied and accurately predicted from the circuit network synthesis? The topic under the scope will investigate more advanced equivalent circuit model and synthesis techniques that can represent more information for practical filter design.

In Section 2.7, for the general case where all three types of frequency dependent couplings are involved, a numerical optimization approach is used to solve the synthesis problem of coupling matrix, and find the element values in coupling matrix. However, an analytical procedure is still desired, since it can produce more freedom on selecting the coupling elements and coupling topology, and provide insight about the realization of transmission zeros in coupling matrix approach. Such techniques

have been developed for the narrowband band case for multi-coupled resonators filter, although it is relatively simpler.

In Section 3.5, the extraction methods for inductive and capacitive coupling inverters acting as cross-coupling elements (either symmetric or asymmetric) have been given. It is still possible that the composite type coupling inverter can be used as cross-coupling, and its extraction equation should exist. Thus, this method is still needed to complete the set of extraction questions, and envision more possible coupling topologies, although the physical realization of the composite type coupling inverter for cross-coupling is very challenging.

Another widely used method to realize a transmission zero for a narrowband microwave filter is the Extracted-Pole method [71], which has not been covered in this dissertation. It will be interesting to investigate the possible extraction procedure and extraction equation to handle this structure.

Appendices

APPENDIX A

The matrices $(C - M^C)$ and $(P - M^L)$ are both real symmetric and positive definite. Symmetry follows from the reciprocity of the circuit model. The proof on the positive definite property is from the passivity of the circuit

$$C_i > 0 \quad C_i > \sum_{j=1,\, j\neq i}^{N} \left| C_{ij} \right|$$

$$\frac{1}{L_i} > 0 \quad \frac{1}{L_i} > \sum_{j=1,\, j\neq i}^{N} \left| \frac{1}{L_{ij}} \right| \tag{A1}$$

Thus, both $(C - M^C)$ and $(P - M^L)$ are diagonally dominant matrices. Invoking Sylvester's criterion in linear algebra, which states that "a symmetric row diagonally dominant matrix with positive diagonal entries is positive definite," it is concluded that both $(C - M^C)$ and $(P - M^L)$ are real, symmetric and positive definite matrices.

Next is to show that $A^t(P - M^L)A$ is real symmetric and positive definite. The matrix is real, and since

$$\left[A^t(P - M^L)A \right]^t = A^t(P^t - M^{Lt})A = A^t(P - M^L)A \tag{A2}$$

it is symmetric.

From (2.33), $A = Q\sqrt{\Lambda_C^{-1}}$, where Q is an orthogonal matrix, and Λ_C is a diagonal matrix. Since $(P - M^L)$ is real symmetric and positive definite, then it can be decomposed as

$$(P - M^L) = YDY^t \tag{A3}$$

where $D = diag(d_1, d_2, \ldots, d_n)$, $d_i > 0$, and Y is an orthogonal matrix, satisfying $YY^t = Y^tY = I$. Thus,

$$A^t(P - M^L)A = \sqrt{\Lambda_C^{-1}}Q^tY\sqrt{D} \cdot \sqrt{D}Y^tQ\sqrt{\Lambda_C^{-1}} = Z^tZ \tag{A4}$$

where

$$Z = \sqrt{D}Y^tQ\sqrt{\Lambda_C^{-1}} \tag{A5}$$

Note that Z is invertible,

$$Z^{-1} = \left[\sqrt{D}Y^tQ\sqrt{\Lambda_C^{-1}}\right]^{-1} = \sqrt{\Lambda_C}Q^tY\sqrt{D^{-1}} \tag{A6}$$

Thus, for any vector $v \neq 0, Zv \neq 0$.

Therefore,

$$v^t(Z^tZ)v = \left(v^tZ^t\right)Zv = \left\|Zv\right\|^2 > 0 \tag{A7}$$

This concludes that $Z^tZ = A^t(P - M^L)A$ is positive definite.

The proof on the real symmetric and positive definite property of $\sqrt{L}(C - M^C)\sqrt{L}$ is similar.

APPENDIX B

This Appendix shows the even- and odd-excitation method to extract the values of circuit elements according to the equivalent circuit model in Fig. 3.8 from the EM simulation results.

The circuit model shown in Fig. 3.8 represents a 2-pole symmetric filter. Therefore, a symmetric plane *T-T'* can be placed in the middle as shown in Fig. 3.9. Under the condition of even-excitation of the two ports, the middle symmetric plane *T-T'* is open circuit, equivalent to a perfect magnetic conductor at *T-T'*. The reflection coefficient of the bisected network under even excitation is defined as S_e. Under the condition of odd-excitation of the two ports, the middle symmetric plane *T-T'* is short circuit, equivalent to perfect electric conductor at *T-T'*. The reflection coefficient of the bisected network under odd excitation is defined as S_o.

Relate the S_e and S_o to the *S*-parameters of two-port network:

$$S_e = S_{11} + S_{21} \text{ and } S_o = S_{11} - S_{21} \tag{B.1}$$

or

$$S_{11} = \tfrac{1}{2}(S_e + S_o) \text{ and } S_{21} = \tfrac{1}{2}(S_e - S_o) \tag{B.2}$$

Derive the input admittance $Y_{in(e,o)}$ of the bisected network under even- and odd-excitation, respectively:

$$Y_{in,e} = sC_{xe} + \frac{1}{sL_{xe}}$$

$$C_{xe} = C_1 - C_{12} \text{ and } \frac{1}{L_{xe}} = \frac{1}{L_1} - \frac{1}{L_{12}} \tag{B.3}$$

and

$$Y_{in,o} = sC_{xo} + \frac{1}{sL_{xo}}$$

$$C_{xo} = C_1 + C_{12} \text{ and } \frac{1}{L_{xo}} = \frac{1}{L_1} + \frac{1}{L_{12}} \tag{B.4}$$

So the goal now is to find C_{xe} & L_{xe} from S_e and C_{xo} & L_{xo} from S_o, respectively, from which the values of circuit element C_1, L_1, C_{12} and L_{12} can be solved.

Derive the reflection coefficient from the input admittance of the network, assuming the characteristic admittance of the port is 1 (S):

$$S_{11} = \frac{1 - Y_{in}}{1 + Y_{in}} \text{ and } Y_{in} = sC_x + \frac{1}{sL_x} \tag{B.5}$$

$$S_{11} = \frac{\left[1 - j(\omega C_x - \frac{1}{\omega L_x})\right]^2}{1 + (\omega C_x - \frac{1}{\omega L_x})^2} = \frac{1 - (\omega C_x - \frac{1}{\omega L_x})^2 - 2j(\omega C_x - \frac{1}{\omega L_x})}{1 + (\omega C_x - \frac{1}{\omega L_x})^2} \tag{B.6}$$

The bisected network is basically an *LC* resonator. The location of the resonant frequency ω_0 can be found from the extreme point of group delay. At the resonant frequency ω_0, the phase of S_{11} becomes zero, and the imaginary part of S_{11} is also

zero:

$$\omega_0 = \frac{1}{\sqrt{C_x L_x}} \tag{B.7}$$

When the phase of S_{11} is +/- 90 degree, the real part of S_{11} will become zero:

$$1 - (\omega C_x - \frac{1}{\omega L_x})^2 = 0 \tag{B.8}$$

$$\omega_1 C_x - \frac{1}{\omega_1 L_x} = 1 \text{ and } \omega_2 C_x - \frac{1}{\omega_2 L_x} = -1 \tag{B.9}$$

where ω_1 and ω_2 are the frequency points where the phase of S_{11} is +90 degree and -90 degree, respectively.

$$C_x = \frac{1}{\omega_1 - \omega_2} \text{ and } L_x = \frac{\omega_1 - \omega_2}{\omega_1 \omega_2} \tag{B.10}$$

So C_{xe} & L_{xe} can be found from S_e, and C_{xo} & L_{xo} from S_o, respectively. Then C_1, L_1, C_{12} and L_{12} can be solved by

$$C_1 = \frac{1}{2}(C_{xo} + C_{xe}) \tag{B.11}$$

$$C_{12} = \frac{1}{2}(C_{xo} - C_{xe}) \tag{B.12}$$

$$\frac{1}{L_1} = \frac{1}{2}(\frac{1}{L_{xo}} + \frac{1}{L_{xe}}) \tag{B.13}$$

$$\frac{1}{L_{12}} = \frac{1}{2}(\frac{1}{L_{xo}} - \frac{1}{L_{xe}}) \tag{B.14}$$

Bibliography

[1] A. E. Atia, "Wideband communication satellite payload architecture," in *IEEE MTT-S Int. Microwave Symp. Dig.*, Baltimore, MD, June 2011, pp. 1–4.

[2] Digital Video Broadcasting (DVB), ETSI EN 302 307, V1.2.1, April 2009. http://www.etsi.org/deliver/etsi_en/302300_302399/302307/01.02.01_60/en_302307v010201p.pdf.

[3] Bruce Elbert, *Digital Communications - Fundamentals and Applications*, Upper Saddle Hill, New Jersey: Prentice Hall, 2001.

[4] C. T. Rodenbeck, S.-G. Kim, et. al., "Ultra-wideband low-cost phased-array radars," *IEEE Trans. Microw. Theory Tech.*, vol. 53, no. 12, pp. 3697–3703, Dec. 2005.

[5] U. Schmid, H. Sledzik, *et. al.*, "Ultra-wideband GaN MMIC chip set and high power amplifier module for multi-function defense AESA applications," *IEEE Trans. Microw. Theory Tech.*, vol. 61, no. 8, pp. 3043–3051, Aug. 2013.

[6] S. Masuda, M. Yamada, *et. al.*, "C-Ku band GaN MMIC T/R frontend module using multilayer ceramics technology," in *IEEE MTT-S Int. Dig.*, Baltimore, MD, Jun. 2011, pp. 1–4.

[7] A. E. Atia, A. E. Williams, and R. W. Newcomb, "Narrow-band multiple-coupled cavity synthesis", *IEEE Trans. Circuits Syst.*, vol. CAS-21, pp. 649-655, Sept. 1974.

[8] R. J. Cameron, "General coupling matrix synthesis methods for Chebychev

filtering functions," *IEEE Trans. Microwave Theory Tech.,* vol. MTT-47, pp. 433-442, Apr. 1999.

[9] R J. Cameron, J. C. Faugere, and F. Seyfert, "Coupling matrix synthesis for a new class of microwave filter configuration", in *IEEE MTT-S Int. Microw. Symp. Dig.*, Long Beach, CA, Jun. 2005, pp. 119-122.

[10] R. J. Wenzel, "Exact design of wideband equal-ripple bandpass filters with non-adjacent resonator couplings," in *IEEE MTT-S Int. Microw. Symp. Dig.*, Jun. 1976, pp. 125-127.

[11] R. J. Wenzel, "Synthesis of combline and capacitively loaded inter-digital bandpass filters of arbitrary bandwidth," *IEEE Trans. Microwave Theory Tech.,* vol. MTT-19, no. 8, pp. 678-686, Aug. 1971.

[12] S. Amari, M. Bekheit, and F. Seyfert, "Notes on bandpass filters whose inter-resonator coupling coefficients are linear functions of frequency", in *IEEE MTT-S Int. Microw. Symp. Dig.*, Atlanta, GA, Jun. 2008, pp. 1207-1210.

[13] W. Meng, H.-M. Lee, K. A. Zaki, and A. E. Atia, "Synthesis of multi-coupled resonator filters with frequency-dependent couplings", in *IEEE MTT-S Int. Microw. Symp. Dig.*, Anaheim, CA, May 2010, pp. 1716-1719.

[14] S. Amari, F. Seyfert, and M. Bekheit, "Theory of coupled resonator microwave bandpass filters of arbitrary bandwidth," *IEEE Trans. Microwave Theory Tech.,* vol. 58, pp. 2188-2203, Aug. 2010.

[15] K. Kurokawa, *An Introduction to the Theory of Microwave Circuits*. New York: Academic Press, 1969.

[16] E. A. Guillemin, *The Mathematics of Circuit Analysis*. New York: J. Wiley,

1949.

[17] H. J. Orchard and G. C. Temes, “Filter design using transformed variables,” *IEEE Trans. Circuits Theory*, vol. CT-15, no. 4, pp. 385-408, Dec. 1968.

[18] Y. Zhang, K. A. Zaki, J. A. Ruiz-Cruz, and A. E. Atia, “Analytical synthesis of generalized multi-band microwave filters”, in *IEEE MTT-S Int. Microw. Symp. Dig.*, Honolulu, HI, Jun. 2007, pp. 1273-1276.

[19] MATLAB, http://www.mathworks.com.

[20] G. Matthaei, L. Young, and E. M. T. Jones, *Microwave Filters, Impedance-Matching Networks, and Coupling Structures*. Norwood, MA: Artech House, 1980.

[21] R. J. Cameron, “Fast generation of Chebyshev filter prototypes with asymmetrically prescribed transmission zeros”, *ESA J.*, vol. 6, pp. 83-95, 1982.

[22] H. C. Bell, “Canonical asymmetric coupled-resonator filters,” *IEEE Trans. Microw. Theory Tech.*, vol. MTT-30, no. 9, pp. 1335–1340, Sep. 1982.

[23] R. Levy, “Synthesis of general asymmetric singly- and doubly-terminated cross-coupled filters,” *IEEE Trans. Microw. Theory Tech.*, vol. 42, pp. 2468-2471, Dec. 1994.

[24] R. J. Cameron, C. M. Kudsia, and R. R. Mansour, *Microwave Filters for Communication Systems*, John Wiley & Sons, New Jersey, 2007.

[25] S. Darlington, “Synthesis of reactance 4-poles which produce prescribed insertion loss characteristics,” *J. Math. Phys.*, vol. 30, no. 9, pp. 257-353, Sept. 1939.

[26] H. W. Bode, *Network Analysis and Feedback Amplifier Design*, New Jersey:

Van Nostrand, 1945.

[27] M. E. van Valkenburg, *Network Analysis*, New Jersey: Prentice-Hall, 1955.

[28] E. A. Guillemin, *Synthesis of Passive Networks*, New York: Wiley, 1957.

[29] W. Cauer, *Synthesis of Linear Communication Networks*, New York: McGraw-Hill, 1958.

[30] J. D. Rhodes, *Theory of Electrical Filters*, New York: Wiley, 1976.

[31] G. Szentirmai, "FILSYN—A general purpose filter synthesis program," Proc. IEEE, vol. 65, no. 10, pp. 1443-1458, Oct. 1977.

[32] R. J. Cameron, "General prototype network synthesis methods for microwave filters", *ESA J.*, vol. 6, pp. 193-206, 1982.

[33] D. M. Pozar, *Microwave Engineering*, New York: Wiley, 2012.

[34] R. E. Collin, *Foundations for Microwave Engineering*, McGraw-Hill, New York, 1966.

[35] J.R. Montejo-Garai, J. A. Ruiz-Cruz, et. al., "Synthesis and design of in-line N-order fitlers with N real transmission zeros by means of extracted poles implemented in low-cost rectangular H-plane waveguide," *IEEE Trans. Microw. Theory Tech.*, vol. 5, no. 5, pp. 1636–1642, May 2005.

[36] J.-S. Hong and M. J. Lancaster, *Microstrip Filters for RF/Microwave Applications*. New York: Wiley, 2001.

[37] P. A. Rizzi, *Microwave Engineering: Passive Circuits*, New Jersey: Prentice-Hall, 1988.

[38] J.-S. Hong and M. J. Lancaster, "Couplings of microstrip square open-loop resonators for cross-coupled planar microwave filters," *IEEE Trans. Microw.*

Theory Tech., vol. 44, no. 12, pp. 2099–2109, Dec. 1996.

[39] Y. Rong and K. A. Zaki, "Full-wave analysis of coupling between cylindrical combline resonators," *IEEE Trans. Microw. Theory Tech.*, vol. 47, no. 9, pp. 1721–1729, Sept. 1999.

[40] H.-M. Lee, K. A. Zaki and A. E. Atia, "Wide-band bandpass filters simulation, design and diagnosis," in *IEEE MTT-S Int. Microw. Symp. Dig.*, Anaheim, CA, May 2010, pp. 441-444.

[41] W. Meng, K. A. Zaki, and A. E. Atia, "Prototype network synthesis for wideband microwave filters," in *IEEE MTT-S Int. Microwave Symp. Dig.*, Baltimore, MD, June 5-10, 2011.

[42] R. J. Cameron, "Advanced coupling matrix synthesis techniques for microwave filters," *IEEE Trans. Microw. Theory Tech.*, vol. 51, no. 1, pp. 1–10, Jan. 2003.

[43] A. J. Piloto, "Integrated passive components: a brief overview of LTCC surface mount and integral options," *Adv. Microelectron. Mag.*, vol. 26, pp. 24-28, 1999.

[44] A. Piloto, K. Leahy, B. Flanick, and K. A. Zaki, "Waveguide filters having a layered dielectric structure," U.S. 5382931, Jan. 17, 1995.

[45] J. Gipprich, D. Stevens, M. Hageman, A. Piloto, K. A. Zaki, and Y. Rong, "Embedded waveguide filters for microwave and wireless applications using cofired ceramic technologies," in *Proc. Int. Microelectron. Symp*, San Diego, CA, 1998, pp. 23–26.

[46] Y. Rong, K. A. Zaki, J. Gipprich, M. Hageman, and D. Stevens, "LTCC wide-

band ridge-waveguide bandpass filters," *IEEE Trans. Microw. Theory Tech.*, vol. 47, no. 9, pp. 1836–1940, Sep. 1999.

[47] C. Lee, A. Sutono, C. Lee, S. Han, K. Lim, S. Pinel, E. Tentzeris, and J. Laskar, "A compact LTCC-based Ku-band transmitter module," *IEEE Trans. Adv. Packag.*, vol. 25, pp. 374–384, Aug. 2002.

[48] L. K. Yeung and K.-L. Wu, "A compact second-order LTCC band-pass filter with two finite transmission zeros," *IEEE Trans. Microw. Theory Tech.*, vol. 51, no. 2, pp. 337–341, Feb. 2003.

[49] Y. Huang, K.-L. Wu, D.-G. Fang and M. Ehlert, "An integrated LTCC mm-wave planar array antenna with low loss feeding network," *IEEE Trans. Antenna & Propagation*, vol.53, no.3, pp.1232-1234, Mar. 2005.

[50] C. W. Tang and S. F. You, "Design methodologies of LTCC bandpass filters, diplexer and triplexer with transmission zeros," *IEEE Trans. Microwave Theory Tech.*, vol. 54, no. 2, pp. 717–723, Feb. 2006.

[51] D. G. Kam, D. Liu, and *et. al.*, "LTCC packages with embedded phased-array antennas for 60 GHz communications," *IEEE Microw. Wireless Compon. Lett.*, vol. 21, no. 3, pp. 142–144, Mar. 2011.

[52] K. A. Zaki, "Low temperature cofired ceramic (LTCC) technology for ridge waveguide filters and multiplexers," in *Proc. Wireless Comm. Tech.*, Oct. 2003.

[53] Z. M. Liu, J. A. Ruiz-Cruz, C. Wang, and K. A. Zaki, "An extremely wideband ridge waveguide filter," in *IEEE MTT-S Int. Microw. Symp. Dig.*, Jun 2004, pp. 615-618.

[54] J. A. Ruiz-Cruz, Y. Zhang, K. A. Zaki, A. J. Piloto, and J. Tallo, "Ultra-

wideband LTCC ridge waveguide filters," *IEEE Microw. Wireless Compon. Lett.*, vol. 17, no. 2, pp. 115–117, Feb. 2007.

[55] G. L. Matthaei, "Comb-line band-pass filters of narrow or moderate bandwidth," *Microwave J.*, vol. 6, pp. 82–91, Aug. 1963.

[56] H.-W. Yao, K. A. Zaki, A. E. Atia, and R. Hershtig, "Full-wave modeling of conducting posts in rectangular waveguides and its applications to slot coupled combline filters," *IEEE Trans. Microw. Theory Tech.*, vol. 43, no. 12, pp. 2824–2830, Dec. 1995.

[57] M. A. El Sabbagh, H.-T. Hsu, K. A. Zaki, P Pramanick and T. Dolan, "Full wave optimization of stripline tapped-in ridge waveguide bandpass filters," in *IEEE MTT-S Int. Microwave Symp. Dig.*, Seattle, WA, June 2002, pp. 1805–1808.

[58] Ansys HFSS, http://www.ansys.com.

[59] J. A. Ruiz-Cruz, *Contribution to the CAD of Microwave-Millimeterwave Passive Devices by Mode-Matching Techniques*. PhD Thesis, Univ. Politecnica de Madrid, Madrid, Spain, 2005.

[60] J. Helszajn, *Ridge Waveguides and Passive Microwave Components*, London: IEE Electromagnetic waves series 49, 2000.

[61] M. Guglielmi and G. Conner, "Chained function filters," *IEEE Microw. Guided Wave Lett.*, vol. 7, no.12, pp. 390–392, Dec. 1997.

[62] C. E. Chrisostomidis and S. Lucyszyn, "On the theory of chained-function filters," *IEEE Trans. Microw. Theory Tech.*, vol. 53, no. 10, pp. 3142–3151, Oct. 2005.

[63] S. Amari and U. Rosenberg, "New building blocks for modular design of elliptic and self-equalized filters," *IEEE Trans. Microw. Theory Tech.*, vol. 52, pp. 721–736, Feb. 2004.

[64] S. Amari, U. Rosenberg, and J. Bornemann, "Singlets, cascaded singlets and the nonresonating node model for modular design of advanced microwave filters," *IEEE Microw. Wireless Compon. Lett.*, vol. 14, no. 5, pp. 237–239, May 2004.

[65] H.-W. Yao, A. Abdelmonem, J.-F. Liang, and K. A. Zaki, "Analysis and design of microstrip-to-waveguide transitions," *IEEE Trans. Microw. Theory Tech.*, vol. 42, no. 12, pp. 2371–2380, Dec. 1994.

[66] Y. Huang and K.-L. Wu, "A broad-band LTCC integrated transition of laminated waveguide to air-filled waveguide for millimeter wave applications," *IEEE Trans. Microw. Theory Tech.*, vol. 51, no. 5, pp. 1613–1617, May 2003.

[67] Y. Ding and K. Wu, "Substrate integrated waveguide-to-microstrip transition in multilayer substrate," in *IEEE MTT-S Int. Microw. Symp. Dig.*, 2007, pp. 1555–1558.

[68] S. Sun, Z. Wang, B. Yan, and R. Xu, "Waveguide to microstrip transitions in W-band with LTCC technology," *In Proc. Asia-Pacific Microw. Conf.*, Singapore, 2009, pp. 2515-2517.

[69] R. Gomez-Garcia, M. Sanchez-Renedo, J.-M. Munoz-Ferreras, "Microwave filtering power-distribution planar network," in *IEEE MTT-S Int. Dig.*, Baltimore, MD, Jun. 2011, pp. 1–4.

[70] M.-G. Choi, H.-M. Lee, Y.-H. Cho, X.-G. Wang, and S.-W. Yun, "Design of

Wilkinson power divider with embedded low-pass filter and cross-stub for improved stop-band characteristics," in *IEEE MTT-S Int. Dig.*, Baltimore, MD, Jun. 2011, pp. 1–4.

[71] J. D. Rhodes and R. J. Cameron, "General extracted pole synthesis technique with application to low-loss TE011-mode filters," *IEEE Trans. Microw. Theory Tech.*, vol. MTT-28, no. 9, pp. 1018–1028, Sept. 1980.

[72] W. Meng, H. M. Lee, K. A. Zaki, and A. E. Atia, "Synthesis of wideband multicoupled resonator filters," *IEEE Trans. Microw. Theory Tech.*, vol. 59, no. 3, pp. 593–603, Mar. 2011.

[73] W. Meng, K. A. Zaki, A. E. Atia, and A. J. Piloto, "Cascade synthesis of wideband microwave filters with composite couplings," to be submitted to *IEEE Trans. Microw. Theory Tech.*